Astronomy Letters, Vol. 31, No. 4, 2005, pp. 221–226. Translated from Pis'ma v Astronomicheskiĭ Zhurnal, Vol. 31, No. 4, 2005, pp. 243–249.
Original Russian Text Copyright © 2005 by Verkhodanov, Kopylov, Pariĭskiĭ, Soboleva, Temirova.

On the Photometric Redshift Estimates for FR II Radio Galaxies

O. V. Verkhodanov*, **A. I. Kopylov**, **Yu. N. Pariĭskiĭ**, **N. S. Soboleva**, and **A. V. Temirova**

Special Astrophysical Observatory, Russian Academy of Sciences, Nizhnii Arkhyz,
357147 Karachai-Cherkessian Republic, Russia

Received September 13, 2004

Abstract—Using the photometric data on FR II radio galaxies obtained during the Big Trio program and data from other sources, we confirmed the stable correlation between the spectroscopic and photometric redshifts up to $z \sim 4$, determined from the evolutionary synthetic spectra of elliptical galaxies. This is confirmation of the theoretical predictions of the existence of a stellar population at high redshifts and its subsequent evolution corresponding to the population of giant elliptical galaxies. *© 2005 Pleiades Publishing, Inc.*

Key words: *radio galaxies, photometry, redshifts.*

INTRODUCTION

The photometric redshifts that were first used by Baum in 1962 (Baum 1962) still remain an important tool for studying the distant Universe (see, e.g., Botzler *et al.* 2004; Rocca-Volmerange *et al.* 2004; Vanzella *et al.* 2004; Budavari *et al.* 2003). Being measured from the spectral energy distribution, they are of paramount importance as the next-to-last selection step in searching for distant objects (Bunker *et al.* 2003; Franx *et al.* 2003; Idzi *et al.* 2004), especially with the emergence of full sky surveys such as SDSS (Abazajian *et al.* 2004), where photometric classification is also used (Padmanabhan *et al.* 2004). The photometric z has become a more powerful selection factor in searching for distant radio galaxies in combination with the radio-astronomical selection based on the spectral indices and morphology (Parijskij *et al.* 1996).

The morphological signatures of radio galaxies, namely, type II (FR II) objects in the classification by Fanaroff and Riley (1974), help to reveal distant objects for several reasons:

(1) These are intense and relatively young (compared to FR I) radio sources visible at any z;

(2) They have a formed radio structure, circumstantial evidence that the source has a reserve of time for the formation of its stellar population;

(3) FR II radio galaxies have more intense emission lines than the FR I galaxies (Baum *et al.* 1995), which facilitates their spectroscopic studies.

In general, relatively close ($z < 2$) FR II radio galaxies are identified with giant elliptical galaxies with high radio luminosities and old, homogeneous stellar populations. Therefore, this type of object is convenient to use for photometric studies in radio cosmology (Pariĭskiĭ 2001). Note that the age and composition of the stellar population in radio galaxies can also be determined from the absorption lines and the continuum formed by this stellar population. However, the sensitivity is insufficient to detect such lines in the spectra of many distant radio galaxies. In addition, the measurement and identification procedure with the determination of the correct weight for each line is fairly complex. Using the continuum makes it possible to apply our knowledge about the composition and age of a radio galaxy's stellar population based on evolutionary models.

Currently available models predict the fast formation (within 1 Gyr) of such systems even at $z \sim 4$ (Pipino and Matteucci 2004), which allows photometric methods to be used to study them. The efficiency of selecting such galaxies by radio-astronomical methods, starting from moderate red shifts ($z > 0.5$), has been confirmed by several teams (Pedani 2003). The combined Hubble $K{-}z$ diagram for radio galaxies and field galaxies (Jarvis *et al.* 2001; De Breuck *et al.* 2002) shows that the radio galaxies have the highest luminosities at any redshift, $0 < z < 5.2$ (Reuland *et al.* 2003). In addition, radio galaxies have supermassive black holes whose mass is generally proportional to that of the stellar bulge ($M_{\mathrm{BH}} \sim 0.006 M_{\mathrm{bulge}}$; Magorrian *et al.* 1998), further evidence for the presence of a formed stellar population. The formation of radio galaxies at redshifts $z \sim$ 3–5 gives the already formed stellar populations at $z \sim$ 2–4 in the ΛCDM models. Thus, when selecting distant radio galaxies, we effectively single out giant

---

*E-mail: `vo@sao.ru`

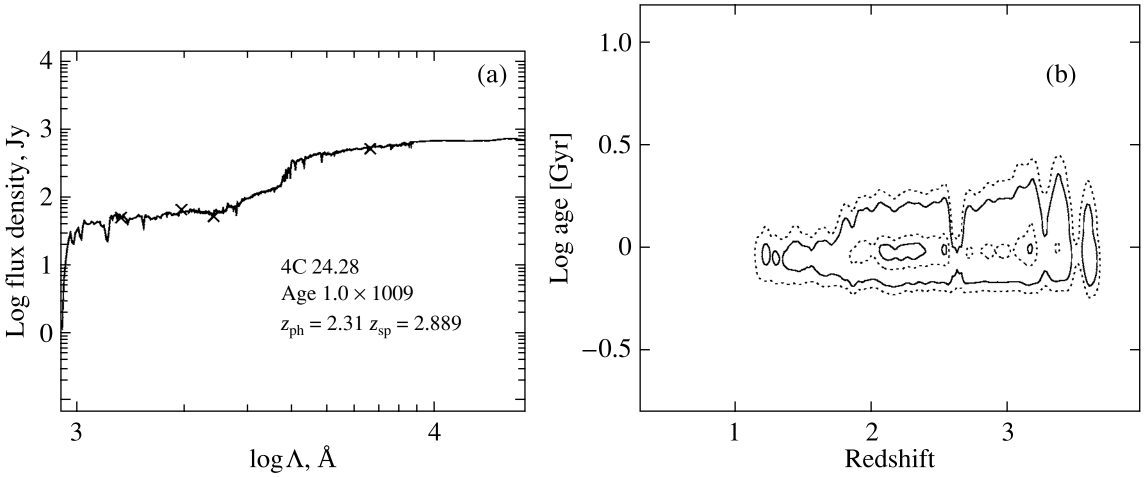

Fig. 1. Demonstration of determining the photometric redshift for the radio galaxy 4C 24.28: (a) the two-dimensional section of the three-dimensional likelihood function that depends on the redshift, age, and flux density; (b) the positions of the photometric points in the SED curve corresponding to the maximum of the likelihood function.

elliptical galaxies that can be used for photometric studies. The above shows the possibility of using the photometric technique to determine the redshifts from the stellar population for FR II radio galaxies at $z > 2$.

The most recent theoretical calculations (see, e.g., Rocca-Volmerange *et al.* 2004) indicate that evolutionary models of the spectra for elliptical galaxies can be applied even to radio galaxies with $z \sim 4$, when gE galaxies with a mass of $10^{12}\ M_\odot$ have already been formed.

Nevertheless, the presence of intense emission lines (e.g., Hα, C IV, He II) in the spectra of several distant radio galaxies that were formed by various ionization mechanisms (Maxfield *et al.* 2002) near jets and "hot spots" raises the question of whether the evolutionary spectra of elliptical galaxies correspond to those of radio galaxies and, as a result, whether the photometric technique can be used to estimate the redshifts of radio galaxies.

In this paper, we consider the $z_{\rm ph}$–$z_{\rm sp}$ relation for two samples of FR II radio galaxies that we drew in our previous papers (Parijskij *et al.* 1996; Verkhodanov *et al.* 1999, 2002a, 2002b) using the popular PEGASE (Projet d'Etude des Galaxies par Synthese Evolutive) evolutionary model of the stellar population (Fioc and Rocca-Volmerange 1997; Le Borgne and Rocca-Volmerange 2002). Apart from this model, we can use the GISSEL (Galaxy Isochrone Synthesis Spectral Evolution Library) model (Bruzual and Charlot 1993, 1996; Bolzonella *et al.* 2000), which yields similar results for photometric redshifts. The files with the spectral energy distributions (synthetic spectra) for both evolutionary models of the stellar population can be found at http://sed.sao.ru (Verkhodanov *et al.* 2000).

THE REDSHIFT ESTIMATION PROCEDURE

We took into account the absorption in our Galaxy using maps from Schlegel *et al.* (1998) written in the form of FITS files.

Before using the model curves, we smoothed them with filters by applying the following algorithm (Verkhodanov *et al.* 2002a, 2002b):

$$S_{ik} = \frac{\sum\limits_{j=1}^{n} s_{i-n/2+j} f_{jk}(z)}{\sum\limits_{j=1}^{n} f_{jk}(z)}, \tag{1}$$

where s_i is the initial model SED curve, S_{ik} is the model SED curve smoothed with the kth filter, $f_k(z)$ is the transmission curve of the kth filter "compressed" by a factor of $(1+z)$ when "moving" along the wavelength axis of the SED curve, and j is the point number in the filter transmission curve. We constructed the two-dimensional (λ, filter) array of smoothed synthetic stellar spectra from the k SED curves formed in this way for the subsequent calculations.

We estimated the redshifts and ages of the stellar populations by choosing the optimal positions of the photometric magnitudes obtained in various bands during the observations of radio galaxies in the smoothed SED curves. We used the computed and tabulated SED curves for different ages. The algorithm for choosing the optimal positions of the data points in the curve (Verkhodanov *et al.* 1996) consisted in shifting the observational points along the wavelength and intensity axes of the SED curves. In this way, we found the position at which the sum of the squares of the deviations of the data points

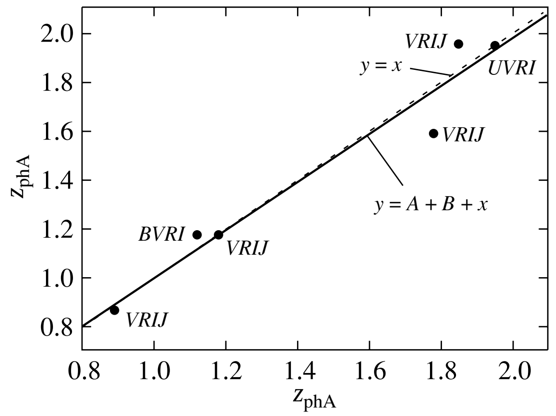

Fig. 2. The "photometric redshift based on all colors (z_{phA})—photometric redshift based on four colors (z_{ph4})" relation. The dotted line indicates the ordinate—abscissa ($x = y$) straight line. The solid line represents the z_{phA}—z_{ph4} regression with the coefficients $A = 0.0098$ and $B = 0.98531$.

from the corresponding smoothed curves was at a minimum; i.e., we actually calculated the minimum of the χ^2 value:

$$\chi^2 = \sum_{k=1}^{N\text{filters}} \left(\frac{F_{\text{obs},k} - p\text{SED}_k(z)}{\sigma_k}\right), \qquad (2)$$

where $F_{\text{obs},k}$ is the observed magnitude in the kth filter, $\text{SED}_k(z)$ is the model magnitude for a given spectral energy distribution in the kth filter at given z, p is a free coefficient, and σ_k is the measurement error. The redshift was determined from the shift in the positions of the observed magnitudes at their best positions in the SED curves from the "rest frame" position. From the whole set of curves for different ages, we chose those for which the sum of the squares of the residuals for the observational data of radio galaxies was at a minimum. Figure 1 shows an example of applying the described technique to the radio galaxy 4C 24.28 or, more specifically, the two-dimensional section of the three-dimensional likelihood function dependent on the following parameters: the redshift, the age, and the flux density, along with the positions of the photometric points in the SED curve corresponding to the maximum of the likelihood function.

We checked the validity of our redshift (and age) estimates by two methods. First, we took the synthetic spectra obtained by smoothing the SED curves for different ages with filters. This enabled us to model the CCD observations for five filters. Subsequently, we chose the data points corresponding to the $VIJHK$ filters, for example, at the redshift $z = 0.54$, and the evolutionary spectra with ages of 1 and 5 Gyr. For each age, we performed two magnitude estimation tests: with fixed $z = 0.54$ and unfixed redshift. These led us to conclude that both the age

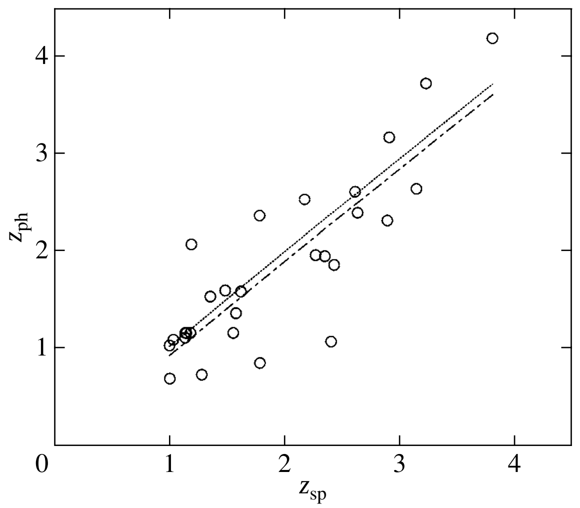

Fig. 3. The "spectroscopic redshift—photometric redshift" relation for FR II radio galaxies with $z > 1$. The dot—dashed straight line represents the regression based on all of our data (the correlation coefficient is 0.85). The dotted straight line represents the regression with the data for the objects 3C 239, 3C 266, 4C 34.34 excluded (the correlation coefficient is 0.91).

and the redshift were determined reliably. However, there is the possibility of falling on the neighboring age curve, which gives an error of 200 Myr, and the result for unfixed z is also affected by the quantization in wavelength λ in the SED curves (the error in z reaches 6%).

In the second case, we explored the possibilities for determining the redshifts and ages of the stellar populations in the parent galaxies from multicolor photometry. For this purpose, we selected about 40 distant radio galaxies with known redshifts and with published magnitudes in at least three filters (Verkho-

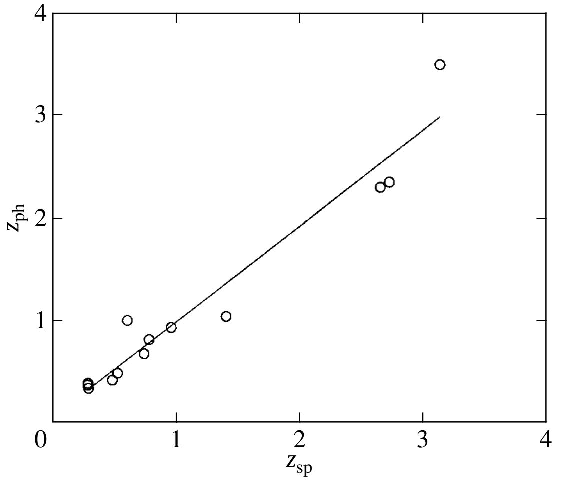

Fig. 4. The "spectroscopic redshift—photometric redshift" relation for the radio galaxies of the Big Trio program.

Table 1. The photometric redshifts for distant FR II galaxies estimated from published photometric data (Verkhodanov *et al.* 1999)

Name	$z_{\rm sp}$	$z_{\rm ph}$
3C 13	1.35	1.54
3C 65	1.176	1.17
3C 68.2	1.575	1.37
MRC 0316–257	3.142	2.64
MRC 0406–244SE	2.427	1.86
4C 41.17	3.8	4.20
3C 184	0.994	1.04
3C 194	1.185	2.07
3C 239	1.781	0.86
3C 241	1.617	1.59
B21056+39	2.171	2.53
4C 34.34	2.40	1.08
3C 266	1.275	0.74
3C 267	1.142	1.17
4C 26.38S	2.609	2.61
4C 39.37	3.225	3.73
3C 280	0.996	0.70
B21256+36	1.13	1.12
4C 24.28	2.889	2.31
3C 294	1.779	2.36
53W091	1.55	1.17
3C 368	1.132	1.17
4C 40.36	2.267	1.96
4C 48.48	2.348	1.95
MRC 2025–218	2.63	2.39
3C 437	1.48	1.60
4C 28.58	2.905	3.17
PK 2353–018	1.028	1.10

Note: The table gives the radio galaxy's name, its spectroscopically measured redshift, and its photometric z estimate.

danov *et al.* 1999). First, we determined only the ages of the stellar populations of the parent galaxies at fixed known redshifts from the collected photometric data. Then, we searched for the optimal model SED curve with the simultaneous determination of the redshift and the age of the stellar population. Subsequently, we compared the values obtained. Using this method, we estimated both the galaxy's age and its redshift based on the given models (see also Verkhodanov *et al.* 1999). It is clear from general considerations that the reliability of the result at high redshifts depends significantly on the availability of infrared data (up to the K band), since our fit covers the range of fast change in the spectrum (the jump) before the optical SED range; thus, we can determine the position of our data reliably, with a pronounced maximum in the likelihood curve. Indeed, in testing the reliability of our procedure using the available measurements while keeping only three points, one of which is in the K band , we obtain the same result in the likelihood function as that obtained from four or five points. If, however, the infrared range is not used, then the result is found to be more uncertain. However, as we showed previously (Verkhodanov *et al.* 1999), the case of four closely spaced filters, as in our case of $BVRI$ photometry, yields a good result in the check sample of six objects (Fig. 2) that matches the result obtained by using all filters, including the infrared band. Note that this set of filters works stably at medium redshifts ($z \sim 1$), which closely corresponds to the sample of radio galaxies in the Big Trio program.

THE SAMPLES OF OBJECTS

Radio Galaxies with $z > 1$

As was mentioned above, to test our technique and to estimate the redshifts and ages of stellar systems, we drew our sample of distant ($z > 1$) FR II radio galaxies with spectral indices $\alpha < -1.0$ and with redshifts up to $z = 3.80$ (Verkhodanov *et al.* 1999) from the data obtained by other authors.

It should be noted that the published photometric data are highly inhomogeneous. They were obtained not only by different authors, but also on different instruments and with different filters. The measurements for the same object were not always made with the same apertures, etc. Therefore, after the final selection, only 42 of the 300 radio galaxies from the primary sample remained. Most of the objects were not included in the sample because they have the properties of quasars, which severely complicates the use of the SED procedure for standard elliptical galaxies. From the remaining objects, we chose only the radio galaxies with an FR II structure (28 galaxies, Table 1).

Figure 3 shows the "spectroscopic redshift—photometric redshift" relation for FR II radio galaxies with $z > 1$. The correlation coefficient calculated from all of the data in Table 1 is 0.85. If we discard the outlying data attributable to random errors, where $z_{\rm sp}$ is much higher than $z_{\rm ph}$ (the objects 3C 239, 3C 266, 4C 34.34), then the correlation coefficient is 0.91.

Table 2. The redshifts and their photometric estimates for the objects of the RC catalog studied in the Big Trio program

Name	α	S_{1400}/S_{3900}	R	$z_{\rm sp}$	$z_{\rm ph}$	Notes
J0105+0501	1.05	79/25	22.8	3.14	3.5	FR II?
J0444+0501	1.09	214/69	22.7	2.73:	2.35	FR II
J0209+0501	1.16	89/33	18.5	0.285	0.38	Pointlike
J0457+0452	1.12	201/56	19.4	0.482	0.41	FR I
J0908+0451	0.92	301/109	19.6	0.525	0.48	FR II
J1124+0456	0.94	935/400	17.8	0.284	0.36	FR II
J1155+0444	1.0	141/54	18.6	0.289	0.33	FR II
J1333+0451	1.3	42/11	18.1	1.405	1.04	FR II QSR
J1339+0445	1.07	119/41	22.6	0.74	0.67	FR II Triple
J1626+0448	1.26	191/46	22.9	2.656	2.30	FR II
J1722+0442	0.99	763/300	20.7	0.604	1.0	FR II
J2029+0456	0.69	142/53	21.7	0.78	0.81	FR II
J2224+0513	0.93	346/107	21.3	0.96	0.93	FR II

Note: The table gives the object's name, its spectral index, the ratio of the flux densities at 1.4 and 3.9 GHz, the R-band magnitude, the spectroscopic and photometric redshifts, and the radio source's morphological type.

Radio Galaxies from the RC Catalog

We drew our second sample from the FR II radio galaxies with steep spectra discovered in the RATAN-600 "Kholod" survey (Pariĭskiĭ *et al.* 1991, 1992) using multicolor photometry to estimate the color redshifts and the ages of the parent galaxies' stellar systems (Parijskij *et al.* 1996; Verkhodanov *et al.* 2002). In the Big Trio observations (Parijskij *et al.* 1996; Pariĭskiĭ *et al.* 1998), the $BVRI$ magnitudes were measured for about 60 radio galaxies, and it was found that although their color ages had a large dispersion, the redshifts could be estimated reliably.

Subsequently, 20 objects were observed spectroscopically with the SCORPIO instrument at the 6 m BTA telescope (Afanasiev *et al.* 2002, 2003). Their z measurements (Kopylov *et al.* 1995a, 1995b; Parijskij *et al.* 1996; Pariĭskiĭ *et al.* 1998) and photometric estimates based on BTA observations (Parijskij *et al.* 1996; Verkhodanov *et al.* 2002a, 2002b) were obtained before spectroscopy by Afanasiev *et al.* (2002, 2003) and are collected in Table 2.

As we see from Table 2, the z measurements confirm our photometric estimates (Fig. 4) even for some of the quasars. The correlation coefficient estimated from the observations of Kholod radio galaxies is 0.92.

CONCLUSIONS

Using the photometric data for FR II radio galaxies with steep spectra obtained as part of the Big Trio program and data from other sources in the astronomical literature, we have confirmed the stable correlation between the spectroscopic and photometric redshifts up to $z \sim 4$ determined from the evolutionary synthetic spectra of elliptical galaxies. The technique that we have used since 1995 (Parijskij *et al.* 1996) has demonstrated its efficiency in selecting distant radio galaxies and investigating their evolutionary properties.

That the photometric estimates for FR II radio galaxies are close to direct measurements suggests that the continuum optical spectra of radio galaxies can be described by stellar models, while the evolutionary models of elliptical galaxies used correspond to the stellar population of distant radio galaxies and are generally evidence of its existence at high redshifts. This allows us to further use the photometric methods based on evolutionary models with a high degree of confidence to study FR II radio galaxies and to estimate cosmological parameters (Verkhodanov and Parijskij 2003; Starobinsky *et al.* 2004).

ACKNOWLEDGMENTS

O.V. Verkhodanov and A.I. Kopylov are grateful to the Russian Foundation for Basic Research (project no. 02-07-90038) for their partial support of this work. Yu.N. Pariĭskiĭ was supported by grants from the Integration and Astronomy programs and the Russian Foundation for Basic Research. We wish to thank the referee for remarks that improved the paper.

REFERENCES

1. K. Abazajian, J. K. Adelman-McCarthy, M. A. Agueros, *et al.* (SDSS Collab.), Astron. J. **128**, 502 (2004).
2. V. L. Afanasiev, S. N. Dodonov, A. V. Moiseev, *et al.*, Preprint No. 139, SPb Filial SAO RAN (St. Petersburg Branch of Spec. Astrophys. Obs., Russ. Acad. of Sci., 2002).
3. V. L. Afanasiev, S. N. Dodonov, A. V. Moiseev, *et al.*, Astron. Zh. **80**, 409 (2003) [Astron. Rep. **47**, 377 (2003)].
4. W. A. Baum, *Proc. IAU Symp. 15, Problems of Extra-Galactic Research*, Ed. by G. C. McVittie (Macmillan Press, New York, 1962), p. 390.
5. S. A. Baum, E. L. Zirbel, and C. P. O'Dea, Astrophys. J. **451**, 88 (1995).
6. M. Bolzonella, J.-M. Miralles, and R. Pelló, Astron. Astrophys. **363**, 476 (2000); astro-ph/0003380.
7. C. S. Botzler, J. Snigula, R. Bender, and V. Hopp, Mon. Not. R. Astron. Soc. **349**, 425 (2004).
8. G. Bruzual and S. Charlot, Astrophys. J. **405**, 538 (1993).
9. G. Bruzual and S. Charlot, 1996, anonymous@ftp://gemini.tuc.noao.edu/pub/charlot/bc96.
10. T. Budavari, A. J. Connolly, A. S. Szalay, *et al.*, Am. Astron. Soc. Meet. **202**, 1901 (2003).
11. A. J. Bunker, E. R. Stanway, R. S. Ellis, *et al.*, Am. Astron. Soc. Meet. **202**, 1110 (2003).
12. C. De Breuck, W. van Breugel, S. A. Stanford, *et al.*, Astron. J. **123**, 637 (2002).
13. B. L. Fanaroff and J. M. Riley, Mon. Not. R. Astron. Soc. **167**, 31p (1974).
14. M. Fioc and B. Rocca-Volmerange, Astron. Astrophys. **326**, 950 (1997).
15. M. Franx, I. Labbe, G. Rudnick, *et al.*, Astrophys. J. Lett. **587**, L79 (2003).
16. M. J. Jarvis, S. Rawlings, S. Eales, *et al.*, Mon. Not. R. Astron. Soc. **326**, 1585 (2001).
17. R. Idzi, R. Somerville, C. Papovich, *et al.*, Astrophys. J. **600**, L115 (2004).
18. A. I. Kopylov, V. M. Goss, Yu. N. Pariĭskiĭ, *et al.*, Astron. Zh. **72**, 613 (1995a) [Astron. Rep. **39**, 543 (1995a)].
19. A. I. Kopylov, V. M. Goss, Yu. N. Pariĭskiĭ, *et al.*, Astron. Zh. **72**, 437 (1995b) [Astron. Rep. **39**, 383 (1995b)].
20. D. Le Borgne and B. Rocca-Volmerange, Astron. Astrophys. **386**, 446 (2002).
21. J. Magorrian, S. Tremaine, D. Richstone, *et al.*, Astron. J. **115**, 2285 (1998).
22. L. Maxfield, H. Spinrad, and D. Stern, Astron. J. **123**, 2321 (2002).
23. N. Padmanabhan, T. Budavari, D. J. Schlegel, *et al.*, Mon. Not. R. Astron. Soc. (2004) (submitted); astro-ph/0407594.
24. Yu. N. Parijskij, *Proc. NATO Advanced Study Inst., Current Topics in Astrofundamental Physics: the Cosmic Microwave Background*, Ed. by Norma G. Sanchez (Kluwer Acad. Publ., 2001), p. 219.
25. Yu. N. Parijskij, N. N. Bursov, N. M. Lipovka, *et al.*, Astron. Astrophys., Suppl. Ser. **87**, 1 (1991a).
26. Yu. N. Parijskij, N. N. Bursov, N. M. Lipovka, *et al.*, Astron. Astrophys., Suppl. Ser. **96**, 583 (1991b).
27. Yu. N. Parijskij, W. M. Goss, A. I. Kopylov, *et al.*, Bull. Spec. Astrophys. Obs. **40**, 5 (1996).
28. Yu. N. Pariĭskiĭ, A. I. Kopylov, W. M. Goss, *et al.*, Astron. Zh. **75**, 483 (1998) [Astron. Rep. **42**, 425 (1998)].
29. Yu. N. Parijskij, W. M. Goss, A. I. Kopylov, *et al.*, Astron. Astrophys. Trans. **19**, 297 (2000).
30. M. Pedani, New Astron. **8**, 805 (2003).
31. A. Pipino and F. Matteucci, Mon. Not. R. Astron. Soc. **347**, 968 (2004).
32. M. Reuland, W. van Breugel, H. Röttgering, *et al.*, Astrophys. J. **592**, 755 (2003).
33. B. Rocca-Volmerange, D. Le Borgne, C. De Breuck, *et al.*, Astron. Astrophys. **415**, 931 (2004).
34. D. Schlegel, D. Finkbeiner, and M. Davis, Astrophys. J. **500**, 525 (1998).
35. A. A. Starobinsky, Yu. N. Pariĭskiĭ, and O. V. Verkhodanov, Tr. Gos. Astron. Inst. Shternberga **LXXV**, 198 (2004).
36. E. Vanzella, S. Cristiani, A. Fontana, *et al.*, Astron. Astrophys. **423**, 761 (2004).
37. O. V. Verkhodanov, Bull. Spec. Astrophys. Obs. **41**, 149 (1996).
38. O. V. Verkhodanov and Yu. N. Parijskij, Bull. Spec. Astrophys. Obs. **55**, 66 (2003).
39. O. V. Verkhodanov, A. I. Kopylov, Yu. N. Parijskij, *et al.*, Bull. Spec. Astrophys. Obs. **48**, 41 (1999); astro-ph/9910559.
40. O. V. Verkhodanov, A. I. Kopylov, O. P. Zhelenkova, *et al.*, Astron. Astrophys. Trans. **19**, 62 (2000); astro-ph/9912359, http://sed.sao.ru.
41. O. V. Verkhodanov, Yu. N. Parijskij, N. S. Soboleva, *et al.*, Bull. Spec. Astrophys. Obs. **52**, 5 (2002a); astro-ph/0203522.
42. O. V. Verkhodanov, A. I. Kopylov, Yu. N. Pariĭskiĭ, *et al.*, Astron. Zh. **79**, 589 (2002b) [Astron. Rep. **46**, 531 (2002b)].

Translated by N. Samus'

Astronomy Letters, Vol. 31, No. 4, 2005, pp. 227–238. Translated from Pis'ma v Astronomicheskiĭ Zhurnal, Vol. 31, No. 4, 2005, pp. 250–261.
Original Russian Text Copyright © 2005 by Sil'chenko.

Chemically Decoupled Nuclei in Five Lenticular Galaxies from SAURON Data

O. K. Sil'chenko[*]

Sternberg Astronomical Institute, Universitetskiĭ pr. 13, Moscow, 119992 Russia

Received October 12, 2004

Abstract—We analyze data from the SAURON integral-field spectrograph of the William Herschel 4-m telescope for five lenticular galaxies in which we previously found chemically decoupled nuclei from observations with the Multipupil Fiber Spectrograph of the 6-m Special Astrophysical Observatory telescope. In a larger field of view, we confirmed the presence of peaks of the equivalent width of the Mg Ib $\lambda 5175$ absorption line in the nuclei of all five galaxies. However, the structure of the chemically decoupled regions turned out to be highly varied even in such a small sample: from compact unresolved knots to disks with an extent of several hundred parsecs and, in one case, a triaxial compact minibar-type structure. We confirmed the presence of an inner gaseous polar ring in NGC 7280 and found it in NGC 7332. In their outer parts, the planes of these polar rings are warped toward the plane of stellar rotation in such a way that the gas counterrotates with respect to the stars. This behavior of the gas in a triaxial potential was predicted by several theoretical models. © *2005 Pleiades Publishing, Inc.*

Key words: *galaxies, groups and clusters of galaxies, galactic nuclei, galaxy structure, galaxy evolution.*

INTRODUCTION

In 1992, we published a paper (Sil'chenko *et al.* 1992) in which we reported the discovery of chemically decoupled nuclei in several disk galaxies of early types, from S0 to Sb. This discovery was the result of the very first (test) observations with the MPFS (Multipupil Fiber Spectrograph) integral-field spectrograph designed for the 6-m Special Astrophysical Observatory (SAO) telescope. MPFS was among the first integral-field instruments in the world. Spectrographs of this type implied a transition to qualitatively new spectroscopic studies of galaxies, since they allowed one to take spectra from each point of an object's extended region during a single exposure and over a wide wavelength range and, thus, to effectively compare the spectral characteristics at different locations of the region under study. The first version of MPFS (Afanasiev *et al.* 1990) was put into operation in 1989 and worked until 1993. Its optics was not too transparent, and its detector, the Kvant panoramic photon counter, was not too efficient for high-surface-brightness galaxies. Therefore, our results published in 1992 were not two-dimensional maps, but azimuthally averaged radial profiles of the equivalent widths of strong absorption lines in the integrated spectra of galaxies, Mg Ib $\lambda 5175$ and Fe I+Ca I $\lambda 5270$. However, since we had two-dimensional rather than one-dimensional (long-slit) spectroscopic data from the outset, we were able to maintain an approximately constant signal-to-noise ratio along the radius up to an angular distance of $5''$–$6''$ from the center and, thus, to estimate the spectral characteristics of the stellar nuclei of galaxies and nearby regions of their bulges by adding the spectra in rings. In 1989–1990, we observed 12 bright galaxies with morphological types from E to Sb and found chemically decoupled nuclei in seven of them: the equivalent width of the Mg Ib absorption line in the nucleus was more than 1 Å larger than its equivalent width in the nearest regions of the bulge; at the then existing accuracy of the azimuthally averaged equivalent widths, 0.3 Å, this was a significant effect. At that time, we tentatively interpreted this effect as evidence of an enhanced metallicity in the compact (unresolved) stellar nuclei of galaxies. Basically, the metallicity gradients along the radius of spheroidal stellar systems, which the elliptical galaxies and the bulges of disk galaxies are, were also known previously from broadband surface photometry (Strom *et al.* 1976; K. Strom and S. Strom 1978; Wirth 1981); in these studies, however, the nuclei were always excluded from analysis, and very "flat" changes, $\Delta[\mathrm{Fe/H}]/\Delta \log r \approx -0.2$ (Peletier *et al.* 1990), were detected in the spheroid itself. What we found looked quite different: the

---

[*] E-mail: `olga@sai.msu.su`

$EW_{\mathrm{MgIb}}(r)$ profile had a sharp break at the boundary of the galactic nucleus determined by the seeing during the observations, and a jump in metallicity of more than 0.3–0.4 dex was reached even at a radius of $R \approx 3''$. By analogy with the previously discovered kinematically decoupled nuclei (Jedrzejewski and Schechter 1988; Bender 1988; Afanasiev *et al.* 1989), we called this phenomenon a chemically decoupled nucleus; both these types of decoupling of the central region were present in several our objects, suggesting a special evolutionary status of the compact stellar nuclei of galaxies.

After 1992, we engaged in searching for and studying the chemically decoupled nuclei of galaxies in earnest; several dozen have now been found (Sil'chenko 2002a). The first version of MPFS was followed by two more modifications, and each succeeding modification was more efficient than the preceding one; the CCD detectors used on the spectrograph were also improved. We were among the first authors in the world to begin publishing two-dimensional maps of the Lick indices at the centers of galaxies (the Lick indices are the standardized equivalent widths of several absorption lines). By comparison with synthetic evolutionary models of stellar populations, for example, with the now classical models by Worthey (1994), we ascertained that, in addition to an enhanced metallicity, the chemically decoupled nuclei often have a younger mean age of the stellar population than do their surrounding bulges; i.e., they were clearly formed during a secondary starburst much later than the bulges. The first resolved chemically decoupled central structures similar in all signatures to circumnuclear compact stellar disks also appeared in our sample.

A serious limitation of our studies of chemically decoupled structures at the centers of galaxies performed so far has been the small field of view of our two-dimensional spectroscopy. In the latest version of MPFS, it is $16'' \times 16''$; if we encounter a decoupled circumnuclear disk with a radius of $5''$–$6''$, as in NGC 3384 (Sil'chenko *et al.* 2003) or NGC 3623 (Afanasiev and Sil'chenko 2004), we virtually run into the boundaries of the field of view and experience difficulties in decoupling the areas of the bulge with which we would like to compare the nuclei. Undoubtedly, two-dimensional spectroscopy with a larger field of view would help us to decoupling the chemically (and evolutionally) isolated part of a galaxy more reliably, to classify its morphology, and to determine whether this structure belongs to the classical large-scale galactic components. We got the opportunity to perform such an extensive analysis when the SAURON (Spectrographic Areal Unit for Research on Optical Nebulae) integral-field spectrograph at the William Herschel 4-m telescope was put into operation in the Canary Islands in February 1999. The SAURON field of view is $41'' \times 33''$ or 44×38 spatial elements, with the size of a single pupil array element being $0.94'' \times 0.94''$. Although the spectrograph was declared to be a private instrument, its first data appeared in the publicly accessible archive of the UK Astronomy Data Centre a year after the first observations, and we were able to retrieve, analyze, and compare them with our data. The sample of 72 nearby galaxies compiled by the SAURON team for their first ambitious survey (de Zeeuw *et al.* 2002) overlapped with our sample by one third. We have now analyzed and published the SAURON data for five galaxies, including the above NGC 3384 and NGC 3623, in which the chemically decoupled nuclei are rather extended (several hundred parsecs) circumnuclear stellar disks. In this paper, we present the SAURON data for five more lenticular galaxies in which we claimed the existence of chemically decoupled nuclei previously based on MPFS data. Three of these, NGC 524, 1023, and 7332, appeared in our very first paper (Sil'chenko *et al.* 1992). Subsequently, they were once again studied with the second version of MPFS, and we again detected magnesium abundance peaks in their nuclei (Sil'chenko 1999, 2000). Thus, this work is a third approach to studying the central regions of these three galaxies by the method of integral-field spectroscopy. As regards NGC 4564 and NGC 7280, using MPFS, we found that their unresolved nuclei are not only chemically but also evolutionally decoupled: the stellar population in them is appreciably younger than that in their surrounding old stellar spheroids (Sil'chenko 1997; Afanasiev and Sil'chenko 2000). The global properties of the five galaxies recorded in the public databases considered in this paper are given in Table 1. Let us now consider how the large magnesium index maps provided by SAURON look for these galaxies.

SAURON: OBSERVATIONS AND DATA REDUCTION

The SAURON integral-field spectrograph was designed by an international team of researchers consisting mostly of representatives of France, the Netherlands, and Great Britain. A detailed description of the spectrograph and the team can be found in the paper by Bacon *et al.* (2001). The design of the spectrograph is based on the classical scheme of turning a lens array through a small angle relative to the direction of dispersion; this is called a TIGER mode in the literature. The second version of MPFS was also based on the same principle, which facilitated our work with SAURON data. In SAURON, a medium-band interference filter cuts out a spectral range of about 4800–5400 Å; both the filter transmission curve and the reciprocal dispersion, within

Table 1. Global parameters of the five galaxies under study

NGC	524	4564	1023	7280	7332
Morphological type (NED[1])	SA(rs)0+	E6	SB(rs)0−	SAB(r)0+	S0 pec
R_{25}, arcmin (LEDA[2])	1.4	1.8	4.4	1.1	2.0
R_{25}, kpc	13.9	9.0	13.7	8.8	12.0
B_T^0 (RC3[3])	11.17	11.96	10.08	12.84	11.93
M_B (LEDA)	−21.63	−19.44	−20.23	−19.41	−19.16
$(B-V)_T^0$ (RC3)	1.00	0.90	0.93	0.85	0.87
$(U-B)_T^0$ (RC3)	0.58	0.45	0.50	0.37	0.38
V_r, km s^{-1} (NED)	2379	1142	637	1844	1172
Distance, Mpc	34.7	17.5	10.8	27.8	20.2
Line-of-sight inclination (LEDA)	8.4°	90°	90°	54°	90°
$PA_{\rm phot}$ (RC3)	–	47°	87°	78°	155°
σ_*, km s^{-1} (LEDA)	252	159	205	104	124
v_m(HI), km s^{-1} (LEDA)	–	–	190	131	136

[1] NASA/IPAC Extragalactic Database.

[2] Lyon–Meudon Extragalactic Database.

[3] Reference Catalogue of Bright Galaxies.

the range 1.11–1.21 Å/pixel, change slightly over the field of view. The sky is exposed simultaneously with an object on a single $4k \times 2k$ CCD detector and is taken at only 1.7′ from the center of the object under study. For large galaxies, this implies that the outer galactic regions are exposed instead of the sky. We took data for the five galaxies of interest, which were observed during three seasons from 1999 to 2000 (a list of exposure parameters is given in Table 2), from the publicly accessible ING (Isaac Newton Group) archive together with calibration data. Based on the comparison spectra of a neon lamp taken before and after each accumulation of the object, we extracted the spectra of spatial elements and linearized them using quadratic polynomials; the mean linearization accuracy was 0.07 Å. We corrected the spectral sensitivity variations over the field using exposures of a tungsten lamp and the different lens transmission using exposures of the twilight sky.

For the SAURON primary data reduction, we used a software package developed by Vlasyuk (1993) for MPFS data reduction and modified only slightly by the author to incorporate the peculiarities of the SAURON design. An original software package written in FORTRAN was used to compute the maps of absorption line indices; its basic element was a program written by A. Vazdekis; the program computes the Lick indices together with their statistical errors from the individual spectra of spatial elements. Since the SAURON spectral resolution (4 Å) is much higher than the standard Lick resolution (∼8 Å), theoretically, the equivalent widths of the absorption lines, their objective characteristic, must be exactly equal to the computed indices. Nevertheless, we checked whether our Lick indices were the standard ones using the spectra of standard stars from the list by Worthey *et al.* (1994) that were observed during the same periods as the galaxies. The systematic deviations of our instrumental indices from the standard Lick values did not exceed 0.2 Å, and we applied these small systematic corrections to the measurements made for the galaxies. Based on the spectra of standard stars, we also studied what corrections should be applied to the measured indices to incorporate the line broadening in the spectra of the galaxies due to the stellar velocity dispersion. The spectra of giant stars were folded with a Gaussian of variable width, following which the indices were again measured from them and then compared with the indices measured from the "unspoiled" stellar spectrum. In this way, we established the dependence of the correction to the indices on σ_*; these dependences for each index were fitted with quadratic and cubic polynomials. For a typical stellar velocity dispersion of giant lenticular galaxies, ∼200 km s^{-1}, the corrections to the indices for the line broadening are 0.15 Å for Hβ, ∼0.3 Å for Mgb, and ∼0.6 Å

Table 2. SAURON spectroscopic observations of the five galaxies

Object	Date	$T_{\exp}$, min	$FWHM''_*$
NGC 524	Sep. 4, 2000	3 × 30	1.4
NGC 1023, Position 1	Oct. 10, 1999	2 × 30	1.9
NGC 1023, Position 2	Oct. 10, 1999	2 × 30	1.9
NGC 1023, Position 3	Oct. 15, 1999	2 × 30	1.2
NGC 4564	Mar. 28/29, 2000	4 × 30	1.3
NGC 7280, Position 1	Sep. 3, 2000	3 × 30	1.4
NGC 7280, Position 2	Sep. 5, 2000	2 × 30	2.6
NGC 7332	Oct. 13, 1999	4 × 30	1.1

for Fe5270; for a velocity dispersion of ~100 km s^{-1}, which is observed in NGC 7280 and NGC 7332 (see Table 1), these corrections are negligible. The SAURON narrow spectral range is a great threat to the stability of the Fe5270 index system: even at moderate redshifts, $v_r \sim 1500-2000$ km s^{-1}, the Fe I+Ca I λ5270 line shifts to the SAURON spectral sensitivity cutoff, and the Fe5270 index is found to be systematically underestimated. Therefore, we rely below on the Mgb index measurements when discussing how the chemically decoupled nuclei look in the SAURON data: the magnesium triplet with a mean wavelength of λ5175 Å is in the middle of the SAURON spectral range and is measured most reliably.

To compute the stellar velocity field, we cross correlated the spectrum of each spatial element after the continuum subtraction and the transformation to the velocity scale with the spectra of K0–K2 giant stars observed during the same set as the galaxy. To determine the line-of-sight velocities of the gas, we measured the centroid position of the [OIII] λ5007 emission line in the galaxies where it was intense enough.

THE NUCLEI DECOUPLED IN THE MAGNESIUM LINE

Based on SAURON data, we confirmed the existence of chemically decoupled nuclei in all five galaxies considered here. The high internal accuracy of the estimated absorption line indices, which reaches 0.02–0.03 Å in the individual spatial elements of the central galactic regions and which is attributable to good statistics of the accumulated signal, makes this qualitative conclusion absolutely reliable.

In Fig. 1, we quantitatively compare the azimuthally averaged radial Mgb profiles derived from SAURON and MPFS data. Note particularly the agreement between the three Mgb profiles measured independently from SAURON data in NGC 1023 and the two Mgb profiles measured independently from MPFS data in NGC 7332: this allows us to immediately estimate the internal accuracy of the instruments by eye. The MPFS accuracy of the Mgb indices is approximately a factor of 3 lower than their SAURON accuracy. The break in the profiles at $R = 2''-4''$ is seen in the SAURON data even better than in the MPFS data: this is partly because of the higher accuracy of the data and partly because of the better atmospheric conditions and the higher spatial resolution of the observations. Good agreement between the quantitative Mgb estimates is also observed at the centers of the galaxies. However, in the outer (for MPFS) parts of the field, the MPFS magnesium indices are always found to be systematically lower than the SAURON ones. Since the only galaxy in which this discrepancy is absent, NGC 7280, is simultaneously the smallest galaxy in our sample, its angular radius is only 1.1′ (Table 1), the first thing that comes to mind is that the SAURON indices were overestimated due to the sky oversubtraction. Indeed, SAURON exposes the sky background at only 1.7′ from the galactic center, while the radius of NGC 1023 is, for example, 4.4′ (Table 1). It is clear that we subtracted not the pure sky background, but the sky background plus the galactic disk. This problem did not arise in the observations with the second version of MPFS, since the sky background was exposed separately far from the galaxy. If the magnesium line in the spectrum of the galactic disk is not as deep as that in the spectrum of the bulge because, for example, the stellar population of the disk is, on average, younger, then subtracting the "superfluous" continuum will lead to artificial line deepening, i.e., to the effect that can be seen in Fig. 1.

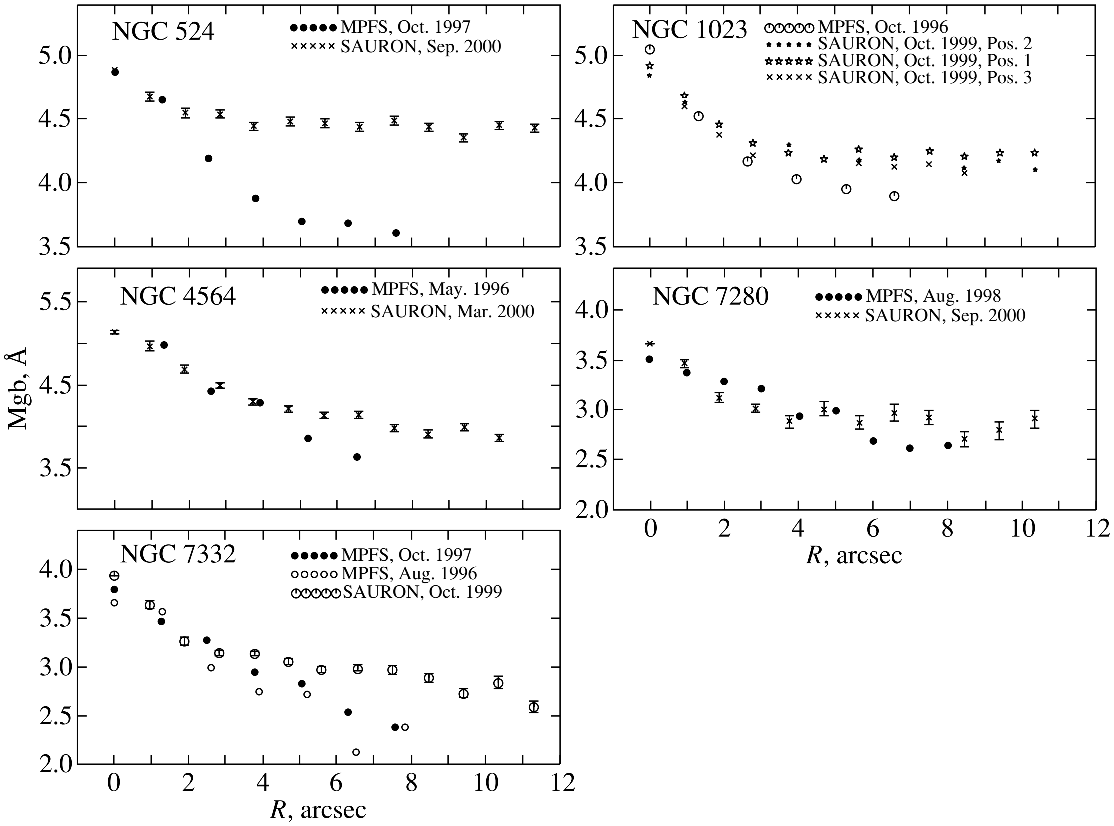

Fig. 1. Radial profiles of the azimuthally averaged Mgb absorption line index in the five galaxies under study from MPFS (which we published previously) and SAURON data.

However, this explanation in pure form is invalid: the radius of NGC 524 is only 1.4′, while the discrepancy between the MPFS and SAURON data is largest. Clearly, in addition to the sky oversubtraction in the SAURON data, the edge effects of the small field of the second MPFS version also play a role. Indeed, at a raster width of 8 elements and an element size of 1.3″, we have a full range of azimuths in the data of the second MPFS version when computing the azimuthally averaged profiles only up to a radius of 3″–4″; at larger radii, the rings open, the estimation accuracy decreases, and systematic errors appear. NGC 7280 is the only galaxy in our sample that was studied with the third version of MPFS with a 16″ × 16″ field of view. It has now become absolutely clear how important it was to confirm the existence of chemically decoupled nuclei in the galaxies using two-dimensional spectroscopy with a larger field of view than that in the first MPFS versions.

Based on Fig. 2, which shows two-dimensional distributions of the magnesium index, we can study the morphology of chemically and, hence, evolutionally decoupled substructures at the centers of galaxies. And here it emerges somewhat unexpectedly that the stellar structures decoupled in the magnesium line appear in most of the galaxies that we study as compact central knots virtually unresolved in observations. Why is this result unexpected? Because, for example, in NGC 4564 and NGC 7332, separate circumnuclear stellar disks with sizes that are quite resolvable in ground-based observations are known to exist from both photometric and kinematic studies. The radius of the central stellar disk is more than 10″ (see Pinkney *et al.* 2003, and references therein) in NGC 4564 and about 5″ (Seifert and Scorza 1996) in NGC 7332. One might expect that precisely the existence of circumnuclear stellar disks, the products of the secular evolution of disk galaxies, must cause the depth of the magnesium line to increase sharply in the integrated spectrum of the central galactic region. However, we see from Fig. 2 that the circumnuclear disks actually have magnesium indices higher than those of the bulge regions that dominate along the minor axis of the isophotes; compact knots in the nuclei, which are even more advanced in the sense of chemical evolution, are superimposed on these elongated regions. Clearly, although the secondary circumnuclear starburst often has a disk geometry, it is more effective at the distinguished point, at the geometric center of the galaxy.

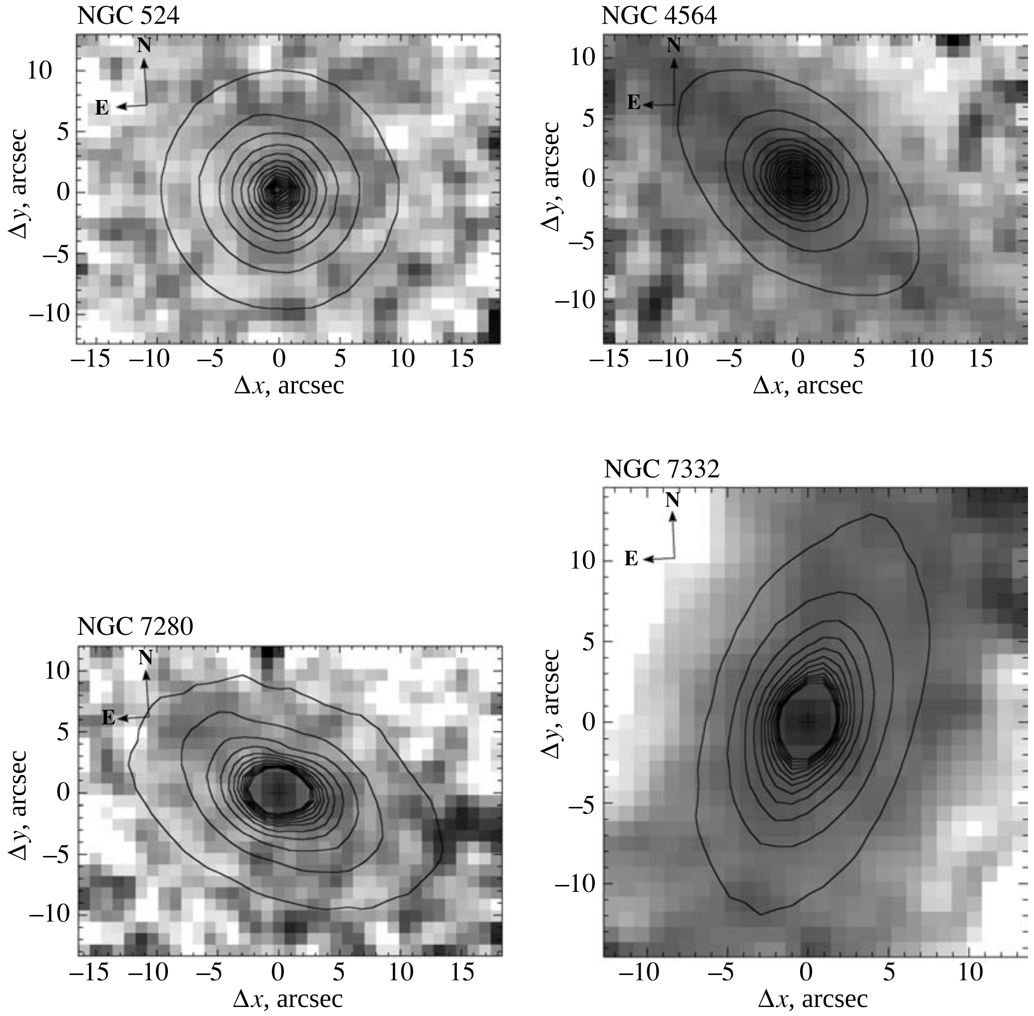

Fig. 2. Maps of the Mgb index in the central regions of four of the galaxies under study (the gray intensity scale); the superimposed isophotes indicate the continuum surface brightness distribution at λ5000 Å.

NGC 1023 constitutes a special, very curious case (Fig. 3). We see from Fig. 3a that the chemically decoupled nucleus is an elongated structure. In our previous paper on this galaxy (Sil'chenko 1999), we decided that we saw the circumnuclear disk edge-on, especially since the structure is elongated roughly along the line of nodes of the global galactic disk. However, we used no kinematic data in our analysis in that paper. Now, Fig. 3 also shows maps of the stellar velocity dispersion and line-of-sight velocities, and these data completely disprove the hypothesis of a circumnuclear disk decoupled in the magnesium line. Instead of the minimum of the stellar velocity dispersion at the center, evidence for the presence of a dynamically cold stellar disk observed, in particular, in NGC 3384 (Sil'chenko *et al.* 2003) or NGC 3623 (Afanasiev and Sil'chenko 2004), we see a maximum; the region of the maximum is not pointlike, as in galaxies where the gravity of a supermassive black hole dominates at the center, but is extended, elongated in a direction of $PA \approx 45°$. Such two-dimensional distributions of the stellar velocity dispersion can be observed at the centers of galaxies with old, dynamically evolved bars; in this case, the extended region of the maximum velocity dispersion is elongated along the bar (Vauterin and Dejonghe 1997). However, the same dynamical numerical models of bars also prescribe a turn of the lines of equal line-of-sight velocities of the ordered stellar motion along the bar, and we see from Fig. 3c that the isovelocities at the center of NGC 1023 turn in exactly the opposite direction, perpendicular to the elongation of the region of enhanced stellar velocity dispersion. To try to interpret this complex combination of orientations, let us compare the position angles of kinematic and photometric features. This comparison is shown in Fig. 4. Here, we used the photometric data obtained at different telescopes, with different

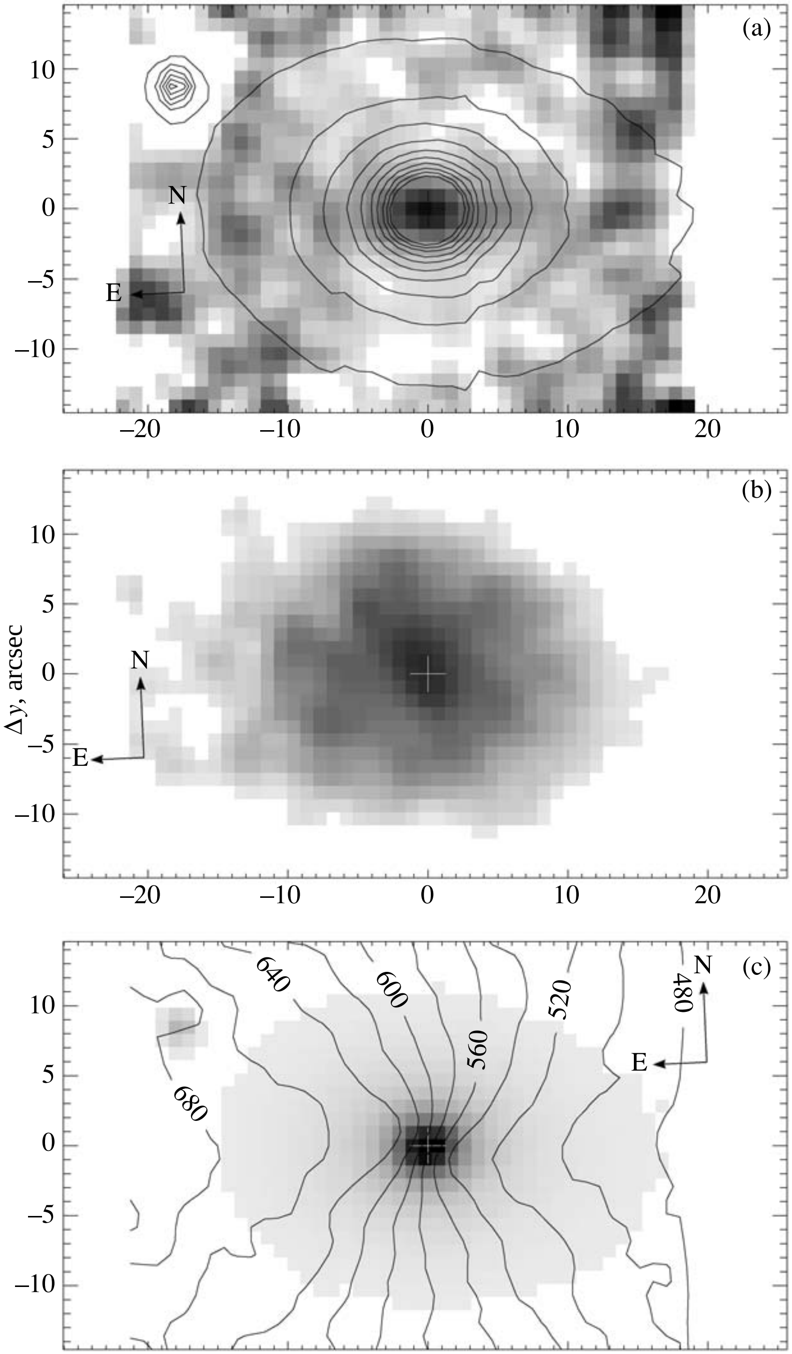

Fig. 3. SAURON data for NGC 1023: (a) the Mgb distribution, the superimposed isophotes indicate the continuum surface brightness distribution; (b) the distribution of stellar velocity dispersion; and (c) the lines of equal velocity (isovelocities) of the stellar line-of-sight velocity field superimposed on the continuum surface brightness map.

spatial resolutions, and in different spectral bands, from green (the $F555W$ filter on the WFPC2/HST camera) to near infrared (the K filter, $\lambda = 2\ \mu$m). All of these data are in excellent agreement at radii $R > 5''$, where the spatial resolution of the instrument does not distort the measurements. In addition to the position angle of the isophotes, the dashed lines in Fig. 4 indicate the orientations of the lines of nodes of the bulge and the disk from Möllenhoff and Heidt (2001), while the solid line indicates the kinematic major axis (the direction of the maximum line-of-sight velocity gradient) of the stars, computed from the velocity

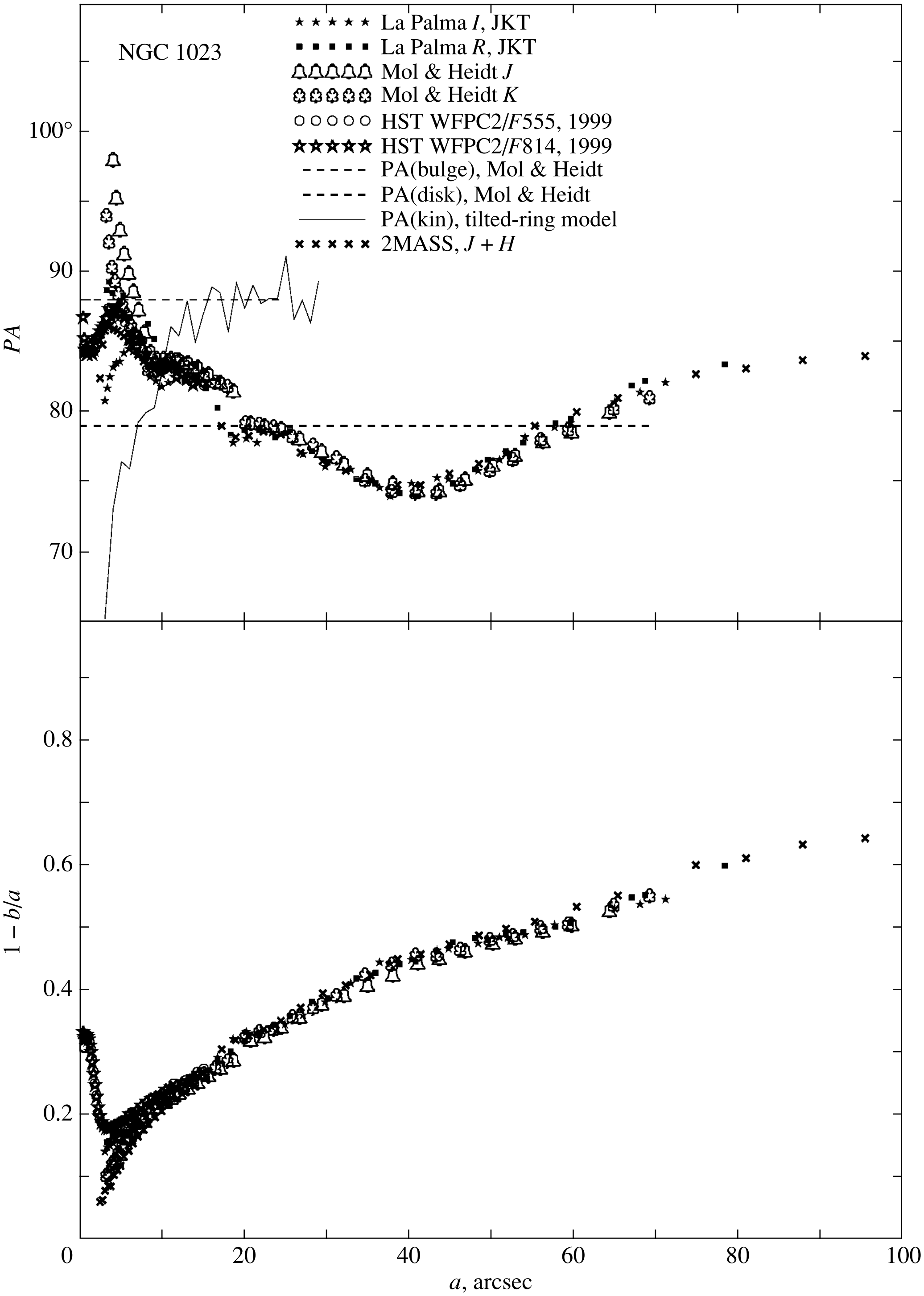

Fig. 4. Results of our isophotal analysis of the surface brightness distributions at various wavelengths in the galaxy NGC 1023, in the upper panel, in comparison with the orientation of the kinematic major axis of the stellar velocity field. We used optical photometric data from the Jacobus Kapteyn 1-m telescope at La Palma and the Hubble Space Telescope and near-infrared data published by Möllenhoff and Heidt (2001) and from the 2MASS survey.

field in Fig. 3 in terms of a tilted-ring model (Begeman 1989) using the DETKA code written for IDL by A.V. Moiseev. The extrema in the $PA(R)$ dependence allow us to diagnose the existence of two elongated photometric structures at the center of NGC 1023. The first, more compact structure with a radius of $\sim 5''$ is elongated in a direction of $PA \geq 88°$; it can be immediately identified with the structure decou-

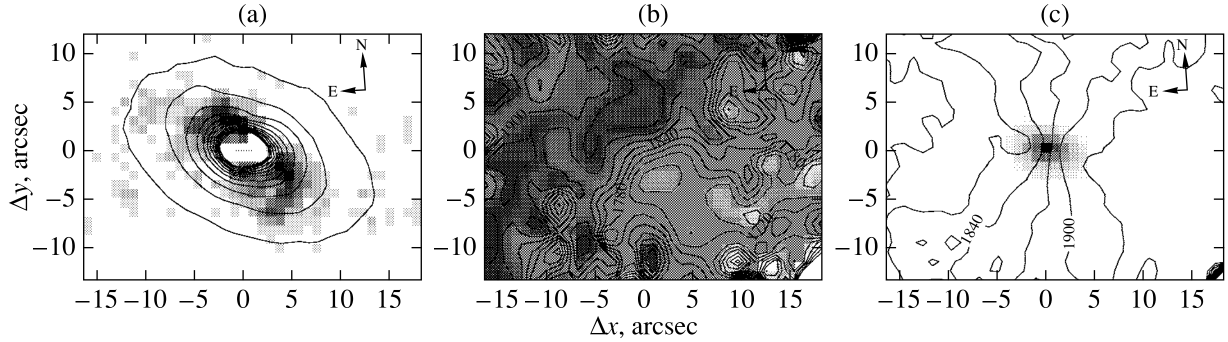

Fig. 5. Results of our SAURON data reduction for NGC 7280: (a) the gray intensity map of the [O III] $\lambda5007$ emission line with superimposed continuum surface brightness isophotes; (b) the ionized-gas velocity field (darker regions correspond to higher velocities; the superimposed isovelocities duplicate the gray-scale data); (c) the isovelocities of the stellar line-of-sight velocity field superimposed on the continuum surface brightness map.

pled in the magnesium line. The second elongated photometric structure in NGC 1023 has a radius of $\sim 40''$ and a position angle of $PA \leq 74°$; clearly, this is just a global bar in the galactic disk, and the distribution of the stellar velocity dispersion is tied to it. Based on MPFS observations of a sample of 13 barred galaxies, Moiseev (2002) pointed out that the stellar velocity dispersion at the centers of even early-type galaxies traces the geometry of the global bar. And what is the nature of the central elongated structure? This is probably just the central part of the triaxial bulge of NGC 1023. That the bulge is triaxial follows at least from the fact that, according to Möllenhoff and Heidt (2001) and our Fig. 4, the major axis of its isophotes does not coincide with the line of nodes of the large galactic disk. In addition, in Fig. 4, the kinematic and photometric major axes at $R < 10''$ diverge in opposite directions relative to the line of nodes; this is a characteristic signature of rotation inside a triaxial potential (Monnet *et al.* 1992; Moiseev and Mustsevoĭ 2000). All scales are in agreement: according to Baggett *et al.* (1998), the bulge in NGC 1023 photometrically dominates over the disk at $R < 15''$, while according to Simien and Prugniel (1997), its dynamical influence is felt up to $R \sim 50''$; hence the agreement between the kinematic major axis and the photometric axis of the bulge in the range of radii $R \sim 15''$–$30''$.

THE INNER POLAR RINGS IN NGC 7280 AND NGC 7332

The circumnuclear gaseous polar rings in disk galaxies was a curious phenomenon that we encountered while looking for chemically decoupled nuclei by means of two-dimensional spectroscopy. Prior to our work, such rings were found only in galaxies of very early types; Bertola and Galletta (1978) introduced a special type of elliptical galaxies by distinguishing five objects with dust lanes along the minor axis. In elliptical galaxies without large-scale gaseous disks, the inner polar rings may well be assumed to result from the accretion of gas from another galaxy. We first discovered inner polar rings of ionized gas in several spiral galaxies (in NGC 2841 (Sil'chenko *et al.* 1997), NGC 7217 (Sil'chenko and Afanasiev 2000), NGC 6340 (Sil'chenko 2000), and NGC 4548 (Sil'chenko 2002b) where the outer gas is much greater in amount than the inner gas and rotates quite regularly in the symmetry plane of the galaxy together with the stars. This combination of nested noncoplanar gaseous disks is in much poorer agreement with the hypothesis of chance single-moment accretion. It has also emerged that the lenticular galaxies where we found inner polar rings, NGC 7280 (Afanasiev and Sil'chenko 2000) and eight more objects (Sil'chenko and Afanasiev 2004), are atypically rich in neutral hydrogen for this type of galaxies; the neutral gas is often concentrated near the plane of the galaxy, but outside its optical disk. When we compared the global structure of the galaxy with the phenomenon of a polar inner ring, we suspected that the concentration of the inner gas in polar orbits could be linked with the existence of a triaxial potential; this link, in particular, was previously suggested by some of the dynamical models by Friedli and Benz (1993).

Using the SAURON data, which have the advantage of a large field of view, we detected new features of the gas distribution and kinematics in galaxies with inner polar rings. Figures 5 and 6 show the results of our data reduction for NGC 7280 and NGC 7332: the line-of-sight velocity field of the gas (as measured in the [O III] $\lambda5007$ emission line) and stars as well as the emission surface brightness distribution against the background of the isophotes of the stellar distribution. In NGC 7280, we found an inner polar ring previously using MPFS data (Afanasiev and Sil'chenko 2000). In NGC 7332, we observed nothing

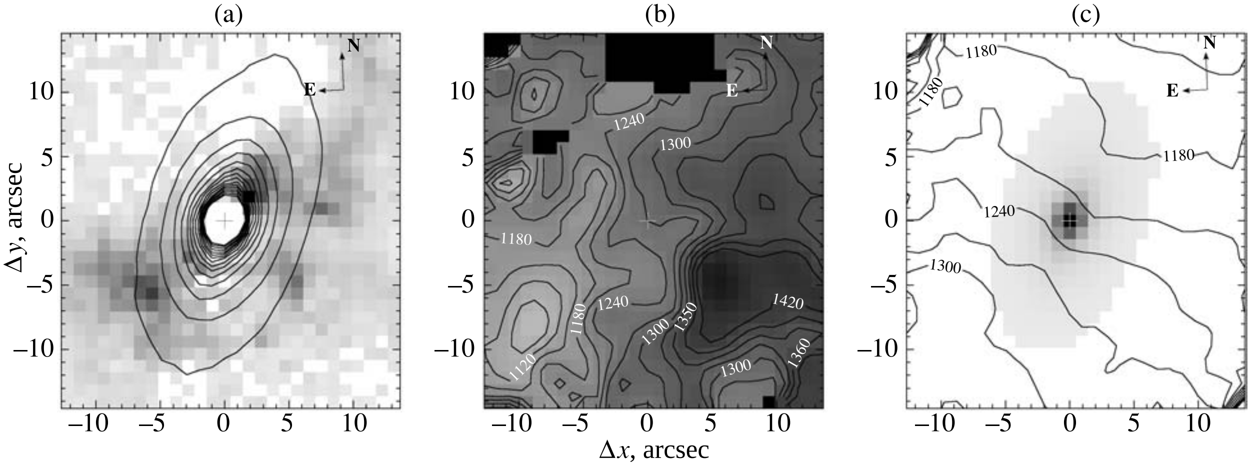

Fig. 6. Same as Fig. 5 for NGC 7332.

of this kind, although the galaxy was studied previously (Sil'chenko 1999). This is probably because the emission is absent in the nucleus itself, but appears only at about 5″ from the center, which is an example of complex gas kinematics around a completely inactive nucleus. According to the SAURON data, the line-of-sight velocity field of the ionized gas in both galaxies is very complex, with a variable pattern of rotation at different distances from the center. A comparison of the gas and stellar velocity fields within $R = 5''{-}7''$ shows an almost polar rotation of the gas relative to the stars in both galaxies. Thus, for example, in NGC 7280, the position angles of the kinematic major axes of the stars and the gas in the ring $R = 2''{-}4''$ are $PA_{\mathrm{kin},*} = 261^\circ \pm 0.5^\circ$ and $PA_{\mathrm{kin,[O\,III]}} = 20^\circ \pm 2^\circ$, respectively; i.e., ΔPA is ∼120° (Fig. 5). In NGC 7332, the picture is not so distinct: the polar gas rotation cannot be traced in full azimuth; the red spot is best seen southwest of the nucleus, and the blue region is much less pronounced in the northeast with a velocity that, nevertheless, differs from the systemic velocity by $\sim{-100}$ km s^{-1} (Fig. 6). The polar gaseous ring of NGC 7332 with a hole inside is probably seen almost edge-on. However, the behavior of the gas at large ($R > 7''$) distances from the center is most curious: the maximum (along the azimuth) intensity of the emission at these radii is observed near the major axis of the continuum isophotes (in NGC 7280, this appears as a weak spiral; in NGC 7332, the gas distribution is more irregular), and the gas at $R > 10''$ within the SAURON field of view rotates in the opposite sense with respect to the stars in both galaxies. In NGC 7332, the extended counterrotating gaseous disk was described by Fisher *et al.* (1994); in NGC 7280, we point out this phenomenon for the first time.

DISCUSSION

The combination of an inner compact polar, or highly tilted, ring and an extended counterrotating gaseous disk coplanar to the stellar disk in a single galaxy has been first detected in our observations. However, it is most interesting that theoreticians predicted this combination long ago. Van Albada *et al.* (1982) considered the accretion of gas onto a rotating triaxial potential. At random mutual orientations of the initial momenta, the gas is eventually concentrated into a stably rotating disk in the plane perpendicular to the largest axis of the ellipsoid. However, since the potential figure rotates in space, the outer gaseous disk will be warped toward the plane orthogonal to the smallest axis of the ellipsoid in such a way that the gas rotates toward the stellar motion inside the ellipsoid. In contrast, another dynamical model, that of Friedli and Benz (1993), starts with the presence of a counterrotating gas in the global galactic disk. Internal instabilities in the stellar disk give rise to a bar; the gas in it gives up its momentum to the stars and sinks to the galactic center. If the gas initially counterrotated, its stable circumnuclear orbits would be highly inclined to the plane of the global disk. Falling to the center, the counterrotating gas escapes from the plane and is concentrated in a polar ring. Based on the currently available data alone, it is hard to say what appeared earlier, the chicken or the egg, i.e., the inner polar ring or the counterrotating gaseous disk. However, we do know that there are medium-sized bars, with a radius of ∼1–2 kpc, in both NGC 7280 and NGC 7332. If this is the case, then the presence of an inner polar gaseous ring with a counterrotating outer gas is inevitable from the viewpoint of any of the models mentioned above.

Having analyzed the data for a factor of 3 to 5 larger field of view than we did previously with the

MPFS data, we confirmed the existence of chemically decoupled (in the magnesium line) nuclei in all five galaxies studied. However, the morphology of the chemically decoupled central regions turned out to be highly varied. In galaxies where the presence of separate circumnuclear stellar disks is known from photometric studies, these disks are also recognized in the distribution of the magnesium index; however, pointlike nuclei with a particularly strong magnesium line are superimposed on extended regions of enhanced metallicity. This inevitably suggests that the secondary starburst at the galactic center was nonuniform in space and, in these specific cases, was more effective in the nucleus than in the circumnuclear disk. In NGC 1023, a galaxy with a large bar, the central extended structure decoupled in the magnesium line turned out to be even not a disk, but a compact triaxial spheroid that is probably coaxial with the triaxial bulge. Whereas the current simulations often demonstrate possibilities for the formation of compact circumnuclear stellar disks during secondary central starbursts, the ways in which triaxial structures (minibars without disks?) are formed are so far completely unimaginable. We wish to emphasize the value of obtaining two-dimensional spectroscopic data for wide fields of view. Such data could allow us to accumulate larger statistical material on the morphology of evolutionally decoupled structures at the centers of galaxies.

ACKNOWLEDGMENTS

I am grateful to A.V. Moiseev from the Special Astrophysical Observatory for the analysis of the stellar velocity field in NGC 1023 using his DETKA code and V.V. Vlasyuk, deputy director of the Special Astrophysical Observatory, for the modification of his two-dimensional spectroscopic data reduction software package to incorporate the specific peculiarities of the SAURON spectrograph. I used observational data obtained with the William Herschel and Jacob Kapteyn telescopes on the La Palma island operated by the Royal Greenwich Observatory at the del Roque de los Muchachos Spanish Observatory of the Canary Islands Institute for Astrophysics and taken from the publicly accessible Isaac Newton Group archive at the Astronomical Data Center of Great Britain as well as data from the NASA/ESA Hubble Space Telescope operated by the Association of Universities for Research in Astronomy under NASA contract NAS 5-26555. In our work, we relied on the capabilities of the Lyon–Meudon Extragalactic Database (LEDA) provided by the LEDA team at the CRAL Lyon Observatory (France) and the NASA/IPAC Extragalactic Database (NED) operated by the Jet Propulsion Laboratory at the California Institute of Technology under a contract with the National Aeronautics and Space Administration (United States). This work was supported by the Russian Foundation for Basic Research (project no. 04-02-16087) and the Federal Target Science and Technology Program "Research and Development in Priority Fields of Science and Technology" (the Oriented Basic Research Block, contract no. 40.022.1.1.1101).

REFERENCES

1. V. L. Afanasiev and O. K. Sil'chenko, Astron. J. **119**, 126 (2000).
2. V. L. Afanasiev and O. K. Sil'chenko, Astron. Astrophys. **429**, 825 (2005).
3. V. L. Afanasiev, O. K. Sil'chenko, and A. V. Zasov, Astron. Astrophys. **213**, L9 (1989).
4. V. L. Afanasiev, V. V. Vlasyuk, S. N. Dodonov, and O. K. Sil'chenko, Preprint No. 54, SAO AN SSSR (Spec. Asrophys. Obs., Acad. Sci. USSR, Nizhniĭ Arkhyz, 1990).
5. R. Bacon, Y. Copin, G. Monnet, *et al.*, Mon. Not. R. Astron. Soc. **326**, 23 (2001).
6. W. E. Baggett, S. M. Baggett, and K. S. J. Anderson, Astron. J. **116**, 1626 (1998).
7. K. Begeman, Astron. Astrophys. **223**, 47 (1989).
8. R. Bender, Astron. Astrophys. **202**, L5 (1988).
9. F. Bertola and G. Galletta, Astrophys. J. **226**, L115 (1978).
10. P. T. de Zeeuw, M. Bureau, E. Emsellem, *et al.*, Mon. Not. R. Astron. Soc. **329**, 513 (2002).
11. D. Fisher, G. Illingworth, and M. Franx, Astron. J. **107**, 160 (1994).
12. D. Friedli and W. Benz, Astron. Astrophys. **268**, 65 (1993).
13. R. Jedrzejewski and P. L. Schechter, Astrophys. J. **330**, L87 (1988).
14. A. V. Moiseev, Pis'ma Astron. Zh. **28**, 840 (2002) [Astron. Lett. **28**, 755 (2002)].
15. A. V. Moiseev and V. V. Musstevoĭ, Pis'ma Astron. Zh. **26**, 657 (2000) [Astron. Lett. **26**, 565 (2000)].
16. C. Möllenhoff and J. Heidt, Astron. Astrophys. **368**, 16 (2001).
17. G. Monnet, R. Bacon, and E. Emsellem, Astron. Astrophys. **253**, 366 (1992).
18. R. F. Peletier, R. L. Davies, G. D. Illingworth, *et al.*, Astron. J. **100**, 1091 (1990).
19. J. Pinkney, K. Gebhardt, R. Bender, *et al.*, Astrophys. J. **596**, 903 (2003).
20. W. Seifert and C. Scorza, Astron. Astrophys. **310**, 75 (1996).
21. O. K. Sil'chenko, Astron. Zh. **74**, 643 (1997) [Astron. Rep. **41**, 567 (1997)].
22. O. K. Sil'chenko, Astron. J. **117**, 2725 (1999).
23. O. K. Sil'chenko, Astron. J. **120**, 741 (2000).
24. O. K. Sil'chenko, ASP Conf. Ser. **282**, 121 (2002a).
25. O. K. Sil'chenko, Pis'ma Astron. Zh. **28**, 243 (2002b) [Astron. Lett. **28**, 207 (2002b)].
26. O. K. Sil'chenko and V. L. Afanasiev, Astron. Astrophys. **364**, 479 (2000).

27. O. K. Sil'chenko and V. L. Afanasiev, Astron. J. **127**, 2641 (2004).
28. O. K. Sil'chenko, V. L. Afanasiev, and V. V. Vlasyuk, Astron. Zh. **69**, 1121 (1992) [Sov. Astron. **36**, 577 (1992)].
29. O. K. Sil'chenko, A. V. Moiseev, V. L. Afanasiev, *et al.*, Astrophys. J. **591**, 185 (2003).
30. O. K. Sil'chenko, V. V. Vlasyuk, and A. N. Burenkov, Astron. Astrophys. **326**, 941 (1997).
31. F. Simien and Ph. Prugniel, Astron. Astrophys., Suppl. Ser. **126**, 519 (1997).
32. K. M. Strom and S. E. Strom, Astron. J. **83**, 73 (1978).
33. S. E. Strom, K. M. Strom, J. W. Goad, *et al.*, Astrophys. J. **204**, 684 (1976).
34. T. S. Van Albada, C. G. Kotanyi, and M. Schwarzschild, Mon. Not. R. Astron. Soc. **198**, 303 (1982).
35. P. Vauterin and H. Dejonghe, Mon. Not. R. Astron. Soc. **286**, 812 (1997).
36. V. V. Vlasyuk, Izv. Spets. Astrofiz. Obs., Ross. Akad. Nauk **36**, 107 (1993).
37. A. Wirth, Astron. J. **86**, 981 (1981).
38. G. Worthey, Astrophys. J., Suppl. Ser. **95**, 107 (1994).
39. G. Worthey, S. M. Faber, J. J. Gonzalez, *et al.*, Astrophys. J., Suppl. Ser. **94**, 687 (1994).

Translated by V. Astakhov

Astronomy Letters, Vol. 31, No. 4, 2005, pp. 239–244. Translated from Pis'ma v Astronomicheskiĭ Zhurnal, Vol. 31, No. 4, 2005, pp. 262–268.
Original Russian Text Copyright © 2005 by Malafeev, Zinchenko, Pirogov, Johansson.

Analysis of Spatial Temperature Variations in Regions of Massive Star Formation

S. Yu. Malafeev[1,2], I. I. Zinchenko[1,2*], L. E. Pirogov[1], and L. E. B. Johansson[3]

[1] *Institute for Applied Physics, Russian Academy of Sciences, ul. Ul'yanova 46, Nizhni Novgorod, 603600 Russia*
[2] *Nizhni Novgorod State University, pr. Gagarina 23, Nizhni Novgorod, 603950 Russia*
[3] *Onsala Space Observatory, Chalmers University of Technology, S-43992 Onsala, Sweden*

Received October 5, 2004

Abstract—Using the 20-m Onsala Observatory telescope (Sweden), we performed observations of the $CH_3C_2H(6-5)$ line toward several regions of massive star formation to estimate the kinetic temperature of the gas and study its variations over the sources. Intense lines were detected in five objects. For these, we estimated the kinetic temperature of the gas near the CS and N_2H^+ molecular emission peaks by the method of population diagrams. A significant temperature difference between these peaks is noticeable only in W3 and, to a lesser degree, in DR 21. In the remaining cases, it is insignificant. This indicates that the chemical differentiation of the molecules in these regions cannot be associated with temperature variations. The kinetic temperature determined from methyl acetylene observations is usually slightly higher than the temperature estimated from ammonia observations. This is probably because the methyl acetylene emission originates in denser, i.e., deeper and hotter layers of the cloud. *© 2005 Pleiades Publishing, Inc.*

Key words: *interstellar medium, gaseous nebulae, giant molecular clouds, interstellar molecules,* CH_3C_2H*, radio lines.*

INTRODUCTION

At present, studies of the individual star-forming dense cores of molecular clouds are often replaced with systematic studies of representative samples of objects selected according to certain criteria. This makes it possible to perform a statistical analysis of the derived physical parameters, to reveal correlations between these parameters, and to determine the evolutionary status of objects, which in the long run inevitably lead to a faithful theoretical description of the star formation process. Recently, systematic studies that initially included nearby low-mass cores in which isolated stars with a mass of the order of the solar mass are mainly formed were also actively carried out concerning the massive cores of farther giant molecular clouds (GMCs) where higher-mass stars are formed, as suggested by the presence of water-vapor masers and/or bright pointlike infrared sources in them.

In recent years, the emission regions in lines of such molecules, tracers of a dense gas, as CS, HCN, HCO^+, N_2H^+, and others have been mapped toward several dozen dense cores associated with water masers and bright infrared sources (see, e.g., Zinchenko *et al.* 1995, 1998, 2000; Pirogov *et al.* 2003). This allowed us to determine such important parameters of the cores as the size, the velocity dispersion of internal gas motions, the mean density, and the mass and to draw conclusions about the density and velocity dispersion distributions in several cases. At the same time, differences in the distributions of the emission regions of various molecules were found in a number of objects. The differences were particularly large between the CS (2–1) and N_2H^+ (1–0) distributions (the corresponding results are being prepared for publication), which is probably not related to the gas density variations in the objects, but is indicative of differences between the distributions of the relative number densities of the above molecules.

The freezing out of some of the molecules on dust grains with different efficiencies is known to be responsible for the difference between the relative number densities of the molecules in the central regions of cold low-mass cores. In particular, Bergin *et al.* (2001) showed that the freezing-out efficiency for CS could be fairly high. At the same time, the N_2H^+ (1–0) distributions in low-mass cores correlate well with the continuum dust emission, and the freezing-out efficiency for this molecule is probably much lower (Caselli *et al.* 2002). In high-mass cores, the freezing out of molecules on dust could probably take place at

---

[*] E-mail: `zin@appl.sci-nnov.ru`

Table 1. List of sources

Object	$\alpha(1950)$	$\delta(1950)$
AFGL 6366	$06^{\rm h}05^{\rm m}40\overset{\rm s}{.}1$	$21°31'16''$
DR 21	20 37 13.5	42 12 15
S140	22 17 41.1	63 03 44
S255	06 09 57.9	18 00 12
W3	02 21 40.8	61 53 26

some distance from the star, in regions with a low dust temperature (<30–40 K).

Therefore, information about the temperature of the regions demonstrating a difference between the CS (2–1) and N_2H^+ (1–0) distributions is of great importance in establishing the causes of these differences. A convenient "thermometer" for a dense gas is methyl acetylene, CH_3C_2H. Thus, for example, Bergin *et al.* (1994) showed that the temperature of a gas with a density $n \gtrsim 10^4$ cm^{-3} could be reliably estimated using observations of the $J = 6$–5 $(K = 0, 1, 2)$ transitions in this molecule.

In this paper, we present our measurements of the kinetic temperature for five GMC cores (AFGL 6366, DR 21, S140, S255, and W3). The temperature was determined at various points of each core corresponding to the CS (2–1) and N_2H^+ (1–0) intensity peaks using the methyl acetylene CH_3C_2H emission spectra measured on the 20-m OSO radio telescope in December 2002.

OBSERVATIONS

To obtain information about the variations in the kinetic temperature of the gas in regions of massive star formation demonstrating differences between the CS and N_2H^+ distributions, we selected five objects. A list of the sources with their positions is given in Table 1.

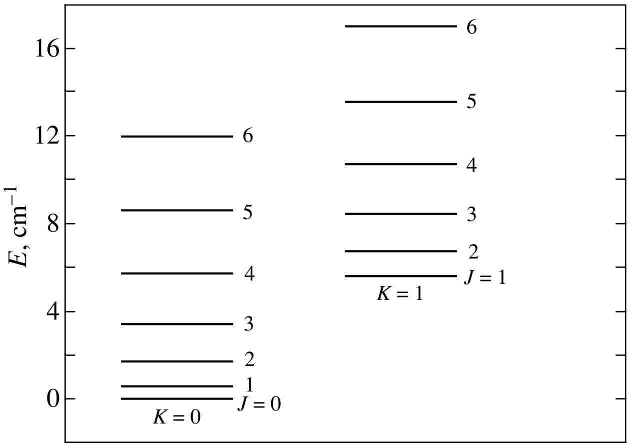

Fig. 1. Energy level diagram for of methyl acetylene.

We observed the $J = 6$–5 transition of the CH_3C_2H molecule at 102.5 GHz toward these sources in December 2002 on the 20-m radio Onsala Space Observatory telescope, Sweden. The parameters of the telescope and the receiving equipment were described by Zinchenko *et al.* (1998, 2000) and Pirogov *et al.* (2003). In these measurements, the system noise temperature was ~400 K, and the spectral resolution of the autocorrelation spectrum analyzer was 50 kHz, which corresponds to 0.15 km s^{-1}.

Apart from the sources listed in Table 1, we observed the cloud S187. However, the intensity of the CH_3C_2H emission in it was too low for the temperature variations to be analyzed.

THE THEORY BEHIND THE METHOD

The methyl acetylene molecule (CH_3C_2H) belongs to the symmetric-top type and is a reliable tracer of the kinetic temperature, since the temperature and density effects on the excitation of rotational transitions can be separated for it (see Bergin *et al.* (1994) and references therein). For a symmetric-top molecule, the energy levels of the rotational spectrum are described by the formula (Townes and Shawlow 1955)

$$E = hBJ(J+1) + h(A-B)K^2, \qquad (1)$$

where A and B are the rotational constants, h is the Planck constant, J is the quantum number that determines the angular momentum, and K is the quantum number that determines the projection of the angular momentum onto the symmetry axis of the molecule. Figure 1 shows the energy level diagram for methyl acetylene. The transitions between various K ladders are forbidden by selection rules ($\Delta J = 0, \pm 1; \Delta K = 0$).

At densities $n \gtrsim 10^4$ cm^{-3}, the relative populations of the $J = 5, 6$ $(K = 0, 1, 2, 3)$ levels approach the values that these would have at local thermodynamic equilibrium, since the populations of these levels are determined mainly by collisions. The relative populations of two molecular levels at thermodynamic equilibrium are defined by the Boltzmann formula

$$\frac{N_{\rm u}}{N_{\rm l}} = \frac{g_{\rm u}}{g_{\rm l}} \exp\left(-\frac{\Delta E_{\rm ul}}{kT_{\rm ex}}\right), \qquad (2)$$

where $N_{\rm u}, N_{\rm l}, g_{\rm u}$, and $g_{\rm l}$ are the column densities and statistical weights of the upper and lower levels, respectively; $\Delta E_{\rm ul}$ is the energy difference between the two levels; $T_{\rm ex}$ is the excitation temperature; and k is the Boltzmann constant. Taking into account the fact that the line optical depth is much smaller than unity, assuming local thermodynamic equilibrium, where the excitation temperatures of all levels (2) are equal to the kinetic temperature (T), and ignoring the cosmic microwave background, we obtain the following expression from the solution of the radiative transfer equation:

$$\frac{3k\int T_A dv}{8\pi^3 \nu S \mu^2} = \frac{N_{\text{tot}}}{Z} g_I g_K \exp\left(-\frac{E_{\text{u}}}{T}\right), \qquad (3)$$

where S is the line strength, which is equal to $(J^2 - K^2)/J$ for a symmetric-top molecule; ν is the transition frequency; E_{u} is the energy of the upper level in Kelvins; μ is the dipole moment; $\int T_A dv$ is the integrated line intensity (T_A is the brightness temperature in the line, ν is the radial velocity); N_{tot} is the total molecular column density; Z is the partition function; and g_K is the statistical weight of the K level attributable to the fact that the K and $-K$ levels are indistinguishable for a symmetric-top molecule:

$$g_K = \begin{cases} 1, & K = 0 \\ 2, & K \neq 0. \end{cases}$$

g_I is the statistical weight normalized to $(2I + 1)^3$ (I is the nuclear spin equal to 1/2 for methyl acetylene) and attributable to the nuclear spin (Kuiper *et al.* 1984):

$$g_I = \begin{cases} 1/2, & K = 0, 3, 6, 9, \ldots \\ 1/4, & K \neq 0, 3, 6, 9, \ldots. \end{cases}$$

Finding the logarithm of Eq. (3) yields

$$\ln\left(\frac{\int T_A dv}{g_I g_K (J^2 - K^2)}\right) = -\frac{E_{\text{u}}}{T} - \ln\left(\frac{3kJZ}{8\pi^3 \nu \mu^2 N_{\text{tot}}}\right). \qquad (4)$$

Thus, if we plot $\ln\left(\int T_A dv/[g_I g_K (J^2 - K^2)]\right)$ against E_{u} and approximate it by a straight line, the kinetic temperature T will be found as the reciprocal of the slope the straight line.

DATA PROCESSING

Figure 2 shows the emission spectrum for CH_3C_2H in the cloud S140 at the point with coordinates of $\Delta\alpha = 40''$ and $\Delta\delta = 20''$ relative to the positions given in Table 1. We see four peaks in it that correspond to $K = 0, 1, 2, 3$ (from left to right). The effective antenna temperature is along the vertical axis. The spectral range is shown in velocity units. The center of the range ($K = 2$) corresponds to the radial velocity of the gas for the cloud in question.

Table 2. Parameters of the $J = 6{-}5$ transition for CH_3C_2H

K	ν, MHz	E_{u}, K	ΔV, km s^{-1}	g_I	g_K
0	102547.9842	17.226	−22.920	1/2	1
1	102546.0241	24.427	−17.189	1/4	2
2	102540.1447	46.029	0	1/4	2
3	102530.3487	82.033	28.640	1/2	2

Table 3. Kinetic temperatures at various points of the cores studied and molecules with emission peaks at these points

Object	$\Delta\alpha$	$\Delta\delta$	T, K	Emission peak
W3	$20''$	$-40''$	52.6 ± 3.1	CS
	160	−160	30.7 ± 0.8	N_2H^+
AFGL6366	0	20	39.4 ± 2.8	CS, N_2H^+
	100	60	35.7 ± 4.6	CS, N_2H^+
DR 21	−40	−80	33.8 ± 0.9	
	−40	40	21.8 ± 1.1	
	0	−80	15.6 ± 0.3	
	0	−40	28.8 ± 0.1	N_2H^+
	0	0	33.4 ± 2.7	CS
	0	40	26.7 ± 0.9	
	0	80	24.5 ± 1.4	
S140	40	40	26.0 ± 1.2	N_2H^+
	40	20	27.8 ± 1.6	N_2H^+
	80	40	33.4 ± 0.2	
	80	0	38.6 ± 4.2	
	40	0	29.8 ± 1.5	
	0	0	30.6 ± 0.7	CS
S255	0	60	34.9 ± 1.4	N_2H^+
	0	0	34.5 ± 1.0	CS

Table 2 gives parameters of the $J = 6{-}5$ transition for CH_3C_2H.

We processed the spectra using the CLASS package. The processing procedure included baseline subtraction, the Gaussian fitting of each line, and the calculation of the integrated intensity $\int T_A dv$. In our fitting, we fixed the separation between the lines. The line widths were assumed to be identical.

A total of 19 spectra were processed for five clouds. For each spectrum, we plotted $\ln\left(\int T_A dv/[g_I g_K \times (J^2 - K^2)]\right)$ against E_{u}, found the straight line passing through the experimental data by the least-squares method, and determined the kinetic temperature. Figure 3 shows the dependence for the spectrum displayed in Fig. 2.

Table 3 gives the calculated kinetic temperatures for the five cores studied and lists the molecules whose intensity peaks correspond to these points.

Figure 4 shows the spatial distribution of the kinetic temperatures in the clouds DR 21 (left) and S140.

Figure 5 shows the dependence of the temperature in the cloud DR 21 on $\Delta\delta$ for $\Delta\alpha = 0''$ fitted by a cubic polynomial.

ANALYSIS OF RESULTS

The results given in Table 3 indicate that significant variations in kinetic temperature are observed only in DR 21 and W3. In AFGL 6366 and S255, there are no statistically significant temperature differences between the observed positions. These objects were observed previously in lines of CO, NH_3, etc., which can also be used to estimate the temperature. There are dust temperature estimates for some of them. However, these estimates depend on the rather uncertain exponent β of the frequency dependence of the dust emissivity. A change in β from 1 to 2 reduces the temperature estimate by $\sim$20%. Below, we compare the available temperature estimates for these sources.

AFGL 6366. The infrared source AFGL 6366 (IRAS 06056+2131) was observed in the NH_3 (1,1) and (2,2) lines on the 100-m Effelsberg radio telescope (Schreyer *et al.* 1996). However, no map of the source was obtained. According to these data, the kinetic temperature of the gas was 26 K. The dust temperature estimated from IRAS data at 60 and 100 μm was 32.3 K. Our estimate of the kinetic temperature is close to this estimate of the dust temperature and slightly exceeds the kinetic temperature estimated from the ammonia observations. The positions that we observed correspond to two emission peaks with slightly differing chemical compositions. Our results indicate that the temperatures of these peaks are almost identical.

W3. The W3 region has been an object of many studies. Of primary interest to us are the detailed observations of the ammonia (1,1) and (2,2) lines (Tieftrunk *et al.* 1998). Their estimate of the kinetic temperature was 44 K near our position $(20'', -40'')$ and 25 K for the position $(160'', -160'')$. The former and the latter correspond to the CS and N_2H^+ emission peaks, respectively. A comparison with Table 3 shows that here the temperatures found from the CH_3C_2H observations slightly exceed the temperatures found from the ammonia observations. However, their ratio is the same. The temperature in the region of the CS emission peak is much higher than that in the N_2H^+ emission region. According to the observations by Werner *et al.* (1980), the dust color temperatures near the point $(20'', -40'')$ must be within the range 70–80 K ($\beta = 1$).

DR 21. The source DR 21 was observed previously in methyl acetylene lines. The measurements were carried out on the 11-m NRAO paraboloid (Kuiper *et al.* 1984). No map of the source was obtained. According to the data by Kuiper *et al.*, the kinetic temperature near the cloud center is 33.0 K, which is almost equal to our estimate (33.4 K). In addition, Mangum *et al.* (1992) observed DR 21 in the ammonia (1,1) and (2,2) lines on the NRAO Very Large Array. They found the kinetic temperatures for 17 positions, but no measurements were made near the points $(0'', -80'')$, $(-40'', 80'')$, and $(0'', 80'')$. Their temperature estimate was 32 K near the positions $(0'', 0'')$ and $(0'', 40'')$, 23 K near $(-40'', 40'')$, and 25 K near $(0'', -40'')$. A comparison with Table 3 shows that the temperatures determined from CH_3C_2H and NH_3 are close. The maximum difference is 5.3 K for the position $(0'', 40'')$. A possible cause of the temperature difference is that the positions of the measurements do not coincide: one of the coordinates always differs by $6''$ as a minimum and $10''$ as a maximum. According to the data from Harvey *et al.* (1986), the dust color temperatures near the points $(0'', 0'')$, $(0'', 80'')$, and $(0'', -80'')$ were 41, 36, and 38 K, respectively ($\beta = 1$). According to Chandler *et al.* (1993), the dust temperature in the region of the CS emission peak is $\sim$40 K.

S140. Like DR 21, the source S140 was observed previously in methyl acetylene lines (Kuiper *et al.* 1984). No map of this source was obtained either. The kinetic temperature of the cloud center, 32.1 ± 6.7 K, is very close to our estimate (30.6 ± 0.7 K). This object has been repeatedly observed in the ammonia (1,1) and (2,2) lines; in particular, the source was studied by Ungerechts *et al.* (1986) using the 100-m MPIfR telescope in Effelsberg. According to their data, the temperatures for three positions, $(0'', 0'')$, $(40'', 0'')$, and $(40'', 40'')$, were found to be appreciably lower than our values (about 20 K). This corresponds to the general trend: methyl acetylene observations usually yield higher kinetic temperatures than ammonia observations. This is probably because methyl acetylene is excited in a denser gas than ammonia, i.e., closer to the cloud center where the temperature is higher. According to IRAS data (Wu and Evans 1989), the dust temperature at the point $(0'', 0'')$ was 34 K for $\beta = 2$, which is close to our estimate. Just as most of the other molecules' high-density traces, the CS emission peak almost coincides with the cloud center (Zhou *et al.* 1994). The

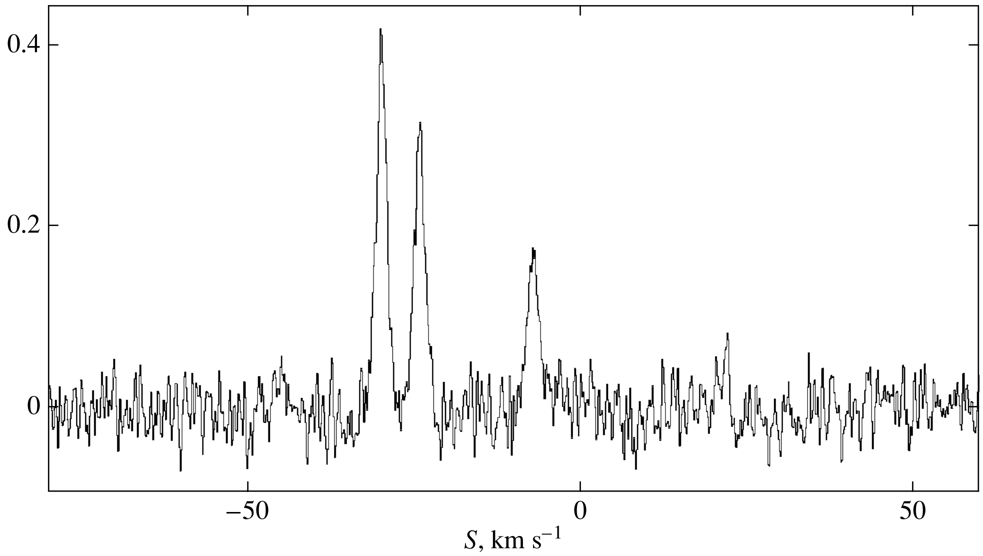

Fig. 2. The spectrum of the CH_3C_2H emission in the cloud S140 from the point with relative coordinates of $\Delta\alpha = 40''$, $\Delta\delta = 20''$.

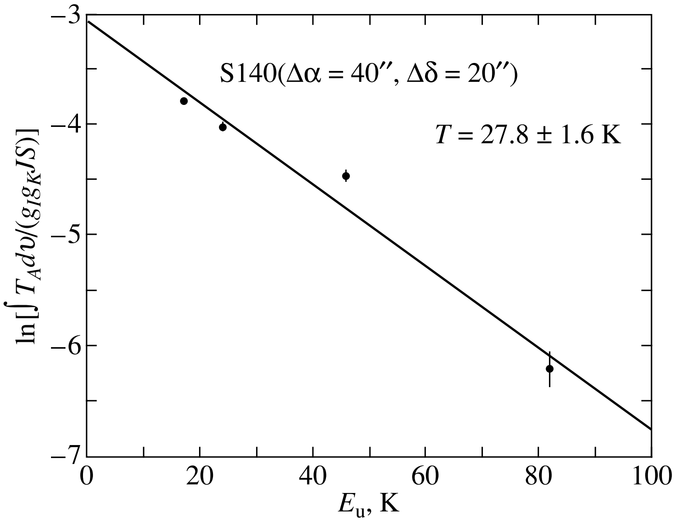

Fig. 3. Rotational diagram for the CH_3C_2H emission spectrum in the cloud S140 ($\Delta\alpha = 40''$, $\Delta\delta = 20''$).

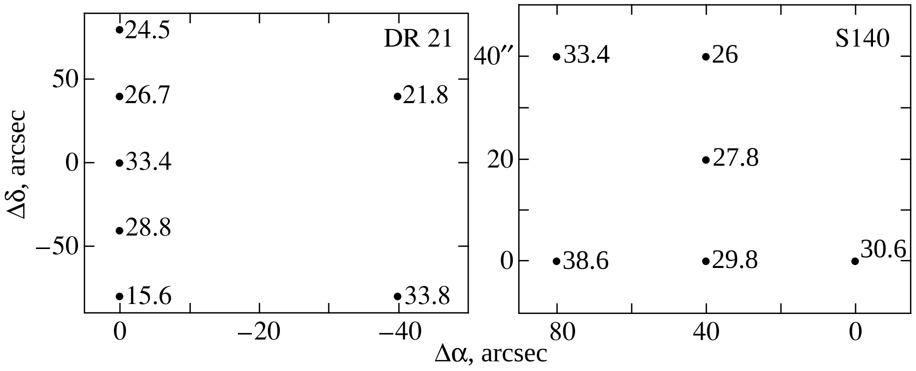

Fig. 4. Spatial distribution of the kinetic temperature in the clouds DR 21 and S140.

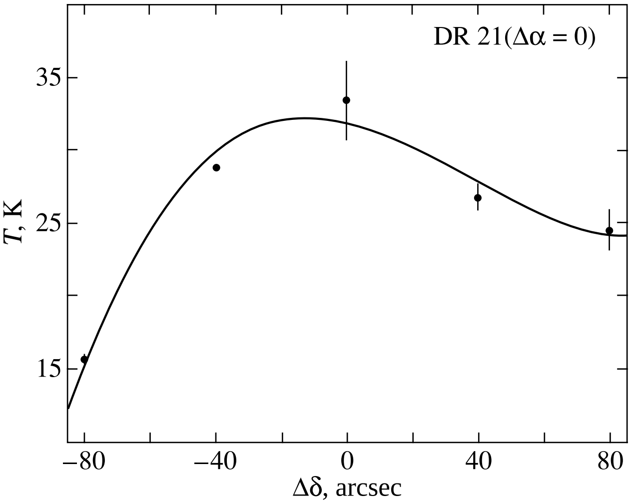

Fig. 5. Dependence of the temperature in the cloud S140 on $\Delta\delta$ for $\Delta\alpha = 0''$ fitted by a cubic polynomial.

N_2H^+ emission peak is shifted to $\sim(+40'', +20'')$. As we see from Table 3, the temperature here was ~27 K, i.e., only slightly lower than the temperature at the point $(0'', 0'')$ (~30 K).

S255. The kinetic temperature in S255 was estimated from ammonia observations (Zinchenko *et al.* 1997). At the point $(0'', +80'')$, it was found to be 23 ± 1 K. At the central position, the uncertainty in the estimated temperature was too large, and this estimate is not given in the above paper. According to Schreyer *et al.* (1996), the kinetic temperature at the point $(0'', 0'')$ calculated from ammonia lines was 30.8 K, and the dust temperature found from IRAS data was 31.1 K ($\beta = 2$).

CONCLUSIONS

In this paper, we have determined the kinetic temperatures at various points in the cores of five GMCs using CH_3C_2H (6–5) observations. The goal of this study was to test the hypothesis about a significant difference between the temperatures in the regions corresponding to the CS (2–1) and N_2H^+ (1–0) emission peaks. In two clouds (DR 21 and W3), we clearly see a significant spatial temperature variation; in the three remaining clouds (AFGL 6366, S140, S255), it is insignificant. Thus, the chemical composition variations in these objects are probably not associated with temperature effects. At the same time, it is worth noting that the temperature of the regions corresponding to the N_2H^+ emission peaks is slightly lower than that for the CS emission peaks.

Our results also indicate that the kinetic temperature determined from methyl acetylene observations is usually slightly higher than the temperature obtained from ammonia observations. This is probably because the methyl acetylene emission originates in denser, i.e., deeper and hotter layers of the cloud.

ACKNOWLEDGMENTS

This work was supported by the Russian Foundation for Basic Research (project no. 03-02-16307), the Program for Support of Leading Scientific Schools (project no. NSh-1483), and the Extended Objects in the Universe program of the Physical Science Branch of the Russian Academy of Sciences.

REFERENCES

1. E. A. Bergin, C. R. Ciardi, C. J. Lada, *et al.*, Astrophys. J. **557**, 209 (2001).
2. E. A. Bergin, P. F. Goldsmith, R. L. Snell, *et al.*, Astrophys. J. **431**, 674 (1994).
3. P. Caselli, P. J. Benson, P. C. Myers, and M. Tafalla, Astrophys. J. **572**, 238 (2002).
4. C. J. Chandler, W. K. Gear, and R. Chini, Mon. Not. R. Astron. Soc. **260**, 337 (1993).
5. P. M. Harvey, M. Joy, D. F. Lester, and B. A. Wilking, Astrophys. J. **300**, 737 (1986).
6. T. B. H. Kuiper, E. N. R. Kuiper, and D. F. Dickinson, Astrophys. J. **276**, 211 (1984).
7. J. G. Mangum, A. Wootten, and L. G. Mundy, Astrophys. J. **388**, 467 (1992).
8. L. Pirogov, I. Zinchenko, P. Caselli, *et al.*, Astron. Astrophys. **405**, 639 (2003).
9. K. Schreyer, T. Henning, C. Koempe, and P. Harjunpää, Astron. Astrophys. **306**, 267 (1996).
10. A. R. Tieftrunk, S. T. Megeath, T. L. Wilson, and J. T. Rayner, Astron. Astrophys. **336**, 991 (1998).
11. C. H. Townes and A. L. Schawlow, *Microwave Spectroscopy* (McGraw-Hill, New York, 1955; Inostrannaya Literatura, Moscow, 1959).
12. H. Ungerechts, C. M. Walmsley, and G. Winnewisser, Astron. Astrophys. **157**, 207 (1986).
13. M. W. Werner, E. E. Becklin, I. Gatley, *et al.*, Astrophys. J. **242**, 601 (1980).
14. Y. Wu and N. J. Evans II, Astrophys. J. **340**, 307 (1989).
15. S. Zhou, H. M. Butner, N. J. Evans, *et al.*, Astrophys. J. **428**, 219 (1994).
16. I. Zinchenko, C. Henkel, and R. Q. Mao, Astron. Astrophys. **361**, 1079 (2000).
17. I. Zinchenko, Th. Henning, and K. Schreyer, Astrophys. J., Suppl. Ser. **124**, 385 (1997).
18. I. Zinchenko, K. Mattila, and M. Toriseva, Astron. Astrophys., Suppl. Ser. **111**, 95 (1995).
19. I. Zinchenko, L. Pirogov, and M. Toriseva, Astron. Astrophys., Suppl. Ser. **133**, 337 (1998).

Translated by G. Rudnitskiĭ

Astronomy Letters, Vol. 31, No. 4, 2005, pp. 245–257. Translated from Pis'ma v Astronomicheskiĭ Zhurnal, Vol. 31, No. 4, 2005, pp. 269–283.
Original Russian Text Copyright © 2005 by Lozinskaya, Komarova, Moiseev, Blinnikov.

New Observations of the Pulsar Wind Nebula in the Supernova Remnant CTB 80

T. A. Lozinskaya[1]*, V. N. Komarova[2], A. V. Moiseev[2], and S. I. Blinnikov[3]

[1] *Sternberg Astronomical Institute, Universitetskiĭ pr. 13, Moscow, 119992 Russia*
[2] *Special Astrophysical Observatory, Russian Academy of Sciences, Nizhniĭ Arkhyz,*
357147 Karachai-Cherkessian Republic, Russia
[3] *Institute for Theoretical and Experimental Physics, ul. Bol'shaya Cheremushkinskaya 25,*
Moscow, 117259 Russia

Received November 15, 2004

Abstract—We investigated the kinematics of the pulsar wind nebula (PWN) in the old supernova remnant CTB 80 using the Fabry–Perot interferometer of the 6-m Special Astrophysical Observatory telescope. In addition to the previously known expansion of the system of bright filaments with a velocity of 100–200 km s^{-1}, we detected weak high-velocity features in the Hα line at least up to velocities of 400–450 km s^{-1}. We analyzed the morphology of the PWN in the Hα, [S II], and [O III] lines using HST archival data and discuss its nature. The shape of the central filamentary shell, which is determined by the emission in the [O III] line and in the radio continuum, is shown to be consistent with the bow-shock model for a significant (about 60°) inclination of the pulsar's velocity vector to the plane of the sky. In this case, the space velocity of the pulsar is twice as high as its tangential velocity, i.e., it reaches $\simeq$500 km s^{-1}, and PSR B1951+32 is the first pulsar whose radial velocity about 40 km s^{-1} has been estimated from PWN observations. The shell-like Hα-structures outside the bow shock front in the east and the west could be associated with both the pulsar's jets and the pulsar wind breakthrough due to the layered structure of the extended CTB 80 shell. © *2005 Pleiades Publishing, Inc.*

Key words: *supernovae and supernova remnants, pulsar wind nebulae, models.*

INTRODUCTION

CTB 80 is a classic example of a supernova remnant (SNR) with a fast-moving pulsar at a late stage of the pulsar's interaction with a very old shell.

The radio image of CTB 80 is represented by three extended (about 30′) ridges that converge in the region of a bright compact core (Velusami and Kundu 1974; Velusami *et al.* 1976; Angerhofer *et al.* 1981; Strom *et al.* 1984; Mantovani *et al.* 1985; Strom 1987; Castelleti *et al.* 2003, and references therein). This unusual (for SNRs) morphology ceased to be puzzling in 1988, when, on the one hand, the 39.5-ms pulsar PSR B1951+32 was discovered in the core (Kulkarni *et al.* 1988; Fruchter *et al.* 1988) and, on the other hand, Fesen *et al.* (1988) identified an extended infrared shell that stretched the radio ridges in the northeast and assumed that precisely this infrared shell represents a very old SNR. The radio ridges with a steep spectrum ($\alpha \simeq -0.7$) correspond to the part of the shell into the compressed magnetic field of which the approached pulsar injected fresh relativistic particles, thereby reanimating its synchrotron radio emission. Subsequently, an H I shell that coincides with the infrared shell and is expanding with a velocity of 72 km s^{-1}, yielding a kinematic SNR age of 7.7×10^4 yr, was also identified (Koo *et al.* 1990, 1993). The characteristic age of the pulsar PSR B1951+32 is $t \simeq 10^5$ yr (Kulkarni *et al.* 1988; Fruchter *et al.* 1988).

The pulsar wind nebula (PWN) is represented by a bright compact (45″) core with a flat spectrum ($\alpha \simeq 0.0$). The core lies at the western boundary of a $10' \times 6'$ plateau with a steeper spectrum ($\alpha \simeq -0.3$) elongated in the east–west direction. Recently, Migliazzo *et al.* (2002) detected the motion of the pulsar with a velocity of 240 km s^{-1} in a direction that confirms the possibility of its birth inside the infrared and H I shells.

The stage of pulsar wind interaction with a very old shell observed in CTB 80 seems most complex in the evolutionary chain of PWNs, from young SNRs where the pulsar interacts with the SN ejection to pulsars that have already escaped from the old SNR.

---

*E-mail: `lozinsk@sai.msu.ru`

The difficulty lies in the matter density in the cooled old shell behind the front of the decelerated shock (and, hence, the density of the compressed interstellar magnetic field) being several hundred times higher than the ambient density and the shell structure is unpredictable in advance. In addition, the rotational energy loss by the pulsar PSR B1951+32 is large ($\dot{E} = 3.7 \times 10^{36}$ erg s^{-1}, as estimated by Kulkarni *et al.* 1988), which is comparable to the energy input from the young Vela X pulsar.

Various distance estimates for CTB 80 and the pulsar PSR B1951+32 lie within the range 1.5–2.5 kpc (see Koo *et al.* 1993; Strom and Stappers 2000; and references therein); we use the universally accepted distance of 2 kpc.

In this paper, we present our observations of the PWN in CTB 80 with the 6-m Special Astrophysical Observatory (SAO) telescope and analyze narrow-band observational data from the HST archive.

We describe the observing and data reduction techniques. We present the results of our observations: we consider the PWN morphology in various lines, construct the radial velocity field in the Hα line, and detected weak emission features whose velocities (up to 400–450 km s^{-1}) exceed significantly the expansion velocity of the system of bright filaments. We discuss the nature of the PWN and estimate the space velocity of the pulsar.

OBSERVATIONS AND DATA REDUCTION

Interferometric Observations on the 6-m Telescope

The core of CTB 80 was observed with the 6-m telescope as part of a program entitled "The Kinematics of Matter in Pulsar Wind Nebulae" (the main applicant is Yu.A. Shibanov). Our interferometric observations of CTB 80 were performed on October 9–10, 2001, at the prime focus of the 6-m telescope using the SCORPIO focal reducer; the equivalent focal ratio of the system was $F/2.9$. A description of SCORPIO is given in the paper by Afanasiev and Moiseev (2005) and on the Internet (http://www.sao.ru/hq/moisav/scorpio/scorpio.html); the SCOPRIO capabilities in interferometric observations have been described by Moiseev (2002). The seeing during the observations varied within the range 1.″2–2.″2. We used a scanning Fabry–Perot interferometer (FPI) in the 235th order at the wavelength of the Hα line; the separation between the neighboring orders of interference, $\Delta\lambda = 28$ Å, corresponded to a region free from order overlapping of 1270 km s^{-1} on the radial velocity scale. The width of the instrumental FPI profile was $FWHM \approx 2.5$ Å or $\simeq$110–120 km s^{-1}. Premonochromatization was performed using an interference filter with a half-width of $\Delta\lambda = 14$ Å centered on the Hα line. The detector was a TK1024 1024×1024-pixel CCD array. The observations were carried out with 2×2-pixel binning to reduce the readout time. In each spectral channel, we obtained 512×512-pixel images; at a 0.55″/pixel scale, the total field of view was 4.′7. We obtained a total of 32 interferograms at various FPI plate spacings, so the width of the spectral channel was $\delta\lambda = 0.87$ Å or 40 km s^{-1} near Hα. The exposure time was 240 s per channel.

We reduced the observations using software running in the IDL environment (Moiseev 2002). After the primary reduction (debiasing and flat fielding), the observational data were represented as $512 \times 512 \times 32$-pixel data cubes; here, a 32-channel spectrum corresponds to each pixel. Major difficulties in the data reduction process arose when night-sky emission lines were subtracted from interferograms. All bright image features were masked, and an azimuthally averaged radial sky emission line profile was constructed from the remaining areas; this profile was subtracted from the corresponding frame in the data cube. This technique allows the sky line intensity variations during two-hour observations to be effectively corrected. However, almost the entire field of view near the core of CTB 80 proved to be filled with weak emission features, which was also confirmed by our deep Hα images of the PWN. Therefore, the problem of choosing a sufficient number of "clean" sky areas in a region of almost 5′ in size arose. As a result, the weakest features in the field of view could be oversubtracted, and the Hα emission line profile is severely distorted at these locations. Our estimates indicate that the line distortion due to the background subtraction may be disregarded for regions in which the intensity of the $H\alpha$ line exceeds 150 photoelectrons per CCD pixel, which corresponds to a surface brightness of 8.6×10^{-17} erg s^{-1} cm^{-2} (uncorrected for the interstellar reddening).

The large number of background stars in the field allowed us to measure and correct the atmospheric transparency and seeing variations in each image. The resulting seeing was 2.″2. Subsequently, we reduced the spectra in the data cube to the same wavelength scale. The formal accuracy of measuring the relative radial velocities was about 2–4 km s^{-1}. However, since the emission lines in the object often have asymmetric profiles, the actual measurement accuracy depends on the chosen line profile fitting method.

The spectra of the object were smoothed with a $FWHM = 1.7$ Å (two channels) Gaussian for optimal filtering of the data cube. To reliably identify weak

Details of the narrow- and medium-band observations of the CTB 80 core with the 6-m (BTA) telescope and HST

Range	Filter	$\lambda_{\rm cen}$, Å	$FWHM$, Å	Exposure time, s
Hα BTA	FN657	6578	75	4×300
Continuum BTA	SED707	7036	207	4×120
Hα HST	F656N	6563	20	$2600 + 2700$
Continuum HST	F547M	5479	200	$1300 + 1300$
[O III] HST	F502N	5013	20	$2700 + 2700$
[S II] HST	F673N	6732	20	$2700 + 2700$

emission features, we also smoothed the images in the cube with a bivariate Gaussian. The resulting angular resolution was about $2''\!.6$. The smoothing was performed using the ADHOC software package.[1]

The continuum level in each spectrum was determined as a median mean of the eight weakest levels. When constructing the velocity field and the monochromatic image in the Hα line, we fitted the spectral line profile by a Gaussian using only the points offset by ± 3 channels from the predetermined line peak.

We calibrated the monochromatic image in energy units (erg $\rm s^{-1}$ $\rm cm^{-2}$) by comparison with our calibrated narrow-band image (see below).

All of the radial velocities in this paper are heliocentric; the passage to the Local Standard of Rest corresponds to $V_{\rm Hel} = V_{\rm LSR} + 17.6$ km $\rm s^{-1}$.

Medium- and Narrow-Band Images

Observations with the 6-m telescope. Our medium- and narrow-band observations of the CTB 80 core were performed on October 11 and 12, 2001, with the 6-m telescope using the SCORPIO focal reducer (see above) with seeing of $1''\!.4$–$1''\!.6$ at zenith distance $z = 12°$–$21°$. Filter parameters and exposure times are given in the table. The detector was a TK1024 1024×1024-pixel CCD array.

To calibrate the images, we observed the spectrophotometric standards G138–31 and Feige 110.

The HST archive. The PWN in CTB 80 was observed with HST (the main applicant is J. Trauger) in October 1997 using the WFPC2 instrument. Parameters of the filters used and the total exposure time are given in the table. The primary data reduction is automatically performed when the data are queried from the HST archive. A filtering code proposed by N.A. Tikhonov (in a private communication) was used to remove numerous cosmic-ray particle hits. The formal accuracy of the astrometric referencing using WCSTools is an order of magnitude lower than the internal accuracy of the USNO-A2.0 star catalog used as a reference one. The resultant value was taken to be $0''\!.3$.

RESULTS OF OBSERVATIONS

The PWN Morphology

Previous studies of the CTB 80 core showed that its optical emission is typical of SNRs: an intense (relative to Hα) [N II], [S II], [O I], [O III] line emission and a filamentary structure (see Angerhofer *et al.* 1980; Blair *et al.* 1984; Whitehead *et al.* 1989; Hester and Kulkarni 1988, 1989; and references therein). Significant differences in PWN morphology in different lines were reported: only a symmetric central shell is observed in the [O III] line, a shell to the east of it appears in the [S II] line, and two bright shells to the east and the west of the central structure that form an elongated core structure are observed in the Hα line.

The deep HST images of the PWN demonstrate a staggering filamentary, irregularly shaped multishell structure and confirm the results of ground-based observations (see Figs. 1a–1c, which show the [O III], [S II], and Hα images, respectively, with superimposed VLA 1.5-GHz radio isophotes).

Only the central horseshoe-shaped part of the core closest to the pulsar is seen in the [O III] line. The PWN morphology in the [O III] line clearly shows a structure expected for the bow shock produced by the pulsar's motion (see the discussion). The Hα emission is also observed in this central filamentary horseshoe-shaped shell; the Hα filaments are adjacent to the [O III] filaments from the outside. We clearly see the two bright (in Hα) filamentary shells in the east and the west, which form a spindle-shaped core structure in the east–west direction. The PWN sizes in the Hα line are about $75'' \times 38''$ or 0.73×0.37 pc.

---

[1] The ADHOC software package was developed by J. Boulestex (Marseilles Observatory) and is freely accessible on the Internet.

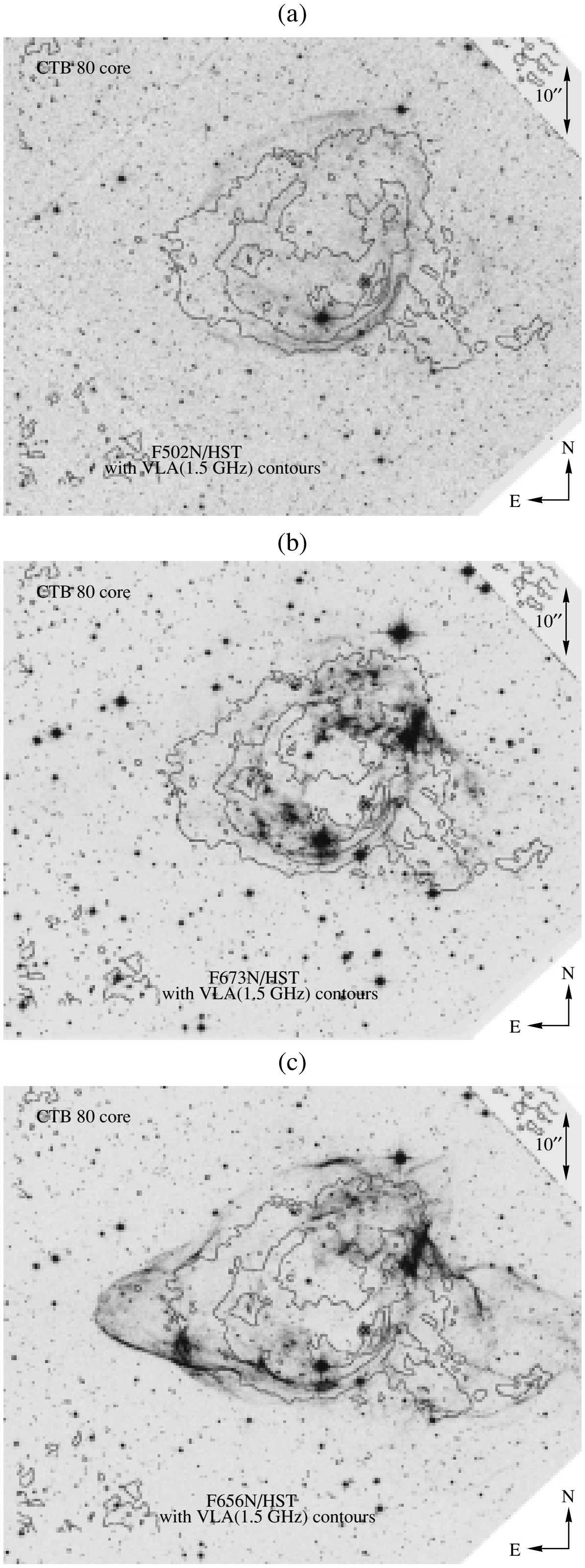

Fig. 1. HST images of the PWN with superimposed VLA 1.5-GHz radio isophotes: (a) in the [O III] line, (b) in the [S II] line, and (c) in the Hα line. The arrow in the bottom panel indicates the motion of the pulsar over a period of 1000 yr, as measured by Migliazzo *et al.* (2002).

The PWN Kinematics

The velocities of PWN filaments. The comparisons of relative line intensities in the core spectrum with diagnostic models made by several authors are suggestive of collisional excitation of the gas behind the front of a shock propagating at a velocity of about 120–140 km s^{-1} in a medium with a density of 25–100 cm^{-3} (Hester and Kulkarni 1989, and references therein). Gas motions in the PWN with such velocities have already been detected. The main method used was long-slit spectroscopy, which allowed the velocities of the individual, generally brightest (and, hence, possibly slowest) knots and filaments to be estimated (Angerhofer *et al.* 1981; Blair *et al.* 1984). Spectroscopic methods revealed no radial velocities higher than 200 km s^{-1} at Hα surface brightness $\geq 0.5 \times 10^{-6}$ erg cm^{-2} s^{-1} sr^{-1} anywhere in the PWN (Blair *et al.* 1988). Using the echelle spectrograph of the 4-m WHT telescope, Whitehead *et al.* (1989) found an expansion of the two central shells with velocities of 200 and 100 km s^{-1}.

Using FPI, we studied the PWN kinematics for the first time. The advantage of FPI observations is that they give the line profile everywhere in the PWN, and not only in the region cut out by the spectrograph slit.

Our observations indicate that the line profile, which is single in bright peripheral filaments, is characterized by a multicomponent structure or line asymmetry, bright red wings in the central PWN regions. As an illustration, Fig. 2 shows several profiles and their decomposition into individual Gaussians. Having analyzed all of the observed Hα profiles, we were able to localize the high-velocity gas in the PWN image that emits in the range from 200 to 400 km s^{-1} (shown at the center in Fig. 2).

Figure 3 shows several so-called position–velocity diagrams (the change in gas velocity along the chosen direction) constructed from our FPI observations and the localization of the corresponding directions in the PWN image.

As we see from this figure, the position–velocity diagrams in the bright core structures show velocities that agree with the previously measured expansion velocity of 100–200 km s^{-1}; i.e., they completely confirm the results of spectroscopic observations.

In addition to the gas velocities in bright filaments within the range from −200 to +200 km s^{-1}, our observations clearly reveal weaker high-velocity Hα emission features in the PWN. Weak emission at high velocities is clearly seen in the position–velocity diagrams up to 400–450 km s^{-1}. This is a lower limit, since the velocity range is limited by the FPI velocity

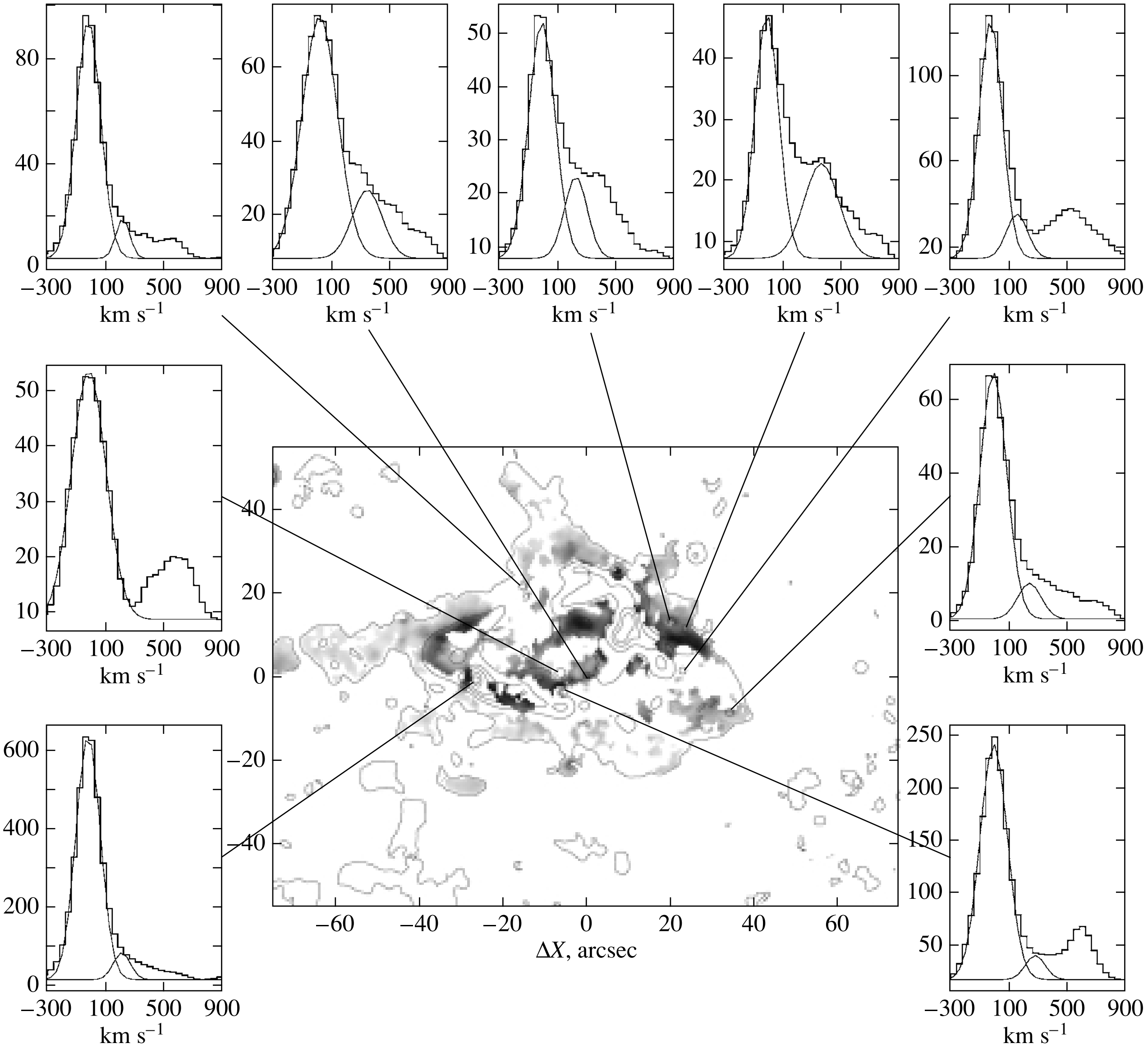

Fig. 2. Hα profiles at several points of the PWN and their Gaussian decomposition. The features at a velocity of +605 km s^{-1} are attributable to the [N II] 6548 Å line emission that falls in the wings of the interference filter and is separated from the Hα emission by about 0.5 order of interference. The localization of the high-velocity gas emitting in the range from 200 to 400 km s^{-1} is shown in the central Hα image of the PWN (isophotes).

range free from order overlapping and the impossibility to properly take into account the contribution from the [N II] 6548 Å line emission.

Figure 3 (scan *3*) clearly shows the typical (for an expanding shell) structure of the so-called velocity ellipsoid (its half corresponding to positive velocities) that is determined by high-velocity motions. The corresponding possible expansion velocity reaches the lower limit mentioned above.

The surface brightness of the detected high-velocity component of the Hα line in the central part of the core lies within the range (1.4–20) × 10^{-16} erg s^{-1} cm^{-2} arcsec^{-2}. In our estimation, we took the color excess $E(B-V) = 0.8$ from Blair *et al.* (1984).

Figure 4 shows the radial velocity field corresponding to the peak of the main line component constructed from our observations and superimposed on the Hα image of the PWN. We emphasize that the radial velocity field refers only to the core of the line, which often has a complex multicomponent profile. The velocities determined from the line peak lie within the range −100 to +50 km s^{-1}, in agreement with the spectroscopic observations.

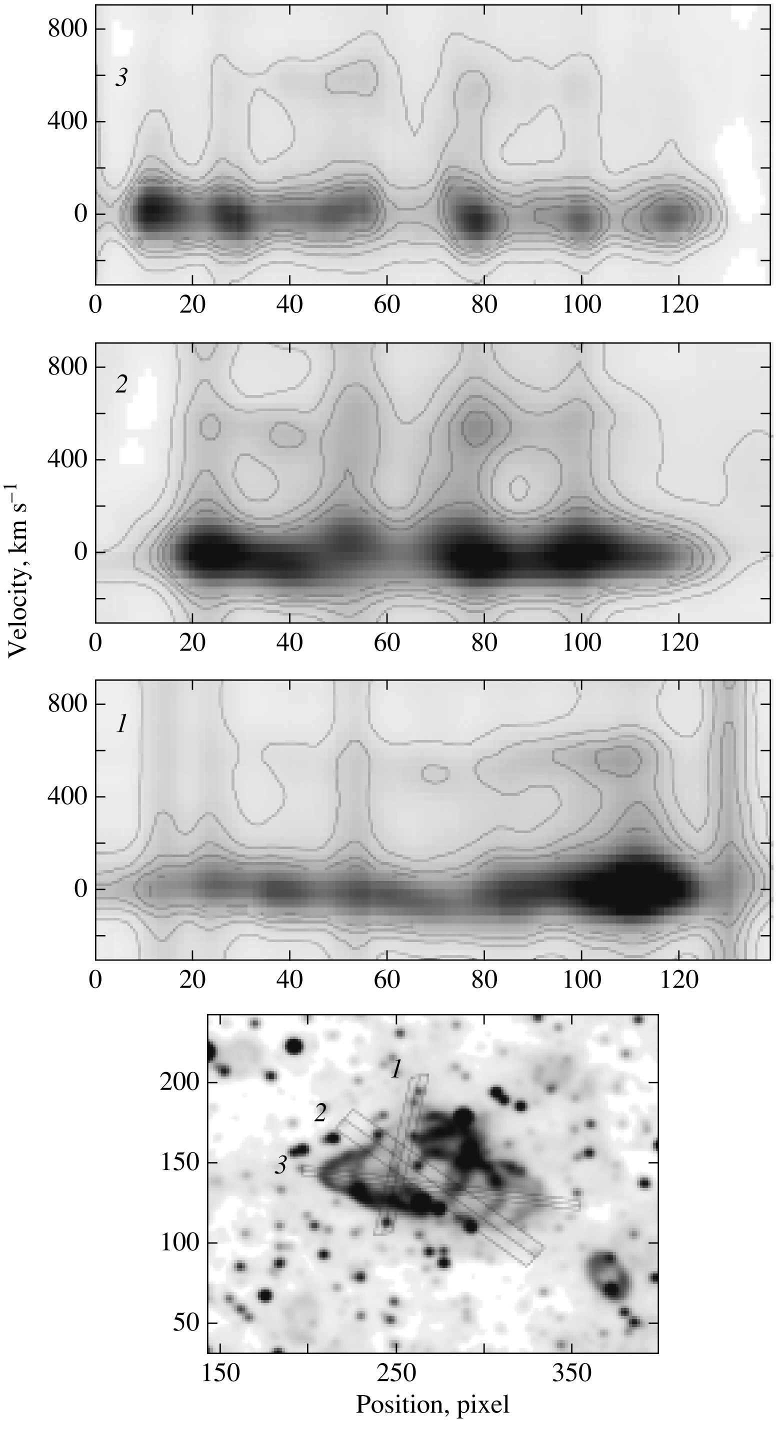

Fig. 3. Position–velocity diagrams constructed from our FPI observations and the localization of the corresponding scans in the PWN image. The emission features at a velocity of about 600 km s^{-1} are attributable to the [N II] 6548 Å line.

In Figs. 4a and 4b, we clearly see the symmetry axis in the velocity distribution of the peak of the main line component in a direction $P \approx 230°$ close to but not coincident with the direction of the pulsar's motion ($P = 252° \pm 7°$; Migliazzo *et al.* 2002).

We estimated the total flux from the PWN in the main line component to be 8.4×10^{-12} erg s^{-1} cm^{-2}, in close agreement with the estimate by Whitehead *et al.* (1989). The total flux in the high-velocity line component is 6.4×10^{-13} erg s^{-1} cm^{-2}; the luminosity of the high-velocity gas accounts for about 7% of the total luminosity of the core in the Hα line.

The high-velocity emission detected in the core for the first time has confirmed the changes in the PWN fine structure pointed out by Strom and Blair (1985)—possibly the proper motions of the filaments of the central shell corresponding to a velocity of 250d km s^{-1} (up to 400d km s^{-1}), where d is the distance to CTB 80 in kpc, i.e., about 500 km s^{-1} (possibly up to 800 km s^{-1}).

The velocities of filaments in the CTB 80 shell outside the core. The optical radiation from the extended SNR CTB 80 outside the PWN is represented by the system of faint filaments clearly seen in the [S II] and Hα lines over the entire $16' \times 16'$ field whose image is given in the paper by Hester and Kulkarni (1989).

The filamentary morphology and the intense [S II] line emission provide strong evidence for the gas emission behind the shock front. It is interesting to measure the velocities of these filaments in the extended remnant outside the core, since, in general, the thin filaments can be localized on the front or rear side of the old shell; i.e., these may be projected rather than be physically associated with the PWN. In addition, the pulsar's velocity with respect to the ambient gas is important in estimating the expected shape of the bow shock produced by the wind from a fast-moving pulsar. Figure 4b shows only the brightest outer filaments in a $4' \times 4'$ field for which the background subtraction effect is insignificant (see above). The Hα brightness of these filaments exceeds 8.6×10^{-17} erg s^{-1} cm^{-2}. As follows from Fig. 4b, the velocities of the bright filaments in the outer shell of CTB 80 do not differ significantly from the velocities of the peripheral filaments of the PWN undistorted by the expansion of the latter.

Note, in particular, the filaments that are immediately adjacent to the PWN in the north and the east and that form a kind of a wake at the boundary of the shell produced by the wind from a moving pulsar. (These filaments are most distinct in the [S II] lines in Fig. 2b from Hester and Kulkarni 1989.) As our measurements indicate, the velocities of these filaments do not differ significantly from those of the bright PWN filaments either.

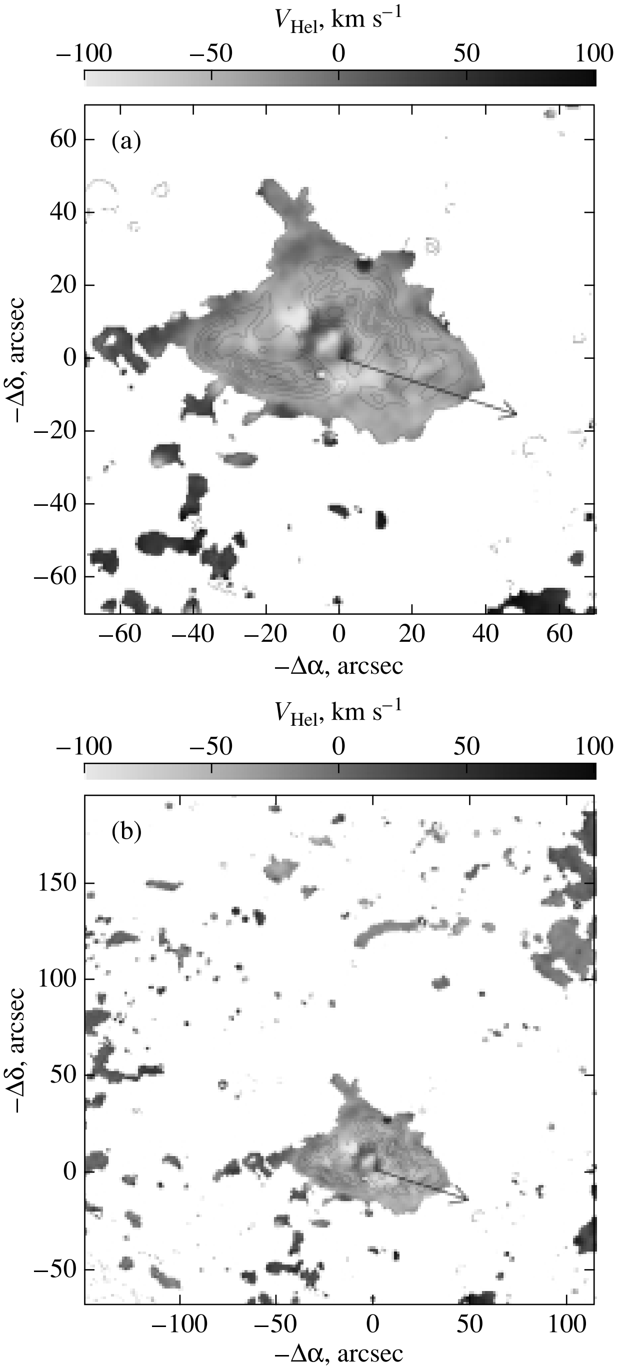

Fig. 4. (a) PWN: the velocity field of the Hα peak superimposed on the PWN image. The arrow indicates the direction of the pulsar's motion, as measured by Migliazzo *et al.* (2002); (b) the same for the entire field of view about 5′ in size in the image obtained with the 6-m telescope (only the brightest outer filaments are shown).

DISCUSSION

The difficulty of explaining the nature of the PWN in CTB 80 lies in the fact the bow-shock structure (in the [O III] line, the radio continuum, and the soft X-ray band) and the elongated filamentary shell-like structure in the Hα line (which is definitely also of a shock origin that, in the opinion of Hester (2000), is associated with the action of the pulsar's jets) are simultaneously clearly seen around the pulsar. We do not see any manifestations of the interaction between two processes: the ejections of relativistic pulsar plasma in two jets and the motion of the pulsar. The elongated PWN structure is not distorted by the pulsar's motion in any way; the bow shock, in turn, is not distorted by the action of the two plasma jets in any way either. The rough estimates given below indicate that, individually, both structures can be explained adequately.

Estimates for the Shock Waves Produced by the Pulsar's Jets

If the pulsar's power L is constant over time t and is released in a solid angle Ω, blowing a bubble of radius $R = R(t)$ in a homogeneous interstellar medium with a density ρ_0, then the mass $M \sim \Omega\rho_0 R^3/3$ is swept up from the bubble. Assuming that all of this mass is gathered in a thin layer at radius R and remains in the same solid angle Ω (in fact, it will partially flow around the jet) and equating the pulsar-wind momentum flux L/c to the rate of increase in the momentum of the wind-driven shell,

$$\frac{L}{c} = \frac{d}{dt}(Mv),$$

where $v = dR/dt$, we obtain an acceptable size of the bubble swept up by the wind for a pulsar at rest under reasonable assumptions about the ambient density and the wind asphericity. Assuming that $R \propto t^\alpha$, we have

$$\frac{L}{c} = \frac{\Omega}{3}\rho_0\alpha\frac{d}{dt}\left(\frac{R^4}{t}\right);$$

hence, $\alpha = 1/2$ at $L = \text{const}$, i.e.,

$$R = \left(\frac{6L}{\Omega c\rho_0}\right)^{1/4} t^{1/2} \sim 3\ \text{pc} \times \left(\ell L_{36}\frac{4\pi}{\Omega n_0}\right)^{1/4} t_6^{1/2}, \tag{1}$$

where $\ell = L/L_0$ is the fraction of the power L_0 went into the solid angle Ω and spent on blowing the bubble, n_0 is the particle number density (for hydrogen composition), and t_6 is the time in Myr.

The power of the flux in relativistic particles (including all types of photons) from the pulsar PSR B1951+32 is $L_0 = \dot{E}_{\text{rot}} = 3.7 \times 10^{36}$ erg s^{-1} (Kulkarni *et al.* 1988). At $n_0 = 1$ cm^{-3} , $L_{36} = 3.7$, and the pulsar's total age $t_6 = 0.1$, we obtain a bubble size of about 1 pc at $\ell = 1$ even for isotropic radiation ($\Omega = 4\pi$), in agreement with the observed PWN size in the Hα line. In fact, only a small fraction ℓ of the pulsar's power goes into blowing the bubble, but Ω is also much less than 4π (by several hundred times for a linear jet opening angle of several degrees).

We emphasize that this is the minimum upper limit: here, the shock waves are assumed to be radiative. The bubble size will increase if the hot-gas pressure inside the bubble is taken into account (Casteleti *et al.* 2003). Two cases are possible: the radius for radiative shock waves is larger than our estimate, but smaller than that for adiabatic shock waves (McKee and Ostriker 1977; Blinnikov *et al.* 1982).

If we took into account the hot-gas pressure inside the bubble and for adiabatic shock waves, we would obtain the maximum estimate at $\Omega = 4\pi$ (Avedisova 1971; Weaver *et al.* 1977; Ostriker and McKee 1988):

$$R = 28\ \text{pc} \times n_0^{-1/5} L_{36}^{1/5} t_6^{3/5}. \tag{2}$$

Hence, R could be even an order of magnitude larger than that from (1).

Let us make several remarks suggesting that these rough estimates are uncertain. On the one hand, the Balmer line emission in PWNs is evidence of nonradiative shock waves in a partially neutral medium (Chevalier and Raymond 1980); it is produced by electron impact excitation or ion charge exchange. In this case, neutral hydrogen can penetrate into the hot gas and impart odd shapes to the shock waves (Bucciantini and Bandiera 2001; Bucciantini 2002; D'Amico *et al.* 2003)

On the other hand, formula (2) was derived for a hot wind with a normal (Pascal) pressure. Since the flow of magnetized particles of photons in a pulsar wind is directed only along the radius, a simple formula of form (1) the derivation of which assumes no pressure isotropy holds good, while formula (2) overestimates the result. Many problems associated with the composition of this wind have not yet been solved (the so-called sigma paradox—the transition from the fraction of the electromagnetic pressure expressed in terms of the Poynting vector to the kinetic pressure of the particle flux cannot be reliably calculated (see the review by D'Amico *et al.* 2003)).

A time shorter than the pulsar's age should be taken as t_6, since it has flown into the dense layers of the shell of the old SNR relatively recently. Castelleti *et al.* (2003) took $t = 18\,200$ yr as the PWN age at an ambient density of $n_0 = 0.5$ cm^{-3}. According to Mavromatakis *et al.* (2001), the relative line intensities in the spectrum of the filaments of the extended CTB 80 shell are typical of the gas radiation behind the front of a shock propagating at a velocity of 85–120 km s^{-1} in a medium with an initial density of about 2–5 cm^{-3}. This density is equal to the mean density in the H I shell estimated by Koo *et al.* (1990).

However, the dependence of R on all parameters, including the density and the age, is weak; i.e., a small fraction ℓ of the total power that goes into blowing the bubble will clearly suffice. (We also see the pulsar's emission; i.e., clearly, the fraction of the captured power, ℓ, is appreciably smaller than unity.)

Thus, the sizes of the bubbles swept up by the pulsar-wind jets can easily be made close to the observed values even if the density is much higher and the fraction ℓ of the pulsar's power that goes into the jet is small.

An Estimate for the Location of the Bow Shock

The pulsar's motion in the plane of the sky with a velocity of $v_0 = 240$ km s^{-1} (Migliazzo *et al.* 2002) for an *isotropic* wind must give rise to a bow shock, which is observed in several pulsars (see the review by D'Amico *et al.* 2003). To estimate the shock shape, we can use the solutions by Lipunov and Prokhorov (1984) and Wilkin (1996). The latter obtained an analytical solution for a normal (nonrelativistic) stellar wind with radiative shock waves:

$$R(\theta) = d_0 \operatorname{cosec} [3(1 - \theta \cot \theta)]^{1/2}, \qquad (3)$$

where d_0 is the distance from the pulsar to the head point at contact discontinuity. This solution describes well the classical numerical results by Baranov *et al.* (1971) and van der Swaluw *et al.* (2003) (see Fig. 8 in the latter paper). An approximate solution for adiabatic shock waves was given by Chen *et al.* (1996). The criticism of the applicability of such solutions to known PWNs (see Bucciantini and Bandiera 2001) is based on these not including the effects of charge exchange and neutral hydrogen penetration behind the shock mentioned above. However, the PWN in CTB 80 is unique in that the bow shock is observed not only in Balmer lines, but also most clearly in the [O III] lines and in the X-ray and radio bands, i.e., in a hot, ionized plasma. Therefore, simple analytical solutions may well be valid in this case.

We obtain the following estimate from the balance between the momentum fluxes $\ell_1 L/c$ and $4\pi d_0^2 \rho_0 v_0^2$:

$$d_0 = \left(\frac{\ell_1 L}{4\pi c \rho_0 v_0^2} \right)^{1/2}. \qquad (4)$$

Hence, we find for $v_0 = 240$ km s^{-1}, $\rho_0 = 2 \times 10^{-24}$ g cm^{-3} ($n_0 = 1$ cm^{-3}), and $\ell_1 = 1$ that $d_0 \approx 0.044$ pc. This value is comparable to the observed distance from the pulsar to the [O III] filaments that determine the position of the head point at the shock front, $d_{\text{obs}} \sim 6'' \approx 0.057$ pc.

The theoretical value of d_0 will be close to d_{obs} if we take into account the fact that $v_0 = 170$ km s^{-1} should be substituted for $v_0 = 240$ km s^{-1}, since the pulsar moves in the matter of a remnant expanding with a velocity of 72 km s^{-1}. In this case, $d_0 \approx 0.043$ pc.

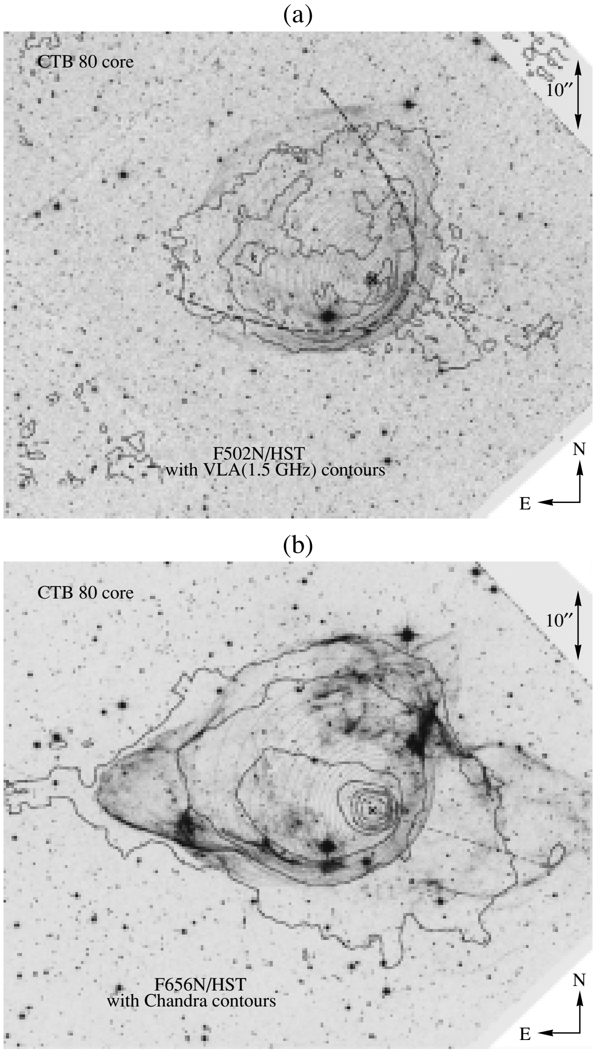

Fig. 5. (a) PWN in the [O III] line and in the radio continuum (isophotes): the bow shock corresponding to solution (3) for the pulsar's motion in the plane of the sky with a position angle of 235° (dashed line) and the bow shock inclined at an angle of 60° to the plane of the sky (θ isolines). (b) The same bow shock inclined at an angle of 60° chosen by the best agreement with the [O III] line image superimposed onto the Hα and X-ray image (isophotes) of the PWN. The arrow indicates the pulsar's motion over a period of 1000 yr, as measured by Migliazzo *et al.* (2002)

In Fig. 5a, the solution by Wilkin (1996) is superimposed on the PWN image in the [O III] line and in the radio continuum. The distance from the head point at the front to the pulsar is assumed to be $d_0 \approx 0.043$ pc, and the axis of the surface with a position of angle at $P = 235°$ does not coincide with the pulsar's velocity direction in the plane of the sky. According to the measurements by Migliazzo *et al.* (2002), an azimuthal asymmetry in the projection of the theoretical surface relative to the observed shape of the central shell remains noticeable at a position angle of $P = 252°$.

The fact that the shape of the bow shock observed in the [O III] line is appreciably "broader" than the gas-dynamical solutions by Wilkin (1996) may suggest that the pulsar moves at a significant angle to the plane of the sky. Allowing for the possible inclination of the pulsar's velocity vector to the plane of the sky yields better agreement of the theory with the observed morphology of the central shell. By varying the pulsar's velocity vector, we found the best agreement with the observations for a bow shock whose axis is inclined at an angle of 60° to the plane of the sky. Figure 5a shows this solution for the bow shock chosen by the best agreement with the shape of the central shell observed in the [O III] line and in the radio continuum. As we see, the shape of the projection of the theoretical surface defined by relation (3) can be completely reconciled with the observed PWN morphology. In this case, the position angle of the pulsar's velocity vector in the plane of the sky is $P = 235°$; i.e., it is close to the direction of the symmetry axis in the velocity field of the main Hα line component found above. $P = 235°$ matches the value obtained by Strom (1987).

We emphasize that, if the pulsar's velocity vector is inclined at an angle of 60°, its space velocity is twice as high as its velocity measured in the plane of the sky; i.e., it reaches 500 km s^{-1} (this value agrees with the mean value in the velocity distribution of pulsars; see Arzoumanian *et al.* 2002). Since the distance d_0 at a higher velocity is a factor of $\sqrt{2}$ smaller, for close agreement with the observations, we must take a slightly lower gas density in front of the bow shock.

Our kinematic studies are also consistent with the suggested model. Since the thickness of the postshock emitting gas, which is determined by the apparent thickness of the bright peripheral PWN filaments, is an order of magnitude smaller than the distance the pulsar traverses in 1000 yr, (see Fig. 1), we conclude that the radiative cooling time of the postshock gas is short, about 100 yr. In this time, an element of gas is not only compressed, but also acquires a velocity that corresponds to the pulsar's motion. Without detailed calculations, it is hard to tell at which velocity the gas emission is at a maximum; one may only expect the observed velocity to be a significant fraction of the pulsar's velocity.

Gas motions with such velocities in the PWN were detected for the first time in our work (see above). These velocities refer to the weak emission feature in the Hα line; these are observed both in the central region around the pulsar, and near the bright filaments at the PWN boundary (see Fig. 2). The radial velocities of the bright filaments are within the ± 200 km s^{-1} range. This is an ordinary (for SNRs) situation related to the bright filaments usually representing the front surfaces seen edge-on.

Unfortunately, since the velocity measurement range in our FPI observations is limited, at present, we cannot unambiguously determine whether the pulsar moves toward or away from us. The existence of high positive velocities argues for the motion away from us, but as yet we have no information about the possible negative velocities without further FPI observations. The derived velocity distribution of the line peak could clarify the picture, but here we are restricted by the density distribution in the closest neighborhood of the shell corresponding to the bow shock being unknown. In particular, the asymmetric expansion of the central shell (according to Whitehead *et al.* (1989), the motion of the approaching side at a velocity of about -200 km s^{-1} is most clearly observed in it) could be attributable to the higher brightness of this side due to a nonuniform ambient gas density.

In Fig. 5b, the same theoretical surface of the bow shock that is inclined at an angle of 60° to the plane of the sky and that agrees best with the PWN emission in the [O III] line is superimposed on the Hα image with X-ray isophotes. The two shell-like Hα structures in the west and the east are far outside the bow shock. These structures, which form the elongated PWN shape, were explained by the action of the pulsar's jets (Hester 2000).

It should be noted that, if the pulsar's jets are directed at an angle to its space velocity (e.g., lie in the plane of the sky), then the contradiction with the absence of an apparent influence of the jets on the shock front in its brightest parts mentioned at the beginning of the section is removed.

Of course, the representation of the shock as an infinitely thin layer with shape (3) is oversimplified. More detailed solutions should be used, and the structure of two shocks with a contact discontinuity between them should be taken into account (Baranov *et al.* 1976), since there is a hint at such a structure in the observations. In particular, Moon *et al.* (2004) associate the structure observed in X rays with a backward shock wave in the pulsar wind and in the Hα line with a bow shock in the ambient medium.

Note also that ℓ_1 in formula (4) may in fact be the fraction of the pulsar's emission absorbed by an ionized plasma, while ℓ in formula (1) for the jet may be the fraction of the emission absorbed by neutral hydrogen. For example, hard ultraviolet emission must be absorbed completely by neutral hydrogen and only partially by ionized plasma. Another possible process, the proton-beam charge exchange in a neutral gas, cannot take place in an ionized medium. Thus, different components of the pulsar's flux can manifest themselves differently in different components of the ambient medium.

A different interpretation of the elongated PWN shape in the Hα line is also possible. The system of thin filaments mentioned in the section Results of Observations, which characterizes the optical emission from the extended remnant outside the PWN, is

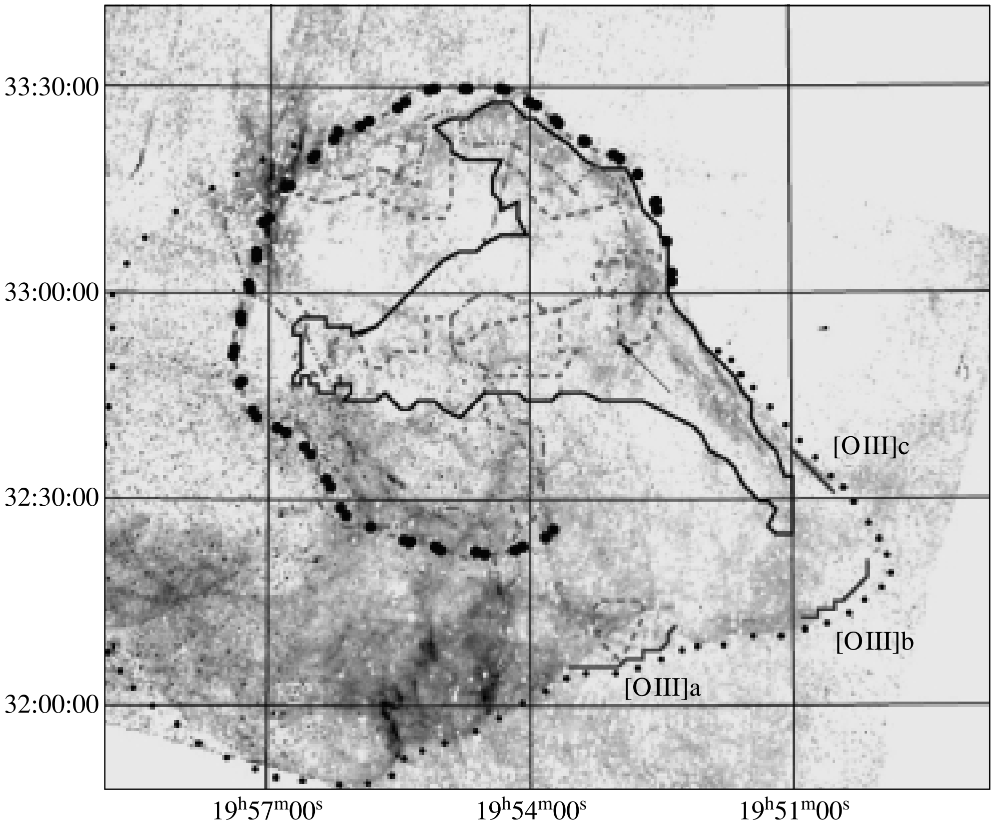

Fig. 6. General scheme of CTB 80 from Mavromatakis *et al.* (2001): the [S II] image of the region, radio ridges (solid line), and the infrared and HI shells (the dashed and dash–dotted lines, respectively). The large and small circles indicate the suggested model for the shell of the old SNR composed of two hemispheres in projection onto the plane of the sky.

most likely the layered structure of the old CTB 80 shell (Hester and Kulkarni 1989). Our velocity measurements for the brightest filaments suggest that these are not projected, but are physically associated with the PWN.

The thickness of the layers (typically, $\sim 10''$–$20''$ or 0.1–0.2 pc) and the separation between them (about $2'$–$2.5'$ or 1–1.5 pc) at the pulsar's velocity of 240 km s^{-1} in the plane of the sky yield a time of about 5000 yr between the passages of neighboring layers and a passage time of a dense layer of 400–800 yr.

The pulsar's motion through such a layered medium can produce the observed elongated multishell structure of the core as a result of the pulsar-wind breakthrough from a dense layer into a tenuous medium between the layers. The breakthrough of the nonrelativistic wind of Wolf–Rayet stars from a dense cloud into a tenuous intercloud gas leads precisely to this effect (see, e.g., Dopita and Lozinskaya 1990).

Localization of the Pulsar in the Extended Remnant CTB 80

If the space velocity of the pulsar actually reaches 500 km s^{-1}, then, in general, it traverses a distance of 50 pc in a time of 10^5 yr and could go beyond the symmetric infrared and H I shells about 40 pc in size, which, according to the previous interpretation, determined the total volume of the old remnant CTB 80. However, the deep images taken in the Hα+[N II], [S II], [O II], [O III] lines by Mavromatakis *et al.* (2001) revealed large-scale filamentary and diffuse structures in the nearby 2° × 2° region. These optical filaments in the north and the northwest closely correlate with the radio images of the remnant (Castelleti *et al.* 2003) and with the boundary of the infrared shell, but go far beyond the infrared and H I shells in the south and the east. (Here, we disregard the extended filaments in the east associated not with CTB 80, but with the remnant of a different supernova (Mavromatakis and Strom 2002).) The relative line intensities in the spectrum of these large-scale filaments are typical of the radiative cooling of the gas behind the front of a shock propagating at a velocity of 85–120 km s^{-1} in a medium with an initial density of about 2–5 cm^{-3} (Mavromatakis *et al.* 2001). Such a density agrees with the mean density in the H I shell estimated by Koo *et al.* (1990) from 21-cm line observations. This argues for the association of the large-scale filaments with the SNR CTB 80.

Therefore, a more complex spatial structure composed of two hemispheres with different sizes should probably be considered as the SNR CTB 80. One hemisphere, which is determined by the northeastern radio ridge and the infrared and H I shells, is the result of the interaction of the shock triggered by a supernova explosion with a dense medium. The second part of the shell has an aspherical shape and is determined by the southwestern ridge and the [O III] filaments denoted by III and IV as well as by the system of bright filaments to the east of IV (see Fig. 2 from Mavromatakis *et al.* 2001). This part of the shell was most likely formed by the shock in a medium with a much lower density.

Figure 6 shows the approximate boundaries of the two parts of the shell in projection onto the plane of the sky in this model.

Note that ROSAT observations revealed a conical ~1° region of thermal X-ray emission southeast of the pulsar far beyond the infrared shell (Safi-Harb *et al.* 1995). The central region of the second part of the shell mentioned above could, in principle, be responsible for this emission. However, the SNR CTB 80 is observed along the Cygnus spiral arm and is immediately adjacent to the giant superbubble produced by intense stellar wind from the Cyg OB2 cluster (Lozinskaya *et al.* 2002, and references therein). Therefore, in general, the thermal X-ray emission in the extended conical region could be the background emission, i.e., it could belong not to CTB 80, but to the superbubble.

In the proposed scheme, the morphology of the SNR in the plane of the sky suggests that the major axis of this structure composed of two hemispheres with different sizes is oriented at a large angle to the plane of the sky. Therefore, at a possible space velocity of 500 km s^{-1}, the pulsar has not yet gone outside the shell of the extended remnant CTB 80.

CONCLUSIONS

Our kinematic study of the pulsar wind nebula in the old supernova remnant CTB 80 using the FPI of the 6-m SAO telescope revealed weak high-velocity Hα features in the PWN at least up to a velocity of 400–450 km s^{-1}. We confirmed the previously measured expansion of the system of bright filaments with a velocity of 100–200 km s^{-1}. We analyzed the PWN morphology in the Hα, [S II], and [O III] lines using HST archival data. The shape of the bow shock, determined by the central horseshoe-shaped shell bright in the [O III] line and in the radio continuum, was shown to be in best agreement with the theory for a significant (about 60°) inclination of the pulsar's velocity vector to the plane of the sky. The space velocity of the pulsar is twice as high as its tangential velocity measured by Migliazzo *et al.* (2002); i.e., it reaches 500 km s^{-1}. This pattern of motion is also confirmed by the high radial velocities of the gas in the PWN that we found here. Thus, PSR B1951+32 is the first pulsar whose possible radical velocity (about 400 km s^{-1}) has been estimated from the PWN morphology and kinematics.

The filamentary shell-like structures observed in the Hα line in the east and the west outside the bow shock can be explained not only by the action of the pulsar's jets, but also by the pulsar-wind breakthrough into an inhomogeneous ambient medium.

We considered the general scheme of CTB 80 that includes the most recent optical and radio observational data in which the pulsar's high space velocity is consistent with its location in the dense shell of the old SNR.

Of course, the proposed scheme of the PWN in CTB 80 must be additionally confirmed. The existence of high velocities in the PWN, the pattern of elongated Hα structures (possibly under the influence of the pulsar's jets or when the wind breaks through from a thin dense layer) and other questions require further observations and detailed hydrodynamic simulations of this interesting object. An analysis of the velocity field for the extended filaments in the entire region can give a kinematic confirmation for the proposed scheme of the old SNR CTB 80.

ACKNOWLEDGMENTS

This work was supported by the Russian Foundation for Basic Research (project nos. 02-02-16500, 03-02-17423, 04-02-16042) and the Federal Science and Technology Program (contract no. 40.022.1.1.1103). A.V. Moiseev thanks the Foundation for Support of Russian Sciences for partial support of this work. We are grateful to Yu.A. Shibanov for a kind permission to use the data obtained as part of his observational program on the 6-m BTA telescope, B.M. Gaensler for providing the VLA radio data, and I.V. Karamyan, V.Yu. Avdeev, and O.V. Egorov for help. This work is based on the observational data obtained with the 6-m SAO telescope financed by the Ministry of Science of Russia (registration no. 01-43) and on the NASA/ESA Hubble Space Telescope data taken from the archive of the Space Telescope Science Institute operated by the Association of Universities for research in astronomy under a NASA contract (NAS 5-26555) and data from the Chandra X-ray Observatory Center operated by the Smithsonian Astrophysical Observatory for and on behalf of the NASA under contract NAS8-03060.

REFERENCES

1. V. L. Afanasiev and A. V. Moiseev, Pis'ma Astron. Zh. **31**, 214 (2005) [Astron. Lett. **31**, 194 (2005)].
2. P. E. Angerhofer, R. G. Strom, T. Velusami, and M. R. Kundu, Astron. Astrophys. **94**, 313 (1981).
3. P. E. Angerhofer, A. S. Wilson, and J. R. Mould, Astrophys. J. **236**, 143 (1980).
4. Z. Arzoumanian, D. F. Chernoff, and J. M. Cordes, Astrophys. J. **568**, 289 (2002).
5. V. S. Avedisova, Astron. Zh. **48**, 894 (1971) [Sov. Astron. **15**, 708 (1972)].
6. V. B. Baranov, K. V. Krasnobaev, and A. G. Kulikovskiĭ, Dokl. Akad. Nauk SSSR **194**, 41 (1971) [Sov. Phys. Dokl. **15**, 791 (1971)].
7. V. B. Baranov, K. V. Krasnobaev, and M. S. Ruderman, Astrophys. Space Sci. **41**, 481 (1976).
8. S. I. Blinnikov, V. S. Imshennik, and V. P. Utrobin, Pis'ma Astron. Zh. **8**, 671 (1982) [Sov. Astron. Lett. **8**, 361 (1982)].
9. W. P. Blair, R. A. Fesen, and R. H. Becker, Astron. J. **96**, 1011 (1988).
10. W. P. Blair, R. P. Kirshner, R. A. Fesen, *et al.*, Astrophys. J. **282**, 161 (1984).
11. N. Bucciantini, Astron. Astrophys. **387**, 1066 (2002a).
12. N. Bucciantini, Astron. Astrophys. **393**, 629 (2002b).
13. N. Bucciantini and R. Bandiera, Astron. Astrophys. **375**, 1032 (2001).
14. G. Castelleti, G. Dubner, K. Golap, *et al.*, Astron. J. **126**, 2114 (2003).
15. Y. Chen, R. Bandiera, and Z. Wang, Astrophys. J. **469**, 715 (1996).
16. R. A. Chevalier and J. C. Raymond, Astrophys. J. Lett. **225**, L27 (1978).
17. N. D'Amico, R. Bandiera, N. Bucciantini, *et al.*, Mem. Soc. Astron. Ital. **74**, 345 (2003).
18. M. A. Dopita and T. A. Lozinskaya, Astrophys. J. **359**, 419 (1990).
19. R. A. Fesen, J. M. Shull, and J. M. Saken, Nature **334**, 229 (1988).
20. A. S. Fruchter, J. H. Taylor, D. C. Backer, *et al.*, Nature **331**, 53 (1988).
21. J. J. Hester, *Proc. Conf. "Spin, Magnetism and Cooling of Young Neutron Stars," Kavli Institute of Theoretical Physics, 2000a*, http://online.itp.ucsb.edu/online/neustars_c00/hester/.
22. J. J. Hester, Bull. Am. Astron. Soc. **32**, 1542 (2000b).
23. J. J. Hester and S. R. Kulkarni, Astrophys. J. Lett. **331**, L121 (1988).
24. J. J. Hester and S. R. Kulkarni, Astrophys. J. **340**, 362 (1989).
25. B.-C. Koo, W. T. Reich, C. Heiles, *et al.*, Astrophys. J. **364**, 178 (1990).
26. B. C. Koo, M. S. Yun, P. T. P. Ho, and Y. Lee, Astrophys. J. **417**, 196 (1993).
27. S. R. Kulkarni, T. C. Clifton, D. C. Backer, *et al.*, Nature **331**, 50 (1988).
28. V. M. Lipunov and M. E. Prokhorov, Astrophys. Space Sci. **98**, 221 (1984).
29. T. A. Lozinskaya, V. V. Pravdikova, and A. V. Finogenov, Pis'ma Astron. Zh. **28**, 260 (2002) [Astron. Lett. **28**, 223 (2002)].
30. F. Mantovani, W. Reich, C. J. Salter, and P. Tomasi, Astron. Astrophys. **145**, 50 (1985).
31. F. Mavromatakis and R. G. Strom, Astron. Astrophys. **382**, 291 (2002).
32. F. Mavromatakis, J. Ventura, E. V. Paleologou, and J. Paramastorakis, Astron. Astrophys. **371**, 300 (2001).
33. C. F. McKee and J. P. Ostriker, Astrophys. J. **218**, 148 (1977).
34. J. M. Migliazzo, B. M. Gaensler, D. C. Backer, *et al.*, Astrophys. J. **567**, L141 (2002).
35. A. V. Moiseev, Bull. Spec. Astrophys. Obs. **54**, 74 (2002); astro-ph/0211104.
36. D.-S. Moon, J.-J. Lee, S. S. Eikenberry, *et al.*, Astrophys. J. Lett. **610**, L33 (2004).
37. J. P. Ostriker and C. F. McKee, Rev. Mod. Phys. **60**, 1 (1988).
38. S. Safi-Harb, H. Ogelman, and J. P. Finley, Astrophys. J. **439**, 722 (1995).
39. R. G. Strom, Astrophys. J. Lett. **319**, L103 (1987).
40. R. G. Strom, P. E. Angerhofer, and J. R. Dickel, Astron. Astrophys. **139**, 43 (1984).
41. R. G. Strom and W. P. Blair, Astron. Astrophys. **149**, 259 (1985).
42. R. G. Strom and B. W. Stappers, *Proc. Conf. "Pulsar Astronomy"* (2000).
43. E. van der Swaluw, A. Achlerberg, V. A. Gallant, *et al.*, Astron. Astrophys. **397**, 913 (2003).
44. T. Velusami and M. R. Kundu, Astron. Astrophys. **32**, 375 (1974).
45. T. Velusami, M. R. Kundu, and R. H. Becker, Astron. Astrophys. **51**, 21 (1976).
46. R. Weaver, R. McCray, J. Castor, *et al.*, Astrophys. J. **218**, 377 (1977).
47. M. J. Whitehead, J. Meaburn, and C. A. Claiton, Mon. Not. R. Astron. Soc. **237**, 1109 (1989).
48. F. P. Wilkin, Astrophys. J. Lett. **459**, L31 (1996).

Translated by V. Astakhov

Astronomy Letters, Vol. 31, No. 4, 2005, pp. 258–262. Translated from Pis'ma v Astronomicheskiĭ Zhurnal, Vol. 31, No. 4, 2005, pp. 284–289.
Original Russian Text Copyright © 2005 by Shtykovskiy, Lutovinov, Gilfanov, Sunyaev.

Constraints on the Luminosity of the Central Source in SNR 1987A

P. E. Shtykovskiy[1,2*], A. A. Lutovinov[1,2], M. R. Gilfanov[2,1], and R. A. Sunyaev[1,2]

[1] *Space Research Institute, Russian Academy of Sciences, Profsoyuznaya ul. 84/32, 117997 Moscow, Russia*
[2] *Max Planck Institut für Astrophysik, Karl Schwarzschild Str. 1, D-85740 Garching bei München, Germany*

Received November 18, 2004

Abstract—We obtained constraints on the luminosity of the central source in SNR 1987A using XMM-Newton and INTEGRAL data. XMM-Newton yields an upper limit on the SNR luminosity in the 2–10 keV energy band, $L_X \lesssim 5 \times 10^{34}$ erg s^{-1}. Since the optical depth of the envelope is still large in the XMM-Newton energy band, this constraint carries no useful information about the luminosity of the central source. The optical depth is expected to be small in the hard (20–200 keV) X-ray band of the IBIS telescope aboard the INTEGRAL observatory. We detected no statistically significant emission from SNR 1987A in the INTEGRAL data and obtained an upper limit of $L_X \lesssim 1.1 \times 10^{36}$ erg s^{-1} on the luminosity of the central source in the 20–60 keV band. We also obtained an upper limit on the mass of radioactive ^{44}Ti, $M(^{44}\mathrm{Ti}) \lesssim 10^{-3} M_\odot$. *© 2005 Pleiades Publishing, Inc.*

Key words: *supernovae, pulsars.*

INTRODUCTION

Owing to its proximity, Supernova SN1987A in the Large Magellanic Cloud (LMC) provides a unique opportunity to study the physical processes in supernovae and supernova remnants (SNRs).

At present, it is seen as a rapidly evolving extended object. The observed X-ray emission from the supernova is mainly attributable to the interaction of the shock wave with the matter left from the stellar wind of its progenitor. As a result of this interaction, the luminosity of the supernova increased monotonically over the preceding decade. In December 2002, the supernova brightened sharply when the shock wave reached the so-called inner ring (see Park *et al.* (2004) and references therein).

Based on the Balmer line observations in the optical spectrum, the identification of a massive blue supergiant as the progenitor (Sonneborn *et al.* 1987), and the detection of a neutrino burst (Hirata *et al.*, 1987) occurred simultaneously with the SN event, SN1987A was classified as a Type-II core-collapse supernova. The mass of the progenitor was estimated to be $\sim$15–20$M_\odot$ (Woosley *et al.* 1987). Sunyaev *et al.* (1987) detected strong hard X-ray emission about 169 days after the explosion attributable to the Comptonization of Co^{56} gamma-ray lines in the optically thick envelope. The lines themselves were detected later (see, e.g. Teegarden *et al.* 1989).

The collapse of such a massive star must lead to the formation of a neutron star or a black hole. If a rapidly rotating neutron star with a strong magnetic field was formed, it must appear as a bright Crab-like X-ray pulsar or as an accreting pulsar, which usually have a hard X-ray spectrum with a maximum or appreciable contribution to the luminosity in the INTEGRAL energy band. A neutron star with a weak magnetic field or a black hole can also become a bright X-ray source through the accretion of matter from the envelope. Park *et al.* (2004) obtained an upper limit of $L_X(2\text{–}10\ \mathrm{keV}) < 1.5 \times 10^{34}$ erg s^{-1} on the luminosity of the central source by analyzing Chandra images. The envelope continues to be optically thick, and its optical depth is probably still large in the standard X-ray band and does not allow the central source to be observed directly. It is important to check that it is not bright in the hard X-ray band, where the envelope is transparent for both Thomson scattering and photoabsorption. In addition, we analyzed data from XMM-Newton, which has a higher sensitivity to photons with energies >5 keV than Chandra.

Below, we present the results of our analysis of INTEGRAL and XMM-Newton observations of SNR 1987A and obtain upper limits on the luminosity of the central source.

---

[*] E-mail: `pav\_sht@hea.iki.rssi.ru`

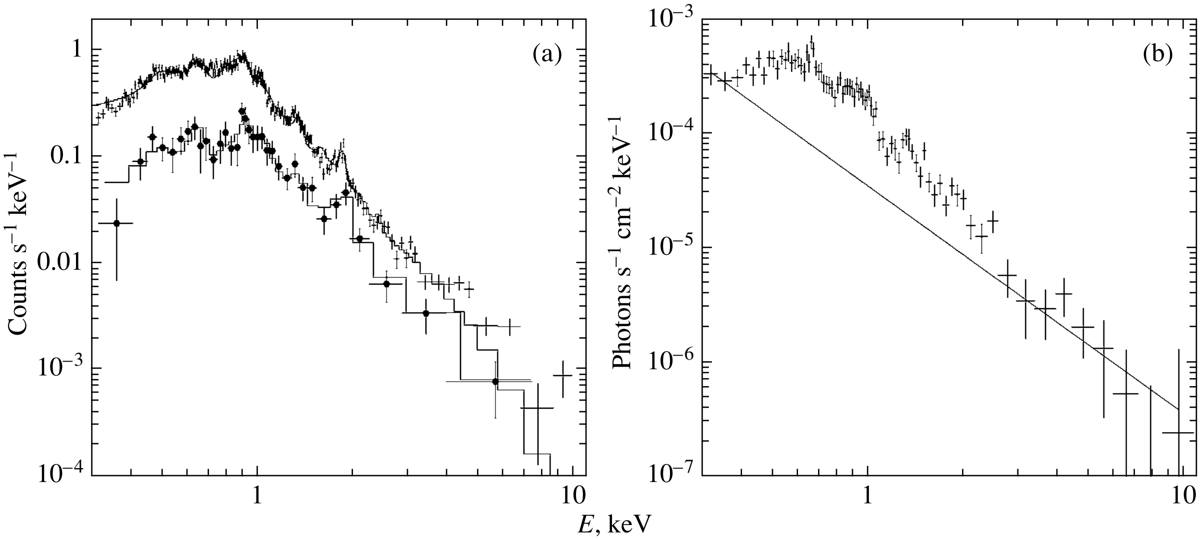

Fig. 1. (a) EPIC PN/XMM Newton spectra of SNR 1987A; the upper and lower curves correspond to the May 2003 and September 2000 pointings, respectively. (b) Deconvolved photon spectrum of SNR 1987A in April 2001; the solid line indicates the power law with a slope of 2 that describes the data at energies above 4 keV.

DATA REDUCTION AND RESULTS

XMM-Newton. SNR 1987A was observed by XMM-Newton in September and November 2000, April 2001, and May 2003. These observations were reduced with the Science Analysis System (SAS) v6.0.0. The data were filtered from soft proton flares by removing the time intervals in which the count rate at energies above 10 keV exceeded significantly the mean level. For the observations in April 2001, because of numerous soft proton flares, the threshold was chosen to be higher than the typical background level in periods without proton flares. To be sure that this did not affect our results, we repeated our analysis with different background thresholds and different regions on the detector used for the background subtraction and found no significant changes in the results obtained.

In contrast to Chandra, the angular resolution of XMM-Newton is insufficient to resolve the SNR; it appears as a pointlike source in the extracted images. However, XMM-Newton is more sensitive to photons with energies >5 keV and, therefore, allows us to reconstruct the spectrum to higher energies. The EPIC PN spectra were extracted from $\sim 30'' - 40''$ circles around the SNR center. The corresponding background spectra were extracted from neighboring regions.

The spectra of SNR 1987A obtained by XMM-Newton in September 2000 and May 2003 together with the NEI model fit (the plane-parallel shock model where the plasma has not reached collisional ionization equilibrium; see Borkowski *et al.* 2001a) are shown in Fig. 1. As we see from the figure, the SNR luminosity increased by more than a factor of 3 over three years, in agreement with predictions of models for the interaction of the supernova shock with circumstellar matter. An excess of hard X-ray emission at energies higher than those in the NEI model was observed in May 2003. This may be associated either with the emission from the central source or with the synchrotron radiation from the SNR shell (see, e.g. Borkowski *et al.* 2001b). Here, we focus our attention on the possible association of the hard X-ray emission with the central source. A detailed analysis of the SNR spectra is not the goal of this paper and can be found, for example, in the papers by Park *et al.* (2004) and Aschenbach (2002).

To obtain a conservative upper limit on the luminosity of the central source, we assume that the total flux observed at high energies is produced by the central source. For this estimation, we used data from early pointings (2000 and 2001), since the contribution of the emission produced by the interaction of the shock with circumstellar matter is smaller for them. Assuming the spectrum of the central source to be a power law with a photon index of 2, we obtained an upper limit (1σ) for its 2–10 keV luminosity, $L_X \lesssim 5 \times 10^{34}$ erg s^{-1} (for an assumed distance to the source of $d = 50$ kpc). This value is slightly higher than the upper limit obtained by Chandra from an imaging analysis (Park *et al.*, 2004).

INTEGRAL. The International Gamma-Ray Laboratory INTEGRAL (Winkler *et al.* 2003) observed the LMC several times in January 2003 with a total exposure of about 1 Ms. In our analysis, we used publicly accessible data obtained by the ISGRI

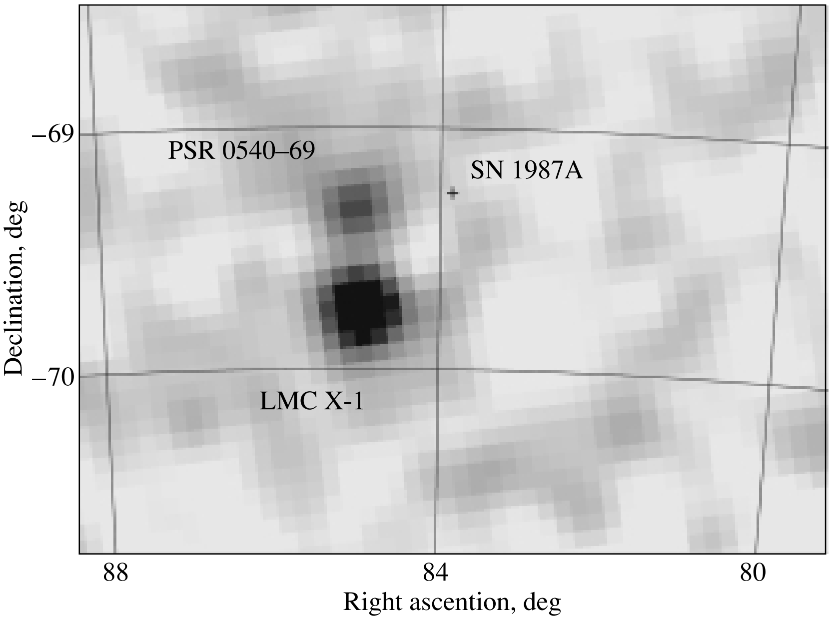

Fig. 2. INTEGRAL image of the LMC region around SN 1987A in the 20–60 keV energy band. The position of SN 1987A is indicates by the cross.

detector of the IBIS telescope. ISGRI is sensitive to photons with energies $E > 20$ keV (Lebrum *et al.* 2003); its data were reduced by a method developed by E.M. Churazov and described by Revnivtsev *et al.* (2004). A detailed analysis of the emission from the Crab Nebula indicates that with the approach and the software used, the conservative estimate for the accuracy of measuring the absolute fluxes from the sources is about 10%.

To investigate the hard X-ray emission from SNR 1987A, we used INTEGRAL/IBIS/ISGRI data in the 20–60 keV energy band, where the ISGRI sensitivity is at a maximum. We reconstructed the image of the central part of the LMC in this energy band (see Fig. 2) and found no statistically significant emission from the SNR with an upper limit on its flux of $F_X \lesssim 3.7 \times 10^{-12}$ erg s^{-1} cm^{-2} (2σ, assuming a Crab-like spectrum), which corresponds to a luminosity of $L_X \lesssim 1.1 \times 10^{36}$ erg s^{-1}.

To compare this result with Chandra and XMM-Newton results, we extrapolate it to the 2–10 keV energy band. The spectra of the pulsars in SNRs are usually fitted by a power law with a photon index of ~1.5–2. For such photon indices, we can estimate the luminosity of the central source in the 2–10 keV energy band corresponding to the INTEGRAL upper limit as $L_X \lesssim (0.6{-}1.6) \times 10^{36}$ erg s^{-1}.

The optical depth of the envelope. The envelope of the supernova immediately after its explosion was optically thick for both photoabsorption and Thomson scattering. This is suggested, for example, by the observations of the Rentgen observatory on the KVANT module of the MIR space station (Sunyaev *et al.* 1987; see also Grebenev and Sunyaev 1987). As the envelope expands and as its density decreases, its optical depth decreases with time as $\tau \propto t^{-2}$. Based on the photoabsorption optical depth of the envelope calculated by Fransson and Chevalier (1987) and assuming that it behaves with time as t^{-2}, we obtain $\tau_{\rm photo} \sim 7$ for 5 keV photons at the epoch of the XMM-Newton observations. The photoabsorption optical depth reaches unity only at energies ~11–15 keV. Thus, the optical depth of the envelope is still large in the Chandra and XMM-Newton energy bands. Therefore, the upper limits obtained by these observatories correspond to a small fraction of the emission from the central source that passed through the envelope, while the actual luminosity of the central source could be much higher.

At the same time, the optical depth for 40 keV photons was estimated to be $\tau_{\rm photo} \sim 0.02$; i.e., the hard X-ray emission escapes from the envelope virtually without being absorbed in it. The Thomson optical depth was estimated to be $\tau_T \sim 0.005{-}0.1$ for various models of the matter distribution in the envelope; therefore, it does not affect the flux either. Even if τ_T were of the order of or slightly larger than unity, this would not change significantly the flux in the 20–60 keV energy band, since the change in energy for a single scattering, $\Delta E/E \approx h\nu/m_ec^2 \sim 0.1$ (Pozdnyakov *et al.* 1983), is small at our energies. Thus, the INTEGRAL observations allow us to look deeper into the envelope without invoking data in

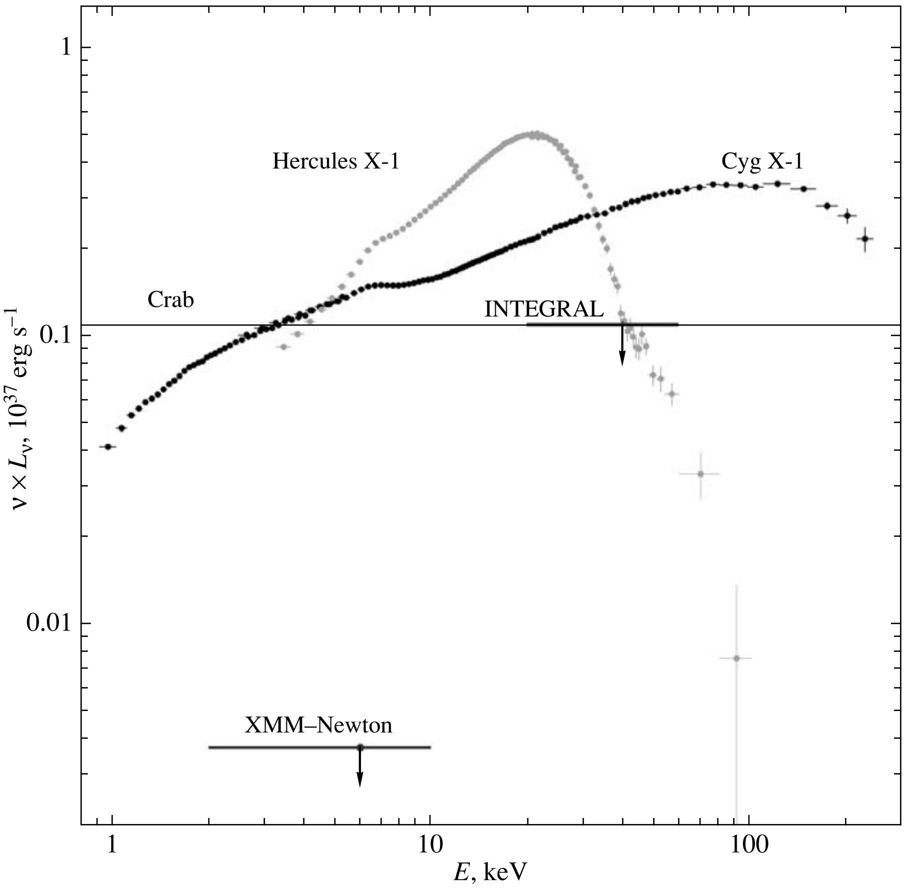

Fig. 3. Spectra for typical systems with an accreting X-ray pulsar, an accreting black hole (Gilfanov *et al.* 2000), and the rotation-powered Crab Pulsar. All spectra were normalized to a luminosity of 2.5×10^{36} erg s^{-1} in the 1–12 keV energy band. This corresponds to the bolometric optical and infrared luminosity (Suntzeff 1997), which is an upper limit on the luminosity of the central source absorbed by the envelope. Also shown are the XMM-Newton and INTEGRAL upper limits on the luminosity of the central source in SNR 1987A.

other energy bands and theoretical models, and its upper limit corresponds to the actual luminosity of the central source.

The absorbed soft X-ray emission must be reradiated in the optical and infrared bands, and the upper limit on the luminosity of the central source can be estimated from the bolometric luminosity of the SNR in these bands. For example, Suntzeff (1997) estimated the bolometric luminosity of the SNR 3600 days after the explosion (about five years before the INTEGRAL observations) to be $\log L \sim 36.1{-}36.4$. This value can be interpreted as an upper limit on the luminosity of the central source corrected for the absorption, which is close to our upper limit obtained from the INTEGRAL data. Obviously, the Spitzer data will help to obtain interesting estimates for the energy of the central source reradiated in the infrared by the optically thick (standard X rays) envelope.

A limit on ^{44}Ti nucleosynthesis. Whereas the main energy source of the early (except the first few weeks) bolometric luminosity of the supernova was the relatively short-lived ($t_{1/2}{\sim}77$ days) ^{56}Co isotope, longer-lived nuclei, for example, ^{44}Ti ($t_{1/2} \sim$ 60 yr), begin to contribute to the bolometric luminosity on long time scales. The ^{44}Ti decay produces two gamma-ray photons with energies of 67.9 and 78.4 keV. Simple estimations of the expected fluxes in these lines give $\sim 3 \times 10^{-13}$ erg s^{-1} cm^{-2} (see e.g., Motizuki and Kumagai 2004), assuming the mass of the synthesized titanium to be $M(^{44}\mathrm{Ti}) = 10^{-4} M_\odot$. To estimate the mass of the synthesized ^{44}Ti, we calculated the observed INTEGRAL fluxes in the 61–73 and 73–88 keV energy bands, $F_\mathrm{X}(61{-}73\,\mathrm{keV}) = (4.30 \pm 1.25) \times 10^{-12}$ erg s^{-1} cm^{-2} and $F_\mathrm{X}(73{-}88\,\mathrm{keV}) = (2.50 \pm 1.60) \times 10^{-12}$ erg s^{-1} cm^{-2}. In the former case, the flux had a formal significance of 3.4σ, but we considered the statistical significance of the line detection to be low. Therefore, to estimate the mass of the synthesized ^{44}Ti, we assumed both fluxes to be upper limits, which yielded $M(^{44}\mathrm{Ti}) \lesssim 10^{-3} M_\odot$.

CONCLUSIONS

Based on XMM-Newton and INTEGRAL data, we obtained constraints on the luminosity of the central source in SNR 1987A. Assuming that the XMM-Newton spectrum of SNR 1987A is attributable to the central source, we obtained an upper limit on its 2–10 keV luminosity uncorrected for absorption, $L_X \lesssim 5 \times 10^{34}$ erg s^{-1}, which is slightly higher than the upper limit obtained by Chandra from an imaging analysis (Park *et al.* 2004). INTEGRAL did not detect any statistically significant emission from the remnant and provided an upper limit for the 20–60 keV luminosity of $L_X \lesssim 1.1 \times 10^{36}$ erg s^{-1}, which corresponds to a 2–10 keV luminosity of $L_X \lesssim (0.6{-}1.6) \times 10^{36}$ erg s^{-1} assuming a Crab-like spectrum. The upper limits on the luminosity of the possible central source in comparison with the typical spectra of the Crab pulsar, an accreting X-ray pulsar, and an accreting black hole are shown on Fig. 3.

Based on the existing calculations of the photoabsorption optical depth of the envelope, we showed that the absorption in the standard X-ray energy band of the XMM-Newton and Chandra observatories is still large, and the upper limit obtained corresponds to the luminosity uncorrected for absorption, which can account for a small fraction of the actual luminosity of the source. At the same time, the optical depth in the INTEGRAL energy band is much less than unity, and the upper limit obtained constrains the actual luminosity of the source.

We also provided an upper limit on the mass of the synthesized ^{44}Ti, $M(^{44}\mathrm{Ti}) \lesssim 10^{-3} M_\odot$.

ACKNOWLEDGMENTS

We wish to thank E.M. Churazov, who developed the methods and software to analyze the IBIS data. We also wish to thank the referee, S.A. Grebenev, for helpful remarks. We used data retrieved through the INTEGRAL Science Data Center (ISDC), Versoix, Switzerland, the Russian INTEGRAL Science Data Center (RSDC), Moscow, Russia, and the XMM-Newton science archive. This work was supported by the Ministry of Industry and Science (project no. NSh-2083.2003.2) and the Nonstationary Phenomena in Astronomy program of the Russian Academy of Sciences. Lutovinov was supported by the Russian Foundation for Basic Research (project no. 04-02-17276).

REFERENCES

1. B. Aschenbach, *Proceed. of the 270. WE-Heraeus Seminar on Neutron Stars, Pulsars, and Supernova Remnants. MPE Report 278*, Ed. by W. Becker, H. Lesch, and J. Truemper (Max-Planck-Institut fuer extraterrestrische Physik, Muenchen 2002), p. 13.
2. K. J. Borkowski, W. J. Lyerly, and S. P. Reynolds, Astrophys. J. **548**, 820 (2001a).
3. K. J. Borkowski, J. Rho, S. P. Reynolds, and K. K. Dyer, Astrophys. J. **550**, 334 (2001b).
4. C. Fransson and R. A. Chevalier, Astrophys. J. **322**, L15 (1987).
5. M. Gilfanov, E. Churazov, and M. Revnivtsev, Mon. Not. R. Astron. Soc. **316**, 923 (2000).
6. S. A. Grebenev and R. A. Sunyaev, Pis'ma Astron. Zh. **13**, 945 (1987) [Sov. Astron. Lett. **13**, 397 (1987)].
7. K. Hirata, T. Kajita, M. Koshiba, *et al.*, Phys. Rev. Lett. **58**, 1490 (1987).
8. F. Lebrun, J. P. Leray, P. Lavocat, *et al.*, Astron. Astrophys. **411**, 141 (2003).
9. Y. Motizuki and Sh. Kumagai, New Astron. Rev. **48**, 69 (2004).
10. S. Park, S. A. Zhekov, D. N. Burrows, *et al.*, Astrophys. J. **610**, 275 (2004).
11. M. G. Revnivtsev, R. A. Sunyaev, D. A. Varshalovich, *et al.*, Pis'ma Astron. Zh. **30**, 430 (2004) [Astron. Lett. **30**, 382 (2004)].
12. G. Sonneborn, B. Altner, and R. P. Kirshner, Astrophys. J. Lett. **323**, 35 (1987).
13. N. B. Suntzeff, *SN 1987A: Ten Years After, the Fifth CTIO/ESO/LCO Workshop, La Serena, Chile, 1997*, Ed. by M. M. Phillips and N. B. Suntzeff; ASP Conf. Ser., 1997; astro-ph/9707324.
14. R. Sunyaev, A. Kaniovsky, V. Efremov, *et al.*, Nature **330**, 227 (1987).
15. B. J. Teegarden, S. D. Barthelmy, N. Gehrels, *et al.*, Nature **339**, 122 (1989).
16. C. Winkler, T. Courvoisier, G. Di Cocco, *et al.*, Astron. Astrophys. **411**, L1 (2003).
17. S. E. Woosley, P. A. Pinto, P. G. Martin, and T. A. Weaver, Astrophys. J. **318**, 664 (1987).

Translated by P. Shtykovskiy

Astronomy Letters, Vol. 31, No. 4, 2005, pp. 263–270. Translated from Pis'ma v Astronomicheskiĭ Zhurnal, Vol. 31, No. 4, 2005, pp. 290–298.
Original Russian Text Copyright © 2005 by Beskin, Eliseeva.

Statistics of Extinct Radio Pulsars

V. S. Beskin[1]* and S. A. Eliseeva[2]

[1] *Lebedev Physical Institute, Russian Academy of Sciences, Leninskiĭ pr. 53, Moscow, 117924 Russia*
[2] *Moscow Institute of Physics and Technology, Institutskiĭ per. 9, Dolgoprudnyĭ, Moscow oblast, 141700 Russia*

Received October 27, 2004

Abstract—We study the statistical distribution of extinct radio pulsars at the stage of an ejector. An important element that distinguishes our study from other works is a consistent allowance for the evolution of the angle of inclination of the magnetic axis to the spin axis. We determined the distribution of extinct radio pulsars in spin period for two models: the model with hindered particle escape from the neutron-star surface and the model with free particle escape. The total number of extinct radio pulsars is shown to be much smaller than that in the model in which the evolution of the angle of axial inclination is disregarded. This is because when the evolution of the angle of axial inclination is taken into account, the transition to the stage of a propeller occurs at much shorter neutron-star spin periods ($P \sim 5$–10 s) than assumed previously. *© 2005 Pleiades Publishing, Inc.*

Key words: *neutron stars, radio pulsars.*

INTRODUCTION

Previously, we showed (Beskin and Eliseeva 2003) that in the case of free particle escape from the surface of a extinct radio pulsar for small distances $d \sim 10$–100 pc typical of the nearest neutron stars, their gamma-ray emission could be detected by the GLAST and INTEGRAL satellites. Our estimate of the intensity of the emission from extinct radio pulsars for free particle escape from the neutron-star surface agrees well with the estimate obtained by Harding *et al.* (2002) for radio-emitting pulsars (see Fig. 1). The point is that the high-frequency emission is associated mainly with primary particles, and, therefore, it can also take place when no secondary plasma is produced. In contrast, for hindered particle escape, the intensity of the emission is so low that the signal from the neutron star cannot be recorded by currently available receivers.

On the other hand, since the intensity of the emission strongly depends on the spin period of the neutron star, radio-quiet pulsars with long spin periods (i.e., those that have long ceased to radiate in the radio frequency range or those with comparatively long spin periods at the stage of radio emission) can no longer be detected even under the assumption of free particle escape from the neutron-star surface. Therefore, we can formulate three necessary conditions under which extinct radio pulsars are detectable: the validity of the model with free particle escape from the neutron-star surface, a relatively small distance to such stars, and a short stellar spin period.

Clearly, the observability of extinct radio pulsars depends on their total number in the Galaxy. We can estimate how many such radio pulsars can be within 100 pc of the Sun from this number. Another no less important parameter is the spin period of the neutron star at which it passes to the stage of a extinct radio pulsar.

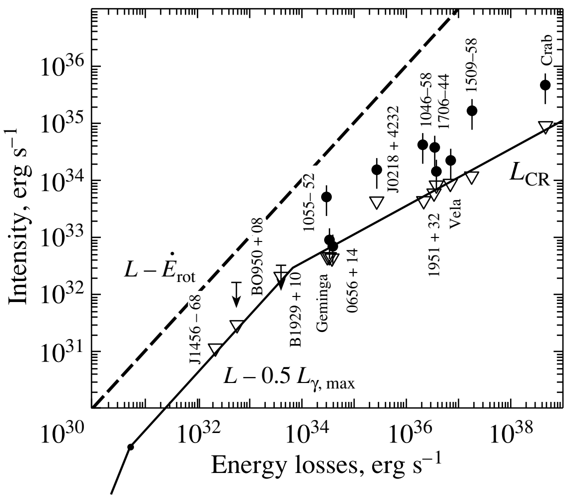

Fig. 1. Predicted and observed dependences of the gamma-ray intensity for radio pulsars on the rate of rotational energy losses under the assumption of free particle escape from the neutron-star surface. Dead radio pulsars correspond to small losses, $L < 10^{31}$ erg s^{-1}.

---

*E-mail: `beskin@lpi.ru`

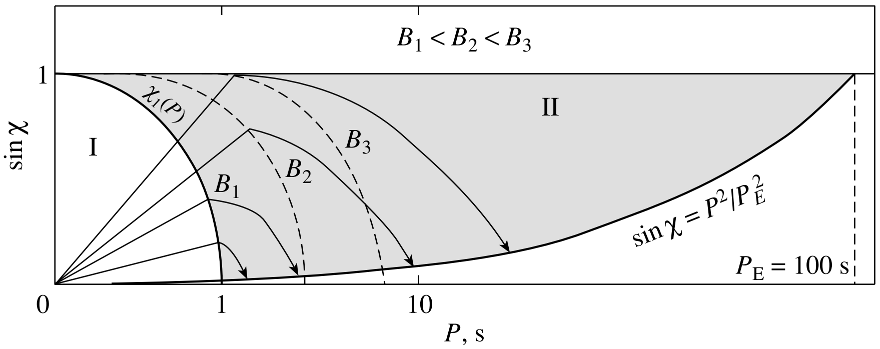

Fig. 2. The evolution of pulsars at the ejector stage under the assumption of hindered particle escape. Regions I and II correspond to active and extinct radio pulsars, respectively. The death line of active radio pulsars is shown for three different magnetic field strengths.

In this paper, we consider the stationary distribution of extinct radio pulsars at the stage of an ejector for two models: the model with hindered particle escape from the neutron-star surface (Ruderman and Sutherland 1975) and the model with free particle escape (Arons 1979). An important element that distinguishes our study from other works is a consistent allowance for the evolution of the inclination of the magnetic axis to the spin axis. On the other hand, we assume that no neutron stars are born at this stage. Finally, we disregard the possibility of magnetic-field evolution.

As a result, we determined the distribution of extinct radio pulsars in spin period. We show that the total number of extinct radio pulsars is much smaller than that in the model in which the evolution of the angle of axial inclination is disregarded. This is because when the evolution of the inclination angle is taken into account, the transition to the stage of a propeller occurs at much shorter neutron-star spin periods ($P \sim 5$–10 s) than assumed previously.

BASIC EQUATIONS

Our objective is to determine the number of neutron stars that are no longer radio pulsars, but have not yet passed to the propeller stage. In other words, we will seek the distribution of neutron stars in the interval $P_{\rm d}(\chi, B) < P < P_{\rm pr}(\chi, B)$, where the period $P_{\rm d}(\chi, B)$ corresponds to the death line of radio pulsars, and the period $P_{\rm pr}(\chi, B)$ corresponds to the transition of neutron stars to the propeller stage (see Figs. 2 and 3). We take into account the fact that both $P = P_{\rm d}(\chi, B)$ and $P = P_{\rm pr}(\chi, B)$ depend on the angle of axial inclination χ (this is a new element that has not been studied previously).

In particular, for the death line of radio pulsars, we will use the expression (Beskin *et al.* 1993)

$$P_{\rm d}(\chi) = B_{12}^{8/15}(\cos\chi)^{0.29} \quad {\rm s}. \tag{1}$$

As regards the transition period to the propeller stage, recall that it can be determined from the condition for the equality between the Schwarzman radius (i.e., the radius at which the pressure of the ambient medium is equal to the magnetodipole radiation pressure) and the radius of the Alfvén surface (Lipunov *et al.* 1996). Therefore, to determine the χ dependence of the transition period $P_{\rm pr}$, it will suffice to recall that the magnetodipole losses

$$L_{\rm md} = -J_r\Omega\dot{\Omega} = \frac{1}{6}\frac{B_0^2\Omega^4R^6}{c^3}\sin^2\chi \tag{2}$$

(B_0 is the magnetic field at the pole of a neutron star with a radius R and a moment of inertia J_r) are proportional to the combination $B_0\sin\chi$. As a result, we obtain

$$P_{\rm pr}(\chi) = P_{\rm E}\sin^{1/2}\chi, \tag{3}$$

where the expression for $P_{\rm E}$ has the standard form (Lipunov *et al.* 1996)

$$P_{\rm E} \approx \frac{R}{c}\left(\frac{Rc^2}{GM}\right)^{1/2}\frac{v_\infty}{c}\left(\frac{B_0^2}{4\pi\rho_\infty v_\infty^2}\right)^{1/4} \tag{4}$$
$$\times\left(\frac{c_\infty}{v_\infty}\right)^{1/2} \approx 10^2\frac{\mu_{30}^{1/2}c_7^{1/2}v_7^{1/2}}{(B_{\rm ext})_{-6}^{1/2}} \quad {\rm s}.$$

Here, ρ_∞ and c_∞ are, respectively, the density and the speed of sound in the interstellar medium (c_7 is in units of 10^7 cm s^{-1}), $B_{\rm ext}^2 = 8\pi\rho_\infty c_\infty^2$ is the corresponding energy density of the magnetic field ($(B_{\rm ext})_{-6}$ is in units of 10^{-6} G), and we naturally assume that the velocity of neutron stars v_∞ is much higher than the speed of sound in the interstellar medium (Popov *et al.* 2000).

To determine the stationary distribution function of extinct radio pulsars, we introduce their distribution function $N(P, \chi; B)$ in spin period P, axial inclination χ, and magnetic field B. It can be found

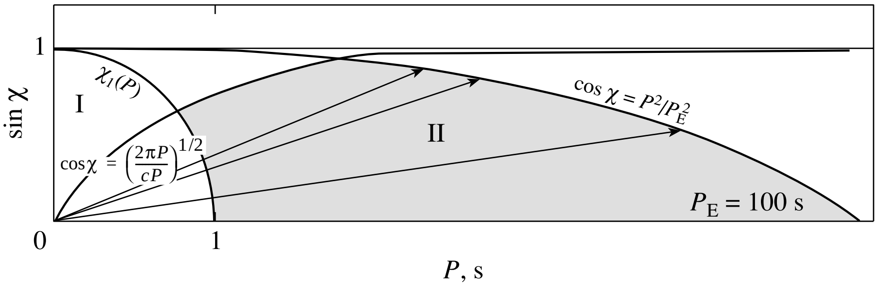

Fig. 3. The evolution of pulsars at the ejector stage under the assumption of free particle escape. Regions I and II correspond to active and extinct radio pulsars, respectively.

from the kinetic equation, which may be represented in general form as

$$\frac{\partial}{\partial P}\left(\frac{\delta P}{\delta t}N\right)+\frac{\partial}{\partial \chi}\left(\frac{\delta \chi}{\delta t}N\right)=U. \qquad (5)$$

In other words, we will ignore the magnetic-field evolution over the lifetime at the ejector stage, as for radio pulsars. The validity of this assumption for normal radio pulsars seems proven, since their lifetime does not exceed the characteristic magnetic-field evolution time (Popov and Prokhorov 2000). As we will show below, when the evolution of the angle of axial inclination is taken into account, the lifetime of neutron stars at the ejector stage before their transition to the propeller stage will also be short.

In Eq. (5), the derivatives $\delta P/\delta t$ and $\delta\chi/\delta t$ are known functions of the magnetic field B, the period P, and the angle of inclination χ. Thus, for example, for the model with hindered particle escape from the radio-pulsar surface, we assume that the energy losses closely match the magnetodipole losses (2):

$$\frac{\delta P}{\delta t}=\frac{2\pi^2}{3}\frac{B_0^2R^6}{J_rPc^3}\approx 10^{-15}B_{12}^2P^{-1}\sin^2\chi, \qquad (6)$$

$$\frac{\delta\chi}{\delta t}\approx -10^{-15}B_{12}^2P^{-2}\sin\chi\cos\chi\ \mathrm{s}^{-1}. \qquad (7)$$

This is because the plasma for hindered particle escape at periods P longer than $P_{\mathrm{d}}(\chi, B)$ will fill only the inner region of the pulsar magnetosphere (Istomin and Mosyagin 1995). It is important that the quantity

$$I_{\mathrm{d}}=\frac{\cos\chi}{P} \qquad (8)$$

is invariant during the evolution, so the angle of axial inclination decreases with time. The characteristic evolution time of the angle χ is equal to the time of change in the spin period of the neutron star.

On the other hand, for free particle escape, we assume that the neutron-star magnetosphere will still be completely filled with plasma that screens the longitudinal electric field. In this case, the magnetodipole losses are known to be completely screened, and all of the energy losses must be associated with the longitudinal currents in the magnetosphere (Beskin *et al.* 1993; Mestel 1999). In other words, the energy losses in this case will be the same as those for radio pulsars. As a result, we obtain (Beskin *et al.* 1993)

$$\frac{\delta P}{\delta t}\approx 10^{-15}B_{12}^{10/7}P^{1/14}\cos^{2d}\chi, \qquad (9)$$

$$\frac{\delta\chi}{\delta t}\approx 10^{-15}B_{12}^{10/7}P^{1/14}\cos^{2d-1}\chi\sin\chi\ \mathrm{s}^{-1}, \qquad (10)$$

where $2d \simeq 1.5$. In this case, the quantity

$$I_{\mathrm{c}}=\frac{\sin\chi}{P} \qquad (11)$$

is invariant during the evolution, so the angle of inclination χ will tend to 90°. As we see, in both cases, the angle of inclination tends to pass into the region where the energy losses are at a minimum.

Finally, the function U on the right-hand side of Eq. (5) is the source of extinct radio pulsars. To make a reasonable assumption about this quantity, recall how we determined it for radio pulsars. Based on the results obtained in the monograph (Beskin *et al.* 1993), we will assume that the birth function of neutron stars can be represented as a product of the probabilities of their initial distributions in angle χ, period P, and magnetic field B:

$$U=U(\chi)U_P(P)U_B(B). \qquad (12)$$

Unfortunately, there is at present no information about the distribution of nascent neutron stars in axial inclination χ (Tauris and Manchester 1999). Therefore, we have to assume that the distribution of neutron stars in their initial value of χ is equiprobable,

$$U(\chi)=2/\pi. \qquad (13)$$

To determine the birth function $U(P)$, we constructed the distribution in period P for pulsars with dynamical ages $\tau_{\mathrm{D}}=P/\dot{P}$ older than the so-called kinetic age $\tau_{\mathrm{kin}}=z/v_\perp$ ($v_\perp$ is the pulsar velocity perpendicular to the Galactic plane), which can be determined for pulsars with known proper motions.

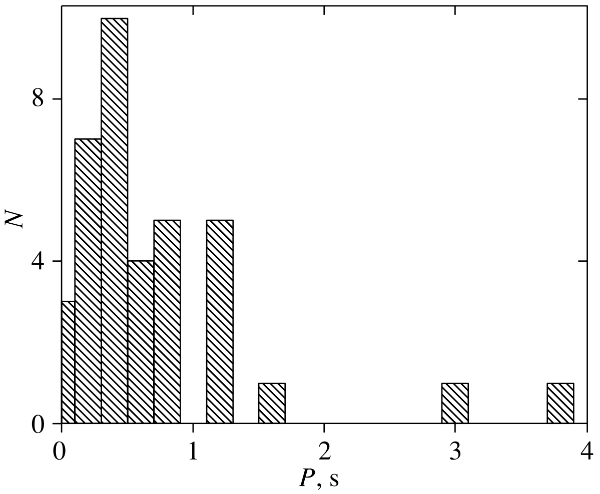

Fig. 4. The distribution of radio pulsars in spin period P for pulsars with $\tau_{\rm D} > \tau_{\rm kin}$. Data from the ATNF catalog were used to construct this distribution.

Here, we use the fact that the thickness of the disk of radio pulsars, $z_{\rm p} \approx 300$ pc, is much larger than the thickness of the disk of supernova remnants, $z_{\rm sn} \approx 10$ pc (Marochnik and Suchkov 1984), where most of the neutron stars are assumed to be born. As a result, the radio pulsars from this sample have not changed their periods significantly; therefore, the distribution of such pulsars in period P must be close to the true birth function of neutron stars $U(P)$.

The derived distribution, which generally matches the distribution obtained previously (Beskin *et al.* 1993), proves to be nearly equiprobable; it at least has no distinct maximum at short periods (see Fig. 4). Therefore, we can assume for radio pulsars with a good accuracy that

$$U_P(P) = U_P = \text{const.} \tag{14}$$

We used this distribution function to analyze the statistical distribution of radio pulsars. On the other hand, we see that a sharp (almost to zero) decrease in the number of radio pulsars is observed at periods $P > 1$ s, whereas the decrease in the number of radio pulsars for the complete sample in the period interval $1 < P < 2$ s is not so appreciable. Therefore, we will assume here that no neutron stars are born at the stage of extinct radio pulsars: $U = 0$.

Finally, recall that we used the following magnetic-field distribution function for radio pulsars:

$$U_B(B) = \frac{\Gamma(\delta+\gamma+1)}{B_0\Gamma(\gamma+1)\Gamma(\delta)}\left(\frac{B}{B_0}\right)^{\gamma}\left(1+\frac{B}{B_0}\right)^{-1-\gamma-\delta}, \tag{15}$$

where $B_0 = 10^{12}$ G and $\gamma = 2$. To refine the power-law dependence of the distribution function for radio pulsars on the magnetic field, we plotted the logarithmic dependence of the number of radio pulsars $N(B > B_0)$ on the magnetic field B for 1348 pulsars the data for which are given in the ATNF Catalog (Manchester). All of the pulsars were divided into two groups by the dimensionless parameter Q that reflects their basic characteristics:

$$Q = 2\left(\frac{P}{1\ \text{s}}\right)^{11/10}\left(\frac{\dot{P}}{10^{-15}}\right)^{-4/10}. \tag{16}$$

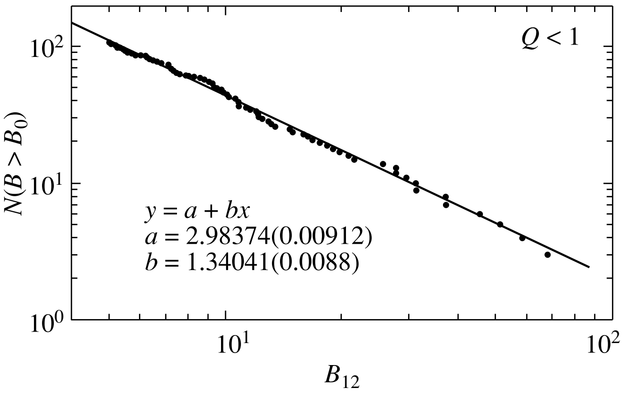

Fig. 5. The distribution of young radio pulsars ($Q < 1$) in magnetic field B_{12} on a logarithmic scale. Data from the ATNF catalog were used to construct this distribution.

The pulsars with $Q > 1$ and $Q < 1$ are, respectively, near and far from the death line (for more details, see Beskin *et al.* 1984). Figures 5 and 6 show the distribution functions for extinct radio pulsars with $Q < 1$ and $Q > 1$, respectively. As we see, the derived exponents are almost equal to those found previously for the statistics of about 400 pulsars. As a result, the distribution function for radio pulsars with $Q < 1$ may be chosen in the form (Beskin *et al.* 1993)

$$N_1(P,\chi;B_0) = 2k_N N_f P\frac{1}{B_k}\left(\frac{B_0}{B_k}\right)^{0.57} \times\left(1+\frac{B_0}{B_k}\right)^{-3.7}\frac{1-\cos\chi}{\sin^2\chi}\cos^{-0.5}\chi\Theta. \tag{17}$$

Here, $k_N \approx 4.4$ is the normalization factor, $\Theta = \theta[P_1(\chi) - P]$, and N_f is the number of normal radio pulsars far from the death line.

Thus, we will consider the stationary distribution of extinct radio pulsars without neutron stars being born at this stage and with the magnetic-field evolution disregarded. Accordingly, the kinetic equation (5) can be written as

$$\frac{\partial}{\partial P}\left(N\frac{\mathrm{d}P}{\mathrm{d}t}\right) + \frac{\partial}{\partial\chi}\left(N\frac{\mathrm{d}\chi}{\mathrm{d}t}\right) = 0. \tag{18}$$

The solution of the kinetic equation for the model with hindered particle escape is given by

$$N(P,\chi) = \frac{F(I_{\rm d})}{\sin\chi}. \qquad (19)$$

For the model with free particle escape from the pulsar surface, we obtain

$$N(P,\chi) = \frac{F(I_{\rm c})}{\cos\chi}. \qquad (20)$$

When solving the kinetic equation for the two models, we must place bounds on the region of extinct radio pulsars. For the model with hindered particle escape from the neutron-star surface (the Ruderman–Sutherland model), these boundaries are determined by the death line of radio pulsars ($\Theta_1 = \theta[P_1(B,\chi) - P]$) and by the boundary of the transition of extinct radio pulsars to the propeller stage ($\Theta_2 = \theta[\sin\chi - P^2/P_{\rm E}^2]$). For the model with free particle escape (the Arons model), in addition to the above boundaries, we must take into account the transition of pulsars to the region where the angle of inclination of the magnetic axis to the spin axis of the neutron star is close to 90° (Beskin and Nokhrina 2004).

Let us designate the regions of active and extinct radio pulsars as regions I and II, respectively. To determine the function $F(I)$, we must join the solutions at the boundary between the regions of active (region I) and extinct (region II) radio pulsars. Equating now the neutron-star fluxes on both sides of the death line, we obtain for the model with hindered particle escape

$$N_2[P_{\rm d}(\chi),\chi] = \frac{\dot{P}_1\left(-\dfrac{{\rm d}\chi_1}{{\rm d}P} - \dfrac{\partial I_{\rm c}/\partial P}{\partial I_{\rm c}/\partial\chi}\right)}{\dot{P}_2\left(-\dfrac{{\rm d}\chi_1}{{\rm d}P} - \dfrac{\partial I_{\rm d}/\partial P}{\partial I_{\rm d}/\partial\chi}\right)} N_1[P_{\rm d}(\chi),\chi], \qquad (21)$$

where all of the derivatives are taken on the death line of pulsars $P = P_{\rm d}(\chi)$. At the same time, for the model with free particle escape, we obtain

$$N_2[P_{\rm d}(\chi),\chi] = N_1[P_{\rm d}(\chi),\chi]. \qquad (22)$$

As a result, in the Ruderman–Sutherland model, we can write the following expression for the function $F(I)$ with sufficient accuracy:

$$F(I_{\rm d}) \approx A(B_{12})\frac{\cos^n\chi}{P^n}, \qquad (23)$$

where $n \approx -0.6$, and $A(B_{12}) \propto B_{12}(1+B_{12})^{-3.7}$ is a function of the magnetic field.

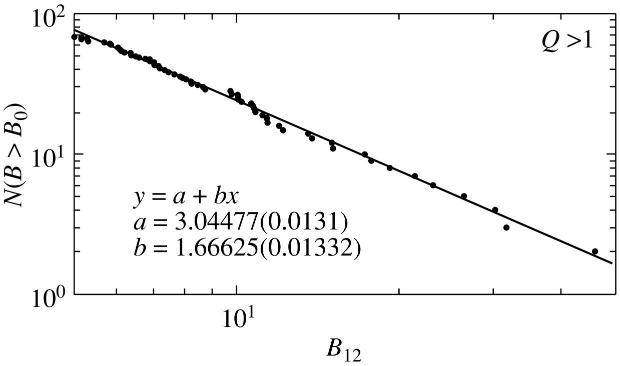

Fig. 6. The distribution of old radio pulsars ($Q > 1$) in magnetic field B_{12} on a logarithmic scale. Data from the ATNF catalog were used to construct this distribution.

THE RUDERMAN–SUTHERLAND MODEL

Let us first consider the statistics of extinct radio pulsars by assuming that the model of hindered particle escape from the neutron-star surface is valid. As we said above, the particle work function is fairly large in this case, and particles fill only the equatorial regions of the magnetosphere with a strongly curved magnetic field, in which secondary particles can still be produced. Therefore, the energy losses for the Ruderman–Sutherland model can be described with a sufficient accuracy by a magnetodipole mechanism.

Let us now turn to Eq. (21), which was derived from the conservation condition for the neutron-star flux on the death line of radio pulsars and which defines the function $F(I)$ and, hence, the distribution of extinct radio pulsars in period P, magnetic field B, and angle χ for the model in question. In this equation, the derivative $\dot{P}_1$ corresponds to the region of active radio pulsars and can be specified by (Beskin *et al.* 1993):

$$\frac{\delta P}{\delta t} \approx 10^{-15} B_{12}^{10/7} P^{1/14} \cos^{1.5}\chi. \qquad (24)$$

At the same time, the derivative $\dot{P}_2$ is specified in the region of extinct radio pulsars, and Eq. (6) should be used for them. Next, let us recall that the region of extinct radio pulsars for the model with hindered particle escape is bounded by the death line of active radio pulsars (1) and the line of the transition of radio pulsars to the propeller stage (3).

Given the aforesaid and that the distribution function for normal radio pulsars is defined by Eq. (17), Eq. (21) can be rewritten as

$$N_2[P_{\rm d}(\chi),\chi] = 0.7 k_N N_f B_{12}^{8/7} \qquad (25)$$
$$\times\,(1+B_{12})^{-3.7}\frac{1-\cos\chi}{\sin^4\chi}\cos^{1.7}\chi(3.5+\tan^2\chi).$$

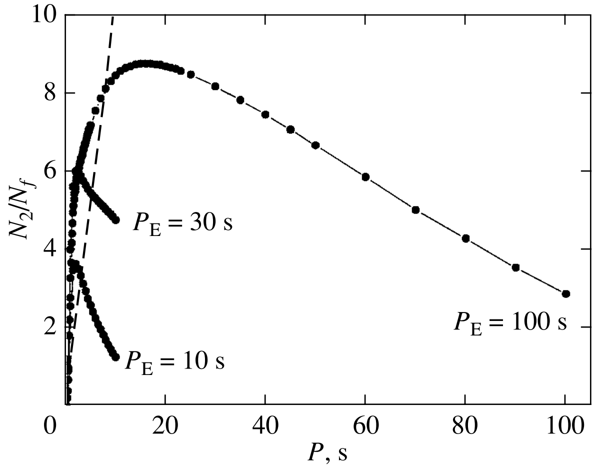

Fig. 7. The distribution of extinct radio pulsars $N_2(P)$ in the model with hindered particle escape with (solid lines) and without (dashed line) allowance for the evolution of the angle of axial inclination.

On the other hand, the solution of the kinetic equation for the model with hindered particle escape from the stellar surface when the distribution of extinct radio pulsars is assumed to be stationary and when no stars are born at this stage and with the magnetic-field evolution disregarded can be represented by Eq. (19). Thus, for the distribution of extinct radio pulsars on the death line, we obtain

$$N_2[P_\mathrm{d}(\chi), \chi] = \frac{F(I_\mathrm{d})}{\sin\chi} = \frac{F(\cos^{0.71}\chi / B_{12}^{8/15})}{\sin\chi}. \quad (26)$$

Let us bring the distribution function for extinct radio pulsars derived from the conservation condition for the flux through the death line into line with form (26). For this purpose, we use the following change of variable:

$$\xi = \frac{\cos^{0.71}\chi}{B_{12}^{8/15}}. \quad (27)$$

As a result, the distribution function for extinct radio pulsars can be finally transformed to

$$N_2[P, B, \chi] = 0.7 k_N N_f B_{12}^{8/7} \quad (28)$$
$$\times (1 + B_{12})^{-3.7} \frac{G(\cos\chi/P)}{\sin\chi} \Theta_1 \Theta_2,$$

where

$$G(\xi) = \frac{1 - c(\xi)}{s^3(\xi)} \left[3.5 + \frac{s^2(\xi)}{c^2(\xi)}\right] c^{1.7}(\xi). \quad (29)$$

We used the following two auxiliary functions:

$$c(\xi) = B_{12}^{0.75} \xi^{1.4} = \cos\chi, \quad (30)$$

$$s(\xi) = [1 - c^2(\xi)]^{1/2} = \sin\chi. \quad (31)$$

Figure 7 shows the distribution of extinct radio pulsars in period P under the assumption of hindered particle escape for three different values of P_E. The results of our numerical calculations shown in this figure are in good agreement with the analytical estimate (23) obtained for the Ruderman–Sutherland model. As we see, the total number of neutron stars at the stage of a extinct radio pulsar when the evolution of the angle of inclination of the magnetic axis to the spin axis is consistently taken into account proves to be much smaller than that in the model in which the evolution of the angle of inclination is disregarded. On the other hand, the number of pulsars with short periods $P \sim 2$–4 s at this stage proves to be even larger than that in the standard model (the dashed line in Fig. 7). This is attributable to the fast transition of neutron stars to the region of small angles of inclination where these are not only accumulated through the decrease in spindown rate, but also disappear due to the transition to the propeller stage.

Finally, it is very important that, when the evolution of the angle of axial inclination is taken into account, the transition to the propeller stage can also occur at short neutron-star spin periods $P \sim 5$–10 s, or even at $P \sim 1$–2 s (see Fig. 2). Indeed, as we mentioned above, the transition to the propeller stage occurs when the Schwarzman radius, which can be determined from the balance between the magnetodipole and external radiation pressures, becomes equal to the Bondi–Hoyle radius. However, since the magnetodipole losses at small angles of axial inclination are essentially suppressed, the transition to the propeller stage takes place even at short neutron-star spin periods:

$$P_\mathrm{pr} = P_\mathrm{E}(\sin\chi)^{1/2}, \quad (32)$$

which is about 5–10 s at $P_\mathrm{E} \sim 100$ s (4). Recall once again that if the model with hindered particle escape from the neutron-star surface is valid, then these cannot be detected with currently available instruments.

THE ARONS MODEL

Let us now discuss the statistics of extinct radio pulsars by assuming that the model with free particle escape from the neutron-star surface is valid. Recall that for this model, the energy losses for both extinct and active radio pulsars are the same and are associated with the longitudinal currents in the magnetosphere. It should also be emphasized that extinct radio pulsars can be detected by their gamma-ray emission precisely for the model of free particle escape at fairly short spin periods and at relatively small distances to such stars.

Let us turn to Eq. (22), which was derived from the condition for the equality between the neutron-star fluxes on both sides of the death line of active radio pulsars. Using the distribution function of normal radio pulsars (17) derived previously (Beskin *et al.* 1993) and refined by using the new data in this paper, let us write the following expression for the distribution function of extinct radio pulsars on the death line:

$$N_2[P_{\rm d}(\chi),\chi] = 0.6k_N N_f B_{12}^{1.1} \quad (33)$$
$$\times (1+B_{12})^{-3.7}\frac{1-\cos\chi}{\sin^2\chi}\cos^{-0.21}\chi.$$

On the other hand, the solution of the kinetic equation for the model of free particle escape from the neutron-star surface can be represented as (20). Accordingly, for the pulsars on the death line, the solution of the kinetic equation is given by

$$N_2[P_{\rm d}(\chi),\chi] = \frac{F(I_{\rm d})}{\cos\chi} = \frac{F[\sin\chi/(B_{12}^{8/15}\cos^{0.29}\chi)]}{\cos\chi}. \quad (34)$$

Recall that, as for the Ruderman–Sutherland model, this solution was obtained by assuming the distribution of extinct radio pulsars to be stationary. At the same time, we disregarded the possibility of stars being born at this stage and the possibility of magnetic field evolution.

Next, it is necessary to consider the boundaries of the region of extinct radio pulsars for the model with free particle escape. This region is bounded by the death line of radio pulsars, the line of the transition of pulsars to the propeller stage, and the line of the transition of pulsars to the region where the angle of inclination of the magnetic axis to the spin axis of the neutron star is close to 90° (see Fig. 3). As in the case of hindered particle escape, the death line of radio pulsars is given by Eq. (1). The transition of extinct radio pulsars to the propeller stage for the model in question is defined as follows:

$$P_{\rm pr}(\chi) = P_{\rm E}\cos^{1/2}\chi. \quad (35)$$

Here, the expression for the limiting period $P_{\rm E}$ also has the standard form (4). Finally, the third bound of the region of extinct radio pulsars is the line of the transition to the region where the angle of axial inclination approaches 90°. For this boundary, we obtained (Beskin and Nokhrina 2004):

$$\cos\chi = \left(\frac{2\pi R}{cP}\right)^{1/2}. \quad (36)$$

Unfortunately, in the case of free particle escape from the neutron star's surface, the distribution function of extinct radio pulsars derived from the flux conservation condition on the death line can be analytically brought into line with (34) only in the approximation of large or small angles of inclination χ. Thus, for example, for small angles of axial inclination,

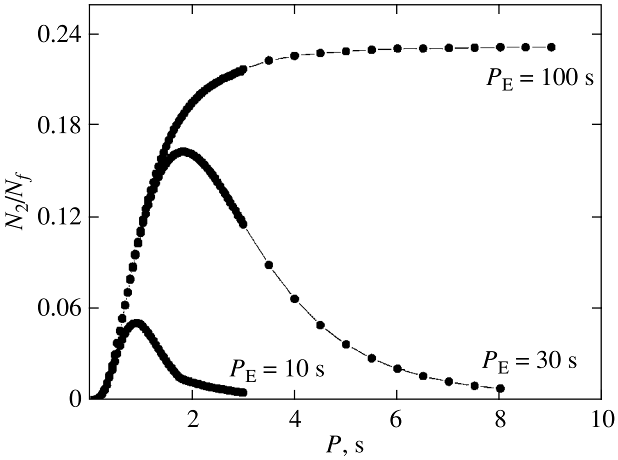

Fig. 8. The distribution of extinct radio pulsars $N_2(P)$ in the model with free particle escape.

$$F(I) = \frac{1}{\pi}k_N N_f B_{12}^{1.1}(1+B_{12})^{-3.7}. \quad (37)$$

At the same time, for angles of inclination close to 90°, we obtain the following expression for the sought function $F(I)$:

$$F(I) = \frac{2}{\pi}k_N N_f B_{12}^{0.2}(1+B_{12})^{-3.7}I^{-1.7}. \quad (38)$$

Using now the approximations for large and small angles of inclination χ, we can approximate the function $F(I)$ for all angles of inclination χ as

$$F(I) = \frac{0.51}{(1+0.1B^{1.7}I^{3.1})^{0.9}}. \quad (39)$$

Thus, the distribution of extinct radio pulsars for the model with free particle escape can ultimately be represented by the function

$$N_2[P,B,\chi] = 0.3k_N N_f \quad (40)$$
$$\times \frac{B_{12}^{1.1}(1+B_{12})^{-3.7}}{\cos\chi[1+0.1B^{1.7}(\sin\chi/P)^{3.1}]^{0.9}}\Theta_1\ldots.$$

Recall that the normalization factor in this expression is $k_N \approx 4.4$, and N_f gives the number of normal radio pulsars far from the death line.

Figure 8 shows the distribution of extinct radio pulsars in spin period P under the assumption of free particle escape from the neutron-star surface. As can be seen from this figure, for the model in question, just as for the Ruderman–Sutherland model, a consistent allowance for the evolution of the angle between the magnetic axis and the spin axis causes the total number of extinct radio pulsars to decrease. Such a decrease stems from the fact that neutron stars can pass to the propeller stage at much shorter spin periods than assumed previously. Indeed, at angles of inclination close to 90°, extinct radio pulsars can pass to the propeller stage even at periods

$$P_{\rm pr} = P_{\rm E}(\cos\chi)^{1/2}. \tag{41}$$

Thus, if the angle of inclination of the magnetic axis to the spin axis is close to 90°, the spin period of a pulsar passing to the propeller stage could be ∼5–10 s.

CONCLUSIONS

Thus, we have determined the distribution of extinct radio pulsars for two models: the model with hindered particle escape from the neutron-star surface and the model with free particle escape. In both cases, we consistently took into account the evolution of the angle of inclination of the magnetic axis to the spin axis of the radio pulsar.

As a result, we showed that for both the model with hindered particle escape from the neutron-star surface and the model with free particle escape, all the details of the calculations, such as the death line of active radio pulsars, the transition of extinct radio pulsars to the propeller stage, and the evolution of extinct radio pulsars, actually require allowing for the evolution of the angle of inclination of the magnetic axis to the spin axis. Unfortunately, with a few exceptions (Beskin *et al.* 1993; Regimbau and de Freitas Pacheco 2001), no consistent analysis of the evolution of the angle of inclination has been performed previously.

As we made sure, such an allowance for the evolution of the axial inclination in analyzing the statistics of extinct radio pulsars causes the total number of such radio pulsars to decrease, thereby making it difficult to detect them with currently available instrumentation (e.g., using the INTEGRAL satellite). Such a situation stems from the fact that when the evolution of the axial inclination is taken into account, the transition of a radio pulsar to the propeller stage can occur even at short periods $P \sim 5$–10 s. Nevertheless, the number of extinct radio pulsars with periods $P \sim 2$–4 s when the evolution of the angle of inclination of the magnetic axis to the spin axis of the neutron star is taken into account turns out to be even larger than that in the standard model. Finally, it should also be noted that the detection of extinct radio pulsars by their gamma-ray emission would be direct evidence for free particle escape from the neutron-star surface.

ACKNOWLEDGMENTS

We would like to thank S.B. Popov and M.E. Prokhorov for fruitful discussions and numerous advice. This work was supported by the Russian Foundation for Basic Research (project nos. 02-02-16762 and 05-02-17700).

REFERENCES

1. J. Arons, Space Sci. Rev. **24**, 437 (1979).
2. V. S. Beskin, Usp. Fiz. Nauk **169**, 1169 (1999) [Phys. Usp. **42**, 1071 (1999)].
3. V. S. Beskin and S. A. Eliseeva, Pis'ma Astron. Zh. **29**, 25 (2003) [Astron. Lett. **29**, 20 (2003)].
4. V. S. Beskin, A. V. Gurevich, and Ya. N. Istomin, Astrophys. Space Sci. **102**, 301 (1984).
5. V. S. Beskin, A. V. Gurevich, and Ya. N. Istomin, *Physics of the Pulsar Magnetosphere* (Cambridge Univ. Press, Cambridge, 1993).
6. V. S. Beskin and E. E. Nokhrina, Pis'ma Astron. Zh. **30**, 754 (2004) [Astron. Lett. **30**, 685 (2004)].
7. A. K. Harding, A. G. Muslimov, and B. Zhang, Astrophys. J. **576**, 366 (2002).
8. Ya. N. Istomin and D. V. Mosyagin, Astron. Zh. **72**, 826 (1995) [Astron. Rep. **39**, 735 (1995)].
9. V. M. Lipunov, *Astrophysics of Neutron Stars* (Nauka, Moscow, 1987) [in Russian].
10. V. M. Lipunov, K. A. Postnov, and M. E. Prokhorov, Astrophys. Space Phys. **9**, 1 (1996).
11. R. N. Manchester, ATNF Catalog, www.atnf.csiro.au/research/pulsar.
12. L. S. Marochnik and A. A. Suchkov, *Galaxy* (Nauka, Moscow, 1984) [in Russian].
13. L. Mestel, *Stellar Magnetism* (Oxford Univ. Press, Oxford, 1999).
14. S. B. Popov, M. Colpi, A. Treves, *et al.*, Astrophys. J. **530**, 896 (2000).
15. S. B. Popov and M. E. Prokhorov, Astron. Astrophys. **357**, 164 (2000).
16. T. Regimbau and J. A. de Freitas Pacheco, Astron. Astrophys. **374**, 182 (2001).
17. M. A. Ruderman and P. G. Sutherland, Astrophys. J. **196**, 51 (1975).
18. T. M. Tauris and R. N. Manchester, Mon. Not. R. Astron. Soc. **306**, 50 (1999).

Translated by V. Astakhov

Astronomy Letters, Vol. 31, No. 4, 2005, pp. 271–279. Translated from Pis'ma v Astronomicheskiĭ Zhurnal, Vol. 31, No. 4, 2005, pp. 299–308.
Original Russian Text Copyright © 2005 by Nadyozhin, Yudin.

The Influence of Coulomb Interaction on the Equation of State under Nuclear Statistical Equilibrium Conditions

D. K. Nadyozhin[*] **and A. V. Yudin**

Institute for Theoretical and Experimental Physics, ul. Bol'shaya Cheremushkinskaya 25, Moscow, 117259 Russia

Received September 10, 2004

Abstract—In the domain of thermodynamic parameters characteristic of the initial collapse of iron stellar cores, we studied the influence of Coulomb interaction on the thermodynamic functions of a plasma under nuclear statistical equilibrium conditions. Our attention was focused on the nuclear component of the matter. We established that including the interaction shifts the equilibrium toward the nuclei with larger charges. However, this effect and the changes in thermodynamic quantities are noticeable only at high densities ($\rho \gtrsim 10^{11}$ g cm^{-3}), i.e., at an advanced stage of gravitational collapse. We also showed that the mean ion model is inadequate in regions with a coupling parameter $\Gamma \sim 1$. We point out a method for modifying the linear mixing model to properly pass to the Debye limit and discuss other multicomponent plasma models. © *2005 Pleiades Publishing, Inc.*

Key words: *plasma astrophysics.*

INTRODUCTION

In this work, we studied the influence of nonideality effects associated with the Coulomb interaction on the equation of state for stellar matter under nuclear statistical equilibrium (NSE) conditions. The Coulomb nonideality of a multicomponent plasma (MCP) is a difficult problem that is so far in the stage of searching for the most efficient approaches to its solution. The NSE state arises in collapsing stellar cores where the electron kinetic energy is much higher than kT due to Fermi degeneracy. Therefore, the Coulomb corrections to the equation of state associated with the electron component are not so significant as those for the ion component.

For clarity and brevity, we focused our attention on the description of the most significant contribution to the equation of state made by the ion–ion correlation interaction. Therefore, in this paper, we present the results of our calculations that include the corrections to the equation of state for an ideal plasma (Nadyozhin and Yudin 2004) attributable to this interaction component alone.

The description of the remaining interaction components involves no fundamental changes; these were also included in our full calculations, which we are going to use to study the hydrodynamics of the gravitational collapse of stellar cores. We took into account the ion–electron interaction using the papers by Stolzmann and Blöcker (2000) and Potekhin and Chabrier (2000), the electron–electron interaction using the papers by Stolzmann and Blöcker (2000) and Kovetz *et al.* (1972), and the contribution of quantum effects to the ion–ion interaction using the papers by Stolzmann and Blöcker (2000) for the liquid phase and Baiko *et al.* (2001) for the crystalline phase.

EQUILIBRIUM MASS FRACTIONS

Under NSE conditions, the dimensionless mass fractions $Y = m_{\rm u}n/\rho$ (n is the number of particles per unit volume, ρ is the matter density, and $m_{\rm u}$ is the atomic mass unit) of various nuclides (A, Z) can be determined from general equilibrium equations that relate the chemical potentials μ of the reacting particles:

$$\mu_{A,Z} = (A - Z)\mu_{\rm n} + Z\mu_{\rm p}, \qquad (1)$$

where $\mu_{A,Z}$, $\mu_{\rm n}$, and $\mu_{\rm p}$ are the chemical potentials of the nuclei (A, Z), neutrons n, and protons p, respectively. When the nuclei are described by Maxwell–Boltzmann statistics and the free neutrons and protons are described by Fermi–Dirac statistics, $Y_{A,Z}$, $Y_{\rm p}$, and $Y_{\rm n}$ can be calculated from the following system of equations (for more details, see Nadyozhin and Yudin 2004):

---

[*] E-mail: `nadezhin@mail.itep.ru`

$$Y_{A,Z} = \omega_{A,Z}\tilde{m}_{A,Z}^{3/2}\frac{m_{\rm u}}{\rho\lambda_T^3} \tag{2}$$
$$\times \exp\left[(A-Z)\psi_{\rm n} + Z\psi_{\rm p} + \frac{Q_{A,Z}}{kT}\right],$$

$$Y_{\rm n} + \sum_{A,Z}(A-Z)Y_{A,Z} = \frac{\theta}{1+\theta}, \tag{3}$$

$$Y_{\rm p} + \sum_{A,Z} ZY_{A,Z} = \frac{1}{1+\theta}, \tag{4}$$

where $\psi_{\rm n,p} \equiv (\mu_{\rm n,p} - m_{\rm n,p}c^2)/kT$ are the reduced chemical potentials of the neutrons and protons; $Q_{A,Z}$ is the binding energy of the nucleus (A,Z); $\tilde{m}_{A,Z}$ is the nuclear mass in atomic mass units $m_{\rm u}$; the dimensions of length are $\lambda_T \equiv \left(\frac{h^2}{2\pi m_{\rm u}kT}\right)^{1/2}$; and $\omega_{A,Z} = \sum_j (2I_j+1)\exp(-E_j/kT)$ is the nuclear partition function. At fixed temperature T, density $\rho = m_{\rm u}(N_{\rm n} + N_{\rm p})$, and ratio $\theta = N_{\rm n}/N_{\rm p}$ ($N_{\rm n}$ and $N_{\rm p}$ are the total numbers of neutrons and electrons per unit volume, both free and bound in atomic nuclei) and given the relationship between $Y_{\rm n,p}$ and $\psi_{\rm n,p}$ that follows from Fermi–Dirac statistics, Eqs. (2)–(4) define the sought mass fractions as functions of three independent variables, ρ, T, and θ.

A FREE ENERGY MODEL

In the overwhelming majority of papers (see, e.g., Stolzmann and Blöcker 2000; Potekhin and Chabrier 2000), the free energy of a system with interaction is represented as a sum of the term that corresponds to an ideal plasma $F^{\rm id}$ and the addition ΔF that describes the interaction:

$$F(\rho, T, \overline{Y}) = F^{\rm id}(\rho, T, \overline{Y}) + \Delta F(\rho, T, \overline{Y}), \tag{5}$$

where F is the specific free energy of the system, and $\overline{Y} \equiv \{Y_j\}$ is the set of mass fractions of various components ($j = {\rm e}^-, {\rm e}^+, {\rm n}, {\rm p}, (A,Z)$ for electrons, positrons, free neutrons and protons, and atomic nuclei, respectively). The Coulomb effects become noticeable only at fairly high densities when the interaction of positrons with electrons, protons, and atomic nuclei may be ignored, which is done in this paper. Therefore, let us represent ΔF as a sum of the terms that correspond to the ion–ion, ion–electron, and electron–electron interactions: $\Delta F = F_{\rm ii} + F_{\rm ie} + F_{\rm ee}$.

Under NSE conditions, the mass fractions $\overline{Y}$ are not independent parameters, but are determined as functions of ρ, T, and θ from the equilibrium condition specified by Eq. (1). In this equation, the chemical potentials of the component i, μ_i ($i = {\rm n}, {\rm p}, (A,Z)$), must include the interaction:

$$\mu_i = m_{\rm u}\left(\frac{\partial F}{\partial Y_i}\right)_{\rho, T, \overline{Y}(j\neq i)} \tag{6}$$
$$= \mu_i^{\rm id} + m_{\rm u}\left(\frac{\partial \Delta F}{\partial Y_i}\right)_{\rho, T, \overline{Y}(j\neq i)}$$

where $\mu_i^{\rm id}$ is the chemical potential calculated from the formulas without interaction, but with the mass fractions determined by including the interaction. Let $\overline{Y}^0$ be the set of mass fractions that is determined from Eqs. (2)–(4) and that corresponds to the equilibrium of the system without interaction described by the free energy $F^{\rm id}$. If the interaction is weak, then we may write in the first approximation $\overline{Y} = \overline{Y}^0 + \Delta\overline{Y}$ and expand F in terms of $\Delta\overline{Y}$:

$$F(\rho, T, \overline{Y}) = F^{\rm id}(\rho, T, \overline{Y}^0) \tag{7}$$
$$+ \sum_i \frac{\partial F^{\rm id}}{\partial Y_i^0}\Delta Y_i + \Delta F(\rho, T, \overline{Y}^0).$$

In what follows, the derivative with respect to Y_i^0 is taken at constant $[\rho, T, \overline{Y}^0(j\neq i)]$. We seek the corrections ΔY_i at constant (ρ, T, θ). In this case, the sum on the right-hand side of Eq. (7) is zero. Indeed, the terms that correspond to the electron–positron component may be written as

$$\frac{\partial F^{\rm id}}{\partial Y_-^0}\left(Y_- - Y_-^0\right) + \frac{\partial F^{\rm id}}{\partial Y_+^0}\left(Y_+ - Y_+^0\right) \tag{8}$$
$$= \mu_-^0\left[Y_- - Y_+ - \left(Y_-^0 - Y_+^0\right)\right] = 0,$$

where the subscripts $-$ and $+$ refer to electrons and positrons, respectively. Here, we used the relationship between the chemical potentials of electrons and positrons ($\mu_- = -\mu_+$) and the electroneutrality equation: $Y_- - Y_+ = Y_-^0 - Y_+^0 = 1/(1+\theta)$. The same result is also obtained for the nuclear component, which may be written as

$$\sum_i \frac{\partial F^{\rm id}}{\partial Y_i^0}\Delta Y_i \tag{9}$$
$$= \frac{1}{m_{\rm u}}\left[\mu_{\rm n}^0\Delta Y_{\rm n} + \mu_{\rm p}^0\Delta Y_{\rm p} + \sum_{A,Z}\mu_{A,Z}^0\Delta Y_{A,Z}\right]$$
$$= \frac{1}{m_{\rm u}}\left[\mu_{\rm n}^0\left(\Delta Y_{\rm n} + \sum_{A,Z}(A-Z)\Delta Y_{A,Z}\right)\right.$$
$$\left. + \mu_{\rm p}^0\left(\Delta Y_{\rm p} + \sum_{A,Z} Z\Delta Y_{A,Z}\right)\right] = 0,$$

where we used condition (1) for the chemical potentials of the nuclei. The last equality in (9) follows from the fact that, according to Eqs. (3) and (4), the changes in fixed quantities, respectively, $\theta/(1+\theta)$ and $1/(1+\theta)$, which are the representatives of the unchangeable (at constant ρ and θ) total numbers of neutrons N_n and protons N_p in the system, appear in parentheses.

Thus, we see that, in the first approximation, to small quantities of the order of $(\Delta Y_i)^2$, the free energy may be calculated using the old mass fractions $\overline{Y}^0$. This is a natural result, since the free energy as a function of the particle mass fractions has a minimum under the chemical reaction equilibrium conditions.

If, however, the interaction is strong, we should proceed from general formulas. Let us introduce the dimensionless free energy of the interaction f in the form

$$\Delta F = \frac{kT}{m_\mathrm{u}} f. \tag{10}$$

We then obtain the following from relation (6) for the reduced chemical potentials:

$$\psi_i = \psi_i^\mathrm{id} + \Delta\psi_i, \tag{11}$$

$$\Delta\psi_i \equiv \left(\frac{\partial f}{\partial Y_i}\right)_{\rho,\, T,\, \overline{Y}(j \neq i)}.$$

Including the Coulomb interaction does not change the relationship between the mass fraction and the chemical potential of the neutrons, since f does not depend on Y_n. Assuming next that the ideal components of the chemical potentials for both protons and nuclei (A, Z), μ^id, and ψ^id, are related to the mass fractions just as in the absence of interaction, we arrive at the following generalization of Eq. (2) to the case where the Coulomb interaction is included:

$$Y_{A,Z} = \omega_{A,Z} \tilde{m}_{A,Z}^{3/2} \frac{m_\mathrm{u}}{\rho\lambda_T^3} \exp\left[(A-Z)\psi_\mathrm{n} + Z\psi_\mathrm{p}^\mathrm{id} + \frac{Q_{A,Z}}{kT} + Z\Delta\psi_\mathrm{p} - \Delta\psi_{A,Z}\right]. \tag{12}$$

The sought mass fractions Y_n, Y_p, and $Y_{A,Z}$ as functions of (ρ, T, θ) can be calculated by numerically solving the system of equations (12) for the adopted set of nuclei (A, Z) together with Eqs. (3) and (4). Technically, the solution is much more complex than that in the absence of interaction where the problem is reduced to the solution of only two equations with two unknowns, ψ_n and ψ_p, by substituting $Y_{A,Z}$ from (2) into (3) and (4). In this case, since $\Delta\psi_\mathrm{p}$ and $\Delta\psi_{A,Z}$ depend, in principle, on the mass fractions of *all* of the nuclei (A, Z) included in the calculations, Eqs. (12) specify the mass fractions of the nuclei only implicitly, and determining the equilibrium values of ψ_n and $\psi_\mathrm{p}^\mathrm{id}$ involves additional difficulties.

Having determined the equilibrium mass fractions with interaction, we can calculate the thermodynamic quantities (pressure P, specific energy E, and specific entropy S) and their derivatives with respect to ρ, T, and θ. This requires that the particle mass fractions calculated by the method described above be substituted into the corresponding formulas defining the thermodynamic quantities in the absence of Coulomb interaction (Nadyozhin and Yudin 2004) and that the following corrections for the Coulomb interaction be applied:

$$\Delta P = \frac{kT}{m_\mathrm{u}} \rho^2 \left(\frac{\partial f}{\partial \rho}\right)_{T,\, \theta}, \tag{13}$$

$$\Delta E = -\frac{kT^2}{m_\mathrm{u}} \left(\frac{\partial f}{\partial T}\right)_{\rho,\, \theta}, \tag{14}$$

$$\Delta S = -\frac{k}{m_\mathrm{u}} \left[f + T\left(\frac{\partial f}{\partial T}\right)_{\rho,\, \theta}\right]. \tag{15}$$

For the entropy of the nuclear component, which corresponds to $F^\mathrm{id}(\rho, T, \overline{Y})$ in Eq. (5), we should use the initial formula

$$S_\mathrm{nuc} = \frac{k}{m_\mathrm{u}} \sum_{A,Z} Y_{A,Z} \times \left\{\frac{5}{2} - \ln\left[\frac{\rho}{m_\mathrm{u}} \frac{Y_{A,Z}}{\omega_{A,Z}} \left(\frac{h^2}{2\pi m_{A,Z} kT}\right)^{3/2}\right] + T\frac{\omega'_{A,Z}}{\omega_{A,Z}}\right\}, \tag{16}$$

where $\omega_{A,Z}$ is the partition function of the nucleus (A, Z). The mass fractions $Y_{A,Z}$ calculated by including the Coulomb interaction must be substituted into this formula. The formula for S_nuc given in our previous paper (Nadyozhin and Yudin 2004) was derived from (16) using Eq. (2), which is valid only in the absence of interaction. An identical contribution from the proton component S_p cannot be explicitly expressed in terms of the proton mass fraction. However, since Y_p is related to $\psi_\mathrm{p}^\mathrm{id}$ just as in the absence of interaction, S_p can be expressed in terms of the formulas without interaction in which $\psi_\mathrm{p}^\mathrm{id}$ is substituted for ψ_p.

Below, we use the quantities averaged over the chemical composition. According to standard rules, the averaging is performed over the mass fractions of the components, for example,

$$\langle Z^n \rangle = \frac{\sum_i Y_i Z^n}{\sum_i Y_i}, \quad \langle A \rangle = \frac{\sum_i A Y_i}{\sum_i Y_i} = \frac{1}{\sum_i Y_i}. \tag{17}$$

The expression for $\langle A\rangle$ in (17) includes the relation $\sum_i AY_i = Y_{\rm p} + Y_{\rm n} + \sum_{A,Z} AY_{A,Z} = 1$ that follows from (3) and (4).

MULTICOMPONENT SYSTEMS

Under physical conditions typical of the collapsing cores of supernovae, the ion–ion correlation interaction that has been well studied for a single-component plasma (SCP), a system with one type of ions, makes the largest contribution to the stellar plasma nonideality. In this case, the reduced free energy of the interaction $f_{\rm ii}$, which is related to $F_{\rm ii}$ by $F_{\rm ii} = \frac{kT}{m_{\rm u}}Y_i f_{\rm ii}$, is known to be a function of only one parameter, $\Gamma = (Ze)^2/(a_i kT)$, which is equal in order of magnitude to the ratio of the mean energy of the interaction between two ions to their mean kinetic energy, where $a_i = (4\pi n_i/3)^{-1/3}$ is the mean separation between the ions. The corresponding parameter for the electron interaction is $\Gamma_{\rm e} = e^2/(a_{\rm e}kT)$ with $a_{\rm e} = (4\pi n_{\rm e}/3)^{-1/3}$. Since $n_{\rm e} = Zn_{\rm i}$, it is related to Γ by the following obvious equality: $\Gamma = Z^{5/3}\Gamma_{\rm e}$.

Our goal was to explore the possibility of generalizing the formulas derived for SCP to the case of a multicomponent plasma (MCP). This is particularly important for matter in NSE conditions, under which tens of nuclei can have appreciable mass fractions and the chemical composition can change abruptly with temperature and density, causing appreciable changes in $\langle Z\rangle$ and $\langle A\rangle$, the mean charge and mass of the nuclei in the plasma. As a base, we used the following Padé approximation for the free energy (see also Stolzmann and Ebeling 1998; Stolzmann and Blöcker 2000):

$$f_{\rm ii}(\Gamma, d) = -\frac{db_0\Gamma^{3/2} + b_2\Gamma^{9/2}\varepsilon_{\rm ii}}{1 - b_1\Gamma^{3/2}(3\ln\Gamma + c_1) + b_2\Gamma^{9/2}}, \tag{18}$$

$$\varepsilon_{\rm ii} = 0.899172\Gamma + 0.274823\ln\Gamma - 1.864179\Gamma^{0.323064} + 1.4018.$$

Here, $b_0 = 1/\sqrt{3}$, $b_1 = \sqrt{3}/8$, $c_1 = 4c_e + 3\ln 3 - 11/3$, $b_2 = 1000(3/4\pi)^{3/2}$, c_e is the Euler constant, and the parameter d, which is equal to unity for SCP, must impart the standard Debye form to $f_{\rm ii}$ for $\Gamma \to 0$. A similar factor can also be used for the coefficient b_1, but including it does not change our conclusions, and we omit it for simplicity. Using precisely this approximation is of no fundamental importance for the questions under discussion; different approximations were used and compared in our calculations. Only its writing in the Padé form is important, as it allows us to change the terms that correspond to one asymptote without affecting significantly the behavior of the function on other asymptotes.

The Mean Ion Model

In the mean ion model, the interaction parameter Γ as well as other possible parameters are substituted with quantities averaged somehow over the chemical composition. Each nucleus is described by its own interaction parameter $\Gamma_i = Z_i^{5/3}\Gamma_{\rm e}$, and the considerations associated with the linear mixing law discussed below lead to the choice of $\langle\Gamma\rangle = \langle Z^{5/3}\rangle\Gamma_{\rm e}$ (see also Hansen *et al.* 1977). Then,

$$F_{\rm ii} = \frac{kT}{m_{\rm u}\langle A\rangle}f_{\rm ii}\left(\langle\Gamma\rangle, \langle d\rangle\right), \quad \langle d\rangle = \frac{\langle Z^2\rangle^{3/2}}{\langle Z\rangle^{1/2}\langle Z^{5/3}\rangle^{3/2}}. \tag{19}$$

The Linear Mixing Law

Many authors (particularly Hansen *et al.* (1977)), have shown that the free energy of a mixture in the region of strong interaction, $\Gamma > 1$, can be accurately represented as a sum of the contributions from each chemical component: $F_{\rm ii} \sim \sum_j Y_j f_{\rm ii}(\Gamma_j)$. Since the principal term in $f_{\rm ii}$ for $\Gamma > 1$ is proportional to Γ, $F_{\rm ii} \sim \sum_j Y_j\Gamma_j$. The mean ion model (19) yields exactly the same result in this limit, which accounts for the adopted method of determining $\langle\Gamma\rangle$. However, we need to determine d to pass to the nonlinear (in Γ) Debye limit. If the parameter d is assumed to be the same for each component of the mixture, then we obtain

$$F_{\rm ii} = \frac{kT}{m_{\rm u}}\sum_j Y_j f_{\rm ii}(\Gamma_j, d), \tag{20}$$

$$d = \frac{\langle Z^2\rangle^{3/2}}{\langle Z\rangle^{1/2}\langle Z^{5/2}\rangle}.$$

However, this determination of d is fraught with the difficulties discussed below. Under NSE conditions there are regions in which both the nuclei for which $\Gamma_i \gg 1$ and those for which their own $\Gamma_j < 1$ make an appreciable contribution to the free energy, and the transition between these two different regimes is very sensitive to the nuances of determining $F_{\rm ii}$. A way out of this situation is to assign an individual value of d_i to each component and to use the following considerations to determine it. In general form, the contribution of the interaction to the specific free energy defined through the binary correlation function g_{ij} and the concentrations n_i and n_j of the ith and jth types of charges is (see, e.g., Kudrin 1974)

$$\Delta F = \frac{1}{2\rho}\int\frac{de^2}{e^2}\int d\mathbf{r}\sum_{i,j} n_i n_j u_{ij}(g_{ij} - 1), \tag{21}$$

$$u_{ij} = \frac{Z_i Z_j e^2}{r},$$

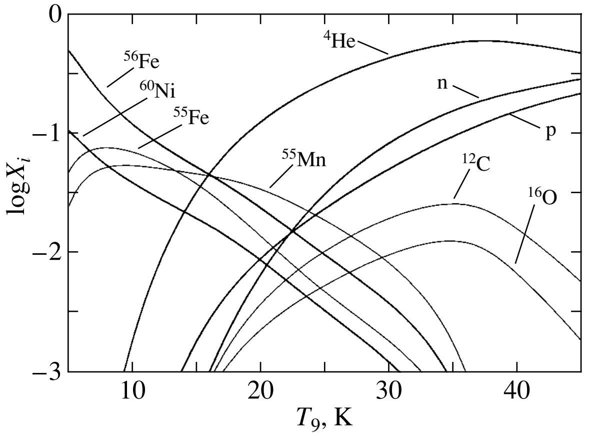

Fig. 1. Mass fractions of several nuclides at $\rho = 10^{12}$ g cm^{-3} and $\theta = 30/26$ without interaction.

where unity was subtracted to allow for the plasma electroneutrality. For a Debye plasma, $g_{ij} = 1 - \frac{Z_iZ_je^2}{kTr}\exp(-\frac{r}{r_d})$, where r_d is the Debye length. If this expression is substituted into (21), then each concentration n_i will appear in the resulting sum with the factor Z_i^2. It is therefore natural to choose d_i in the linear mixing law in such a way that the coefficient of Y_i for $\Gamma_i \to 0$ is also proportional to Z_i^2:

$$F_{\rm ii} = \frac{kT}{m_{\rm u}} \sum_j Y_j f_{\rm ii}(\Gamma_j, d_j), \qquad (22)$$

$$d_j = \sqrt{\frac{\langle Z^2 \rangle}{Z_j \langle Z \rangle}}.$$

Complex Mixing

Analyzing the results of their Monte Carlo simulations, Itoh *et al.* (1979) concluded that these could be accurately described in terms of the following quantities: each component of the mixture is characterized by its interparticle separation a_i, and the interaction between the ith and jth components is characterized by the interaction parameter Γ_{ij}:

$$a_i = \left(\frac{3Z_i}{4\pi \sum_j Z_j n_j}\right)^{1/3}, \qquad (23)$$

$$\Gamma_{ij} = \frac{Z_iZ_je^2}{\frac{1}{2}(a_i + a_j)kT}.$$

If the correlation function is represented as $g_{ij}(r) = \exp(-w_{ij}(r)/kT)$, where w_{ij} is the so-called potential of the mean forces, then w_{ij} can be represented in the range of separations $0.5 \le r/[(a_i + a_j)/2] \le 1.6$, as (Itoh *et al.* 1979)

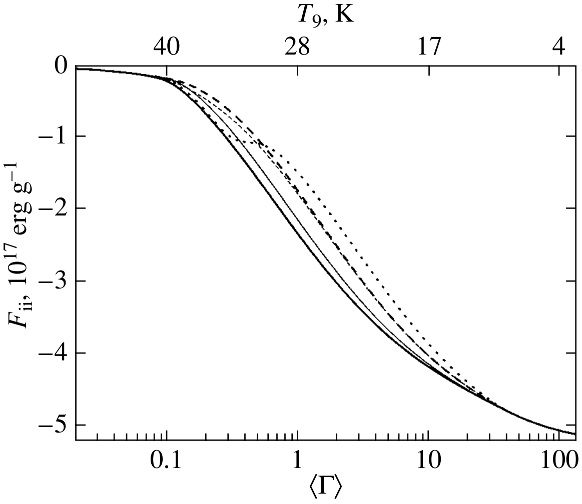

Fig. 2. $F_{\rm ii}$ for various MCP models at the same ρ and θ as those in Fig. 1.

$$w_{ij}(r) = \frac{Z_iZ_je^2}{r} - kT\Gamma_{ij}\left(1.25 - 0.39\frac{2r}{a_i + a_j}\right). \qquad (24)$$

For each term in sum (21) when going to the dimensionless variable ξ related to r by $r = \frac{1}{2}(a_i + a_j)\xi$, g_{ij} in this range of separations is a function of only ξ and Γ_{ij}. When the regions in r, where $g_{ij}(r)$ for the change of variable in question behaves similarly, makes a major contribution to the integral, $F_{\rm ii}$ can be written as

$$F_{\rm ii} = \frac{kT}{m_{\rm u}\sum_k Y_kZ_k} \sum_{i,j} Y_iY_j\tilde{Z}_{ij} f_{\rm ii}(\Gamma_{ij}, d_{ij}), \qquad (25)$$

where $\tilde{Z}_{ij} = \left[(Z_i^{1/3} + Z_j^{1/3})/2\right]^3$. Accordingly, for the case with d common to all components of the mixture and the case where d_{ij} is chosen individually from considerations similar to those that led to formula (22), we obtain

$$d = \frac{\left(\sum_i Y_iZ_i^2\right)^{3/2}\left(\sum_i Y_iZ_i\right)^{1/2}}{\sum_{i,j} Y_iY_j\sqrt{Z_i^3Z_j^3\tilde{Z}_{ij}}}, \qquad (26)$$

$$d_{ij} = \sqrt{\frac{Z_iZ_j\langle Z \rangle}{\langle Z^2 \rangle \tilde{Z}_{ij}}}.$$

Undoubtedly, the above reasoning is not proof of the validity of Eq. (25); its validity must be tested by appropriate calculations.

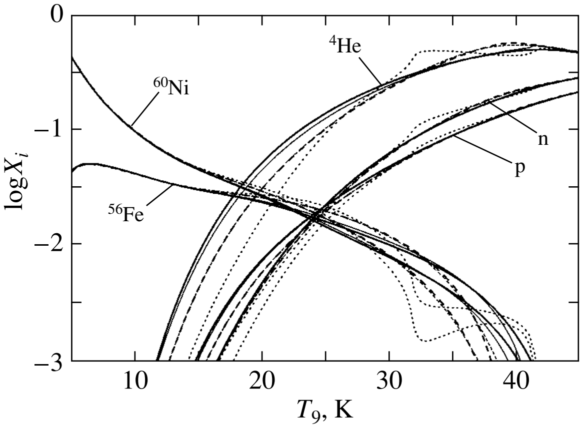

Fig. 3. Mass fractions of several nuclides with interaction for various MCP models at the same ρ and θ as those in Fig. 1.

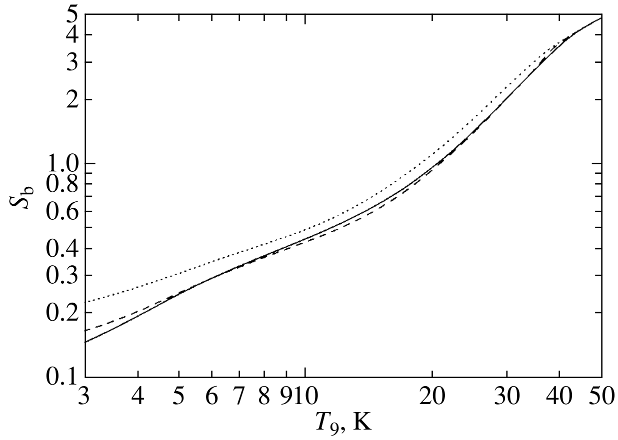

Fig. 4. Dimensionless entropy for $\theta = 30/26$ and $\rho = 10^{12}$ g cm^{-3}.

RESULTS OF CALCULATIONS

Let us first compare $F_{\rm ii}$ calculated using each of the approaches described above for the case where the set of $\overline{Y}$ is determined from NSE conditions for the density $\rho = 10^{12}$ g cm^{-3} and $\theta = 30/26$ in a temperature range that allows us to model most of the important situations: the dominance of heavy elements at low temperatures with the leading role of ^{56}Fe, the transition to equilibrium of lighter elements with rising temperature, and, as a result, the breakup into helium nuclei and free nucleons. The equilibrium mass fractions of several nuclides in the absence of Coulomb interaction are shown in Fig. 1. Figure 2 shows $F_{\rm ii}$ for the described MCP models. The thin and thick solid lines indicate our calculations for the linear mixing law with common and individual values of the parameter d, respectively. The almost coincident thin and thick dashed lines indicate our calculations for the complex mixing model with common and individual values of d; the dotted line indicates our calculations by the mean-ion method. To characterize the interaction, $F_{\rm ii}$ are shown as functions of $\langle\Gamma\rangle$ calculated for the set of $\overline{Y}$ using the mean-ion model. The corresponding temperatures are along the upper axis. In contrast to the mean-ion model, the remaining models predict a smoother behavior of the curves; $F_{\rm ii}$ calculated for the linear mixing law is systematically smaller than that for the complex mixing model. Note that linear mixing causes $F_{\rm ii}$ to be also underestimated in comparison with more accurate computational methods (see, e.g., Hansen *et al.* 1977; Rosenfeld 1996).

Let us now consider the influence of interaction on the nuclear mass fractions. To reveal the characteristic features of the approaches to the MCP problem described above and since the remaining interaction components, whose inclusion makes no fundamental changes, are relatively small, we will demonstrate only the effect from the ion–ion correlation interaction. The interaction effects are shown in Fig. 3, where the lines for each nuclide has the same meaning as in Fig. 2. For convenience, only the lines of ^{4}He, ^{56}Fe, ^{60}Ni, and free nucleons are shown. At both low ($\Gamma \gg 1$) and high ($\Gamma < 1$) temperatures, different models yield almost identical results, which, nevertheless, differ in the intermediate region. Whereas the remaining models predict here a smooth behavior of the mass fractions, the mean-ion model yields a semblance of oscillations. Moreover, choosing a different form of the Padé approximant (18), for example, that from Stolzmann and Blöcker (2000), can even give rise to discontinuities in the lines of equilibrium mass fractions. All of this probably suggests that the mean-ion model is inapplicable for describing the transition from the region with strong interaction with its almost linear dependence of the thermodynamic functions on the mass fraction (in view of the high accuracy of the linear mixing law) to an essentially nonlinear Debye limit.

Figure 3 also demonstrates another interesting phenomenon: the shift of the equilibrium from nuclei with an individual value of $(A-Z)/Z$ close to θ, which dominates under NSE conditions in the absence of interaction (in our case, these are the ^{56}Fe nuclei), to nuclei with a large charge represented in our case by the ^{60}Ni isotope. This could prove to be important for the dynamics of the collapse of an iron stellar core with a mass of $M_{\rm core} \approx 1.4 M_\odot$ that proceeds at lower temperatures not only due to the change in the thermodynamic properties of the matter, but also due to the change in the rate of beta-processes, which changes greatly from nucleus to nucleus and, hence, is sensitive to the chemical composition.

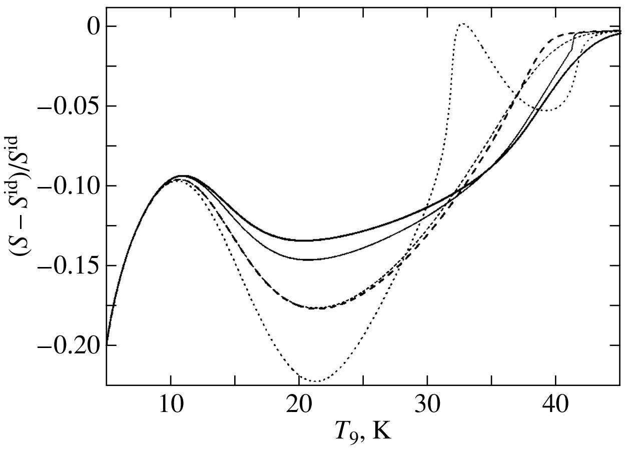

Fig. 5. Relative changes in entropy for various MCP models.

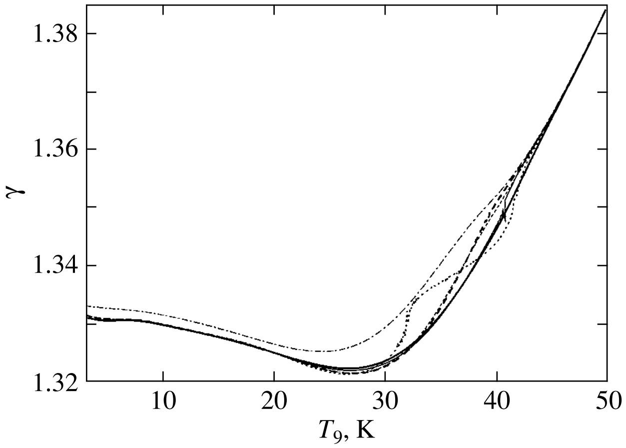

Fig. 6. Adiabatic index versus temperature for various MCP models ($\rho = 10^{12}$ g cm^{-3} and $\theta = 30/26$).

Let us now consider how the procedure for calculating the new equilibrium mass fractions affects the thermodynamics of the matter. For $\theta = 30/26$ and $\rho = 10^{12}$ g cm^{-3}, Fig. 4 shows the dimensionless entropy $S_{\mathrm{b}} = \frac{m_{\mathrm{u}}}{k}S$ for three cases: the dotted line indicates S_{b} without interaction, the solid line indicates our calculation using the linear mixing model with individual values of d_i, and the dashed line indicates our calculation using this model, but without recalculating the mass fractions to the new equilibrium values. Remarkably, although the methods with and without recalculation must be identical in the limit of weak interaction, these also yield similar results in the region where the interaction changes greatly the equilibrium mass fractions; this conclusion is also valid for P and E over a wide range of thermodynamic parameters. However, the quantities defined through the derivatives with respect to the entropy, the pressure, or the internal energy, such as γ, are more sensitive to the difference between these two approaches. Thus, the aforesaid can be summarized as follows: if we are interested only in P, S, and E, then calculating the thermodynamics with the old mass fractions is a satisfactory approximation. If, however, we also need their derivatives (these are important in hydrodynamic calculations!) and nucleosynthesis-related effects, then the mass fractions should be recalculated as described in the section *A Free Energy Model*.

We emphasized the behavior of the specific entropy for the following reasons. First, in contrast to the pressure determined mainly by the electron—positron plasma component, the baryon component of the matter at the high densities concerned makes a major contribution to it, making it sensitive to the MCP model used. Second, in the absence of beta-processes, each element of the stellar matter would collapse with the conservation of its entropy (adiabatic collapse), so a change in entropy directly affects the temperature of the collapsing matter and the parameters of the accompanying neutrino emission. To compare the various MCP models, Fig. 5 for $\rho = 10^{12}$ g cm^{-3} and $\theta = 30/26$ shows the relative deviation, $(S - S^{\mathrm{id}})/S^{\mathrm{id}}$, of the entropy S calculated with interaction from S^{id} without interaction; the lines have the same meaning as those in Fig. 2, i.e., the dotted line indicates our calculation using the mean-ion model etc. In this figure, we clearly see serious deviations of the entropy behavior in the mean-ion model from predictions of other models and the existence of regions in this model where the entropy increases sharply with temperature. Meanwhile, an almost vertical segment at $T_9 \approx 42$ ($T_9 = T/10^9$) is also present in the curve for the linear mixing model with a common value of d. The result of this can be seen from Fig. 6, where the notation is the same as that in Fig. 5. It shows the adiabatic index $\gamma = \left(\frac{\partial \ln P}{\partial \ln \rho}\right)_{S,\theta}$, a quantity that plays a key role in the dynamics of gravitational collapse. There are discontinuities in the $\gamma(T)$ curves at $T_9 \approx 32$ and $T_9 \approx 42$ for the mean-ion model and only at $T_9 \approx 42$ for the linear mixing model with common d. Large-amplitude oscillations that are clearly nonphysical in nature, which are not shown in order not to overload the figure, are actually observed at the locations of the discontinuities. These are associated with the segments of sharp changes in the curves of thermodynamic quantities mentioned above. In principle, choosing a different form of the Padé approximation (18) can give rise to discontinuities at these locations, with the regions of sharp changes being their smoothed variant. The oscillations are the response of our self-consistent nu-

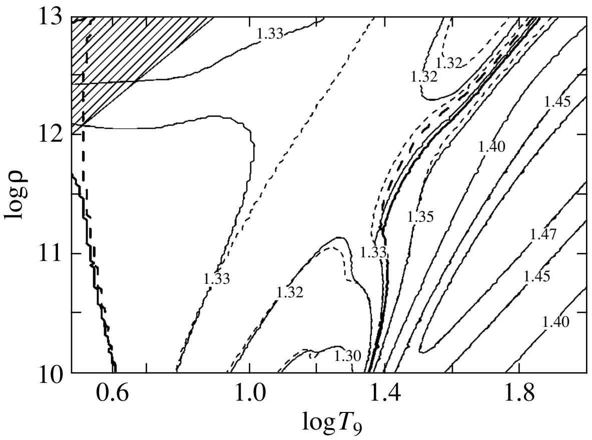

Fig. 7. Line of equal γ for $\theta = 30/26$.

merical procedure for calculating the thermodynamic functions, spline interpolation of the free energy followed by differentiation with respect to the density and the temperature, to these discontinuities. These discontinuities in thermodynamic functions could be attributed to the gas–liquid phase transition in a nuclear plasma near $\Gamma \sim 1$. However, if this transition takes place, it must occur both in mixtures and in homogeneous matter, whereas the initial approximation for SCP (18), as well as others, contain nothing of this kind. We conclude that this is a purely model effect that stems from the fact that some of the approaches to describing MCP are inadequate. Thus, the mean-ion model as well as the linear mixing law with a common parameter d are not satisfactory tools for describing MCP with $\Gamma \sim 1$. In contrast, the linear mixing law with individual d_i as well as the two forms of the complex mixing model yield acceptable results. Note that the complex mixing law is particularly stable, which allows us to use both a common and individual value of d with equal success. The smooth description of the region with $\Gamma \sim 1$ in this model probably stems from the fact that the form of its dependence on Y_i corresponds to the form of the terms of the expansion of thermodynamic quantities in parameter Γ up to the order of $\Gamma^{9/2}$ following the Debye term (see Brown and Yaffe 2001).

Figure 7 shows lines of equal adiabatic index γ for $\theta = 30/26$. The dashed lines indicate the results of our calculations without Coulomb interaction, and the solid lines indicate our calculations with the ion–ion interaction in the linear mixing model with individual values of d_i. The critical value of $\gamma = 4/3$ for the equilibrium of a star is indicated by the heavy lines. In general, including the interaction causes the instability ravine, the region in which $\gamma < 4/3$, to broaden and deepen. However, although these effects are important quantitatively, they do not change the topology of the ravine qualitatively at high and moderate temperatures. At low temperatures, we see a stronger influence of the interaction, but such low temperatures and high densities probably play no role in the supernova collapse. The region in which our data can be inaccurate due to the liquid–crystal phase transition there disregarded in this paper is hatched in the upper left corner of the figure.

CONCLUSIONS

We list our main results below:

Using the procedure for calculating the new equilibrium mass fractions to allow for the Coulomb interaction in a self-consistent way, we found that the equilibrium is shifted toward the nuclei with a larger charge, which could be important for nucleosynthesis-related problems. However, this effect is significant only at high densities $\rho \geq 10^{10}$ g cm^{-3}. Meanwhile, we found only a moderate influence of this procedure on thermodynamic quantities.

When comparing the various MCP models, we concluded that the mean-ion model is inadequate for describing the matter under NSE conditions in the region of moderate interaction, $\Gamma \sim 1$. Although the linear mixing model with a common parameter d appears more plausible, it also yields unsatisfactory results with regard to the adiabatic index γ. Meanwhile, the linear mixing model with individual values d_i and the two complex mixing models yield acceptable and similar results, quantitatively differing only slightly. However, this difference can play a serious role, for example, in determining the type of phase diagrams of the system during the liquid–crystal phase transition. A comparison of the calculations based on these models with the data by de Witt and Slattery (2003) indicates that the complex mixing model is less accurate than the linear mixing model, with its accuracy decreasing with increasing degree of plasma nonideality. Therefore, the linear mixing model is preferred when performing calculations over a wide range of thermodynamic parameters that covers the regions with strong and weak Coulomb interaction with a large number of nuclides.

In conclusion, note that our preliminary (without beta processes) hydrodynamic calculations of the collapse of stars with core masses within the range $M_{\text{core}} = (1.4–2)M_\odot$ using the equation of state calculated here suggest that the typical values of the interaction parameter during the collapse lie within the range $\Gamma \sim (1–20)$. Including the beta-processes and, as a result, matter neutronization inevitably weakens the interaction even more. Thus, the increased attention given to the interaction region $\Gamma \sim 1$ is not only justified, but can also provide a better understanding of the collapse of high-mass stars.

ACKNOWLEDGMENTS

We wish to thank the referee for his constructive remarks. This work was supported by the Russian Foundation for Basic Research (project no. 04-02-16793-a).

REFERENCES

1. D. A. Baiko, A. Y. Potekhin, and D. G. Yakovlev, Phys. Rev. E **64**, 057402 (2001).
2. L. S. Brown and L. G. Yaffe, Phys. Rep. **340**, 1 (2001).
3. H. de Witt and W. Slattery, Contrib. Plasma Phys. **43**, 279 (2003).
4. J. P. Hansen, G. M. Torrie, and P. Vieillefosse, Phys. Rev. A **16**, 2153 (1977).
5. N. Itoh, H. Totsuji, S. Ichimaru, and H. de Witt, Astrophys. J. **234**, 1079 (1979).
6. A. Kovetz, D. Q. Lamb, and H. M. van Horn, Astrophys. J. **174**, 109 (1972).
7. L. P. Kudrin, *Statistical Physics of Plasma* (Atomizdat, Moscow, 1974) [in Russian].
8. D. K. Nadyozhin and A. V. Yudin, Pis'ma Astron. Zh. **30**, 697 (2004) [Astron. Lett. **30**, 634 (2004)].
9. A. Y. Potekhin and G. Chabrier, Phys. Rev. E **62**, 8554 (2000).
10. Y. Rosenfeld, Phys. Rev. E **54**, 2827 (1996).
11. W. Stolzmann and T. Blöcker, Astron. Astrophys. **361**, 1152 (2000).
12. W. Stolzmann and W. Ebeling, Phys. Lett. A **248**, 242 (1998).

Translated by V. Astakhov

Astronomy Letters, Vol. 31, No. 4, 2005, pp. 280–284. Translated from Pis'ma v Astronomicheskiĭ Zhurnal, Vol. 31, No. 4, 2005, pp. 309–314.
Original Russian Text Copyright © 2005 by Kitchatinov, Olemskoi.

Active Longitudes of the Sun: The Rotation Period and Statistical Significance

L. L. Kitchatinov* **and S. V. Olemskoi**

Institute for Solar and Terrestrial Physics, Russian Academy of Sciences, Siberian Branch,
P.O. Box 4026, Irkutsk, 664033 Russia

Received September 23, 2004

Abstract—Using data from the Greenwich catalog, we determined the nonuniformity of the longitudinal distribution of sunspot groups as a function of the rotation period taken for the longitude determination. We estimated the statistical significance of the active longitudes found. A fairly high significance was achieved only for sunspot groups of the Northern Hemisphere and odd activity cycles and only for a synodic rotation period close to 28 days. In this case, one interval of active longitudes was found. The active longitudes are assumed to be associated with the fossil magnetic field frozen in the uniformly rotating radiative zone of the Sun. *© 2005 Pleiades Publishing, Inc.*

Key words: *Sun, active longitudes, rotation.*

INTRODUCTION

A most interesting and still unexplained phenomenon in the magnetic activity of the Sun is its longitudinal nonuniformity. This phenomenon was called active longitudes (Vitinskij 1960, 1969). It is found in the distributions of sunspots (Vitinskij *et al.* 1986; Berdyugina and Usoskin 2003), in the formation of active regions (Benevolenskaya *et al.* 1999), and in the statistics of solar flares (Jetsu *et al.* 1997). The active longitudes are not an exclusive property of the Sun; these are also found on late-type stars (Berdyugina and Tuominen 1998; Korhonen *et al.* 1999). Despite the long history of research on active longitudes, two fundamental questions remain unanswered:

First, it is not clear what rotation period should be taken for the longitude determination. The Sun is known to rotate nonuniformly: the variations of the angular velocity with latitude are about 30% of its mean value, while a 1% change in the rotation period taken for the longitude determination will cause the longitude to change by 360° in a time of less than one solar cycle. Therefore, it is customary to determine the commonly used (synodic) Carrington period, 27.275 days, with a high accuracy. The choice of precisely the Carrington period is conditioned to a greater extent by traditions than by physical arguments. It has long been known that the rotation period of the active longitudes and the centers of activity can take on values from 27 to 29 days (Bumba 1991, 1998). At the same time, determining the rotation rate of the active longitudes is important in understanding their nature. For instance, if the active longitudes are indeed associated with the nonaxisymmetric fossil magnetic field (Kitchatinov 2001; Kitchatinov *et al.* 2001), then these must rotate with a (synodic) period of about 28.8 days, i.e., the rotation period of the solar radiative zone (Schou *et al.* 1998).

Second, it has not yet been shown that the active longitudes are statistically significant. The longitudinal nonuniformity of the solar activity is indistinct. A finite number of solar activity events of a particular type cannot be distributed in longitude absolutely uniformly even if we assume that the probability of occurrence of individual events does not depend on longitude.

In this paper, we attempt to answer these questions. We consider the dependence of the manifestation of active longitudes of sunspots on the rotation period taken for the longitude determination (throughout this paper, we use the synodic periods). We calculate the longitudinal nonuniformity caused by statistical noise in the distribution of a finite number of random events. We establish that the active longitudes cannot be explained by effects of this kind.

THE METHOD

We used data from the Greenwich sunspot catalog for solar cycles 12–17. Following Vitinskij *et al.* (1986), we included only sunspot groups with an area larger than 500 msh. Below, the presence of such a

---

*E-mail: `kit@iszf.irk.ru`

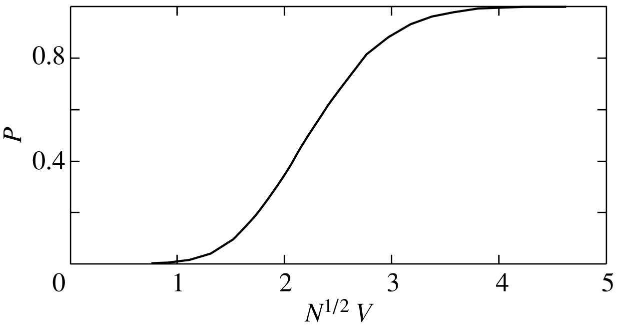

Fig. 1. The probability of variability (3) being less than V as a function $N^{1/2}V$ for a large number N of random events uniformly distributed in longitude.

group on the Sun is called "an event." The coordinates of each event were determined for the day of observations in which the area of the sunspot group was largest. The longitude scale was divided into nine equal 40° intervals. We used a step function for the longitudinal distribution of events,

$$S_i = \frac{9n_i}{N}, \quad i = 1, 2, \dots 9, \tag{1}$$

where n_i number of events in the ith longitude interval, and N is the total number of events. The normalization factor $1/N$ was introduced into (1) to facilitate the comparison of the distributions of events for the Northern and Southern Hemispheres as well as for even and odd activity cycles. The mean value of S over all longitude intervals is unity:

$$\overline{S} = \frac{1}{9}\sum_{i=1}^{9} S_i = 1. \tag{2}$$

The deviations of S_i from unity characterize the nonuniformity of the longitudinal distribution of events. To quantitatively estimate this nonuniformity, we use the quantity

$$V = \sum_{i=1}^{9} \mid S_i - 1 \mid, \tag{3}$$

which we call longitudinal variability.

The Greenwich catalog lists the longitudes, λ_{C}, of sunspot groups determined from the solar rotation period $P_{\mathrm{C}} = 27.275$ d. We can calculate the corresponding longitudes

$$\lambda = \lambda_{\mathrm{C}} + 360^\circ\left(\frac{T}{P} - \frac{T}{P_{\mathrm{C}}}\right) \tag{4}$$

for a different period P, where T is the time. Clearly, if the longitude calculated using (4) does not fall within the interval 0°–360°, then it should be corrected by adding or subtracting a multiple of 360°.

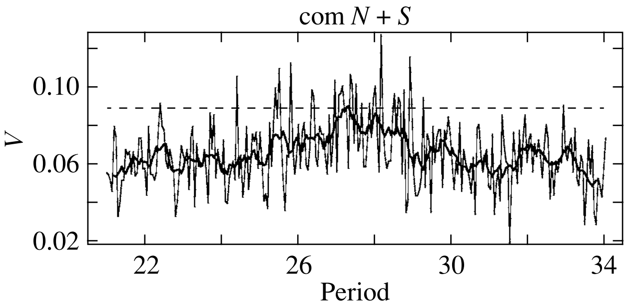

Fig. 2. Variability (3) of the longitudinal distribution of sunspot groups as a function of the rotation period taken for the longitude determination. The thin line indicates the results of our calculations with a 0.05-day step in rotation period. The thick line indicates the centered mean over nine points. The dotted horizontal line indicates the level below which lies the variability for a random, statistically uniform longitudinal distribution of events with a 95% probability.

We can obtain the longitudinal distributions (1) of events for various rotation periods and determine the dependence of the variability V on this period.

In the Appendix, we consider the distribution of random events each of which falls with equal probability within any of the longitude intervals. We show that when the number of such events N is large, the probability that variability (3) is less than a given value of V does not depend on both parameters N and V individually, but is a function of one argument $N^{1/2}V$. This function is shown in Fig. 1. In what follows, it is used to estimate the statistical significance of the active longitudes.

RESULTS AND DISCUSSION

Figure 2 shows variability (3) as a function of the rotation period taken for the longitude determination. The horizontal dotted line indicates the level below which the variability for a random, statistically uniform longitudinal distribution of sunspot groups must be with a 95% probability. We take this 95% level rather subjectively as a statistical significance criterion for the active longitudes. This noise level can also be seen in the difference between the thick and thin lines in the figure. The thin line indicates the results of our calculations performed for several values of the rotation period with a 0.05-day step. The thick line indicates the moving average over nine points. Randomness is clearly present in the longitudinal distribution of sunspot groups.

In the complete statistics of events presented in Fig. 2, the active longitudes are indistinct, although we can note that the variability for the unsmoothed curve reaches the largest values for periods slightly

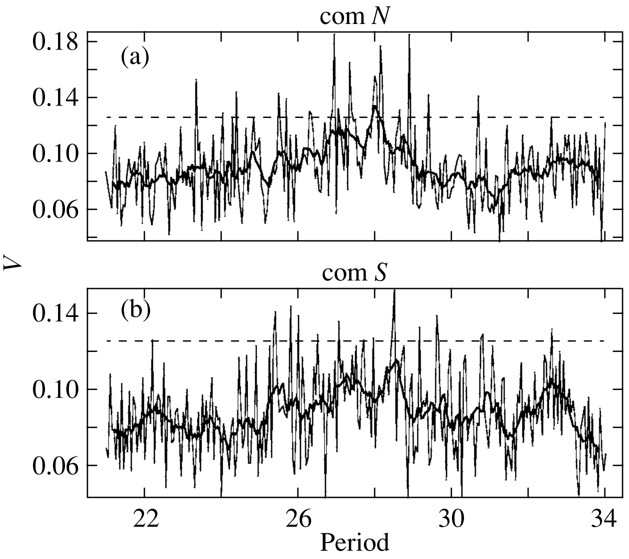

Fig. 3. (a) Variability (3) of the longitudinal distribution of sunspot groups for the Northern Hemisphere as a function of the rotation period taken for the longitude determination; the lines have the same meaning as those in Fig. 2. (b) The same for the Southern Hemisphere.

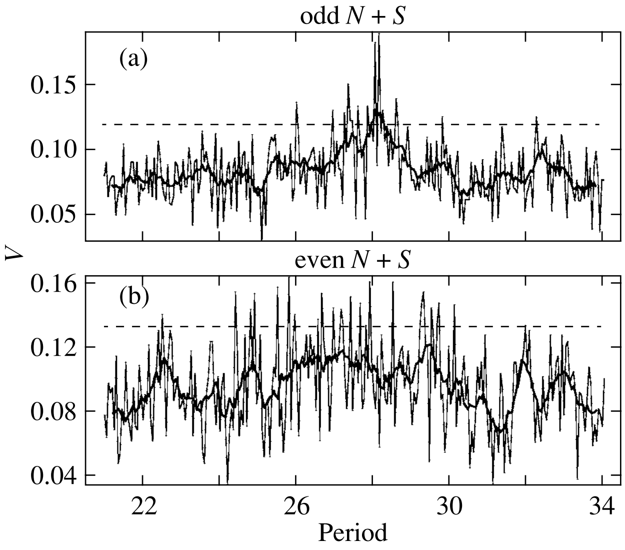

Fig. 4. Variability (3) of the longitudinal distribution of sunspot groups for (a) odd and (b) even cycles as a function of the rotation period; the lines have the same meaning as those in Fig. 2.

longer than 28 days. Almost the entire smoothed curve lies below the level of statistical significance indicated by the dotted line. However, the active longitudes may not coincide for different hemispheres and different activity cycles (Vitinskij *et al.* 1986). Such differences must take place if the phenomenon of active longitudes is associated with the nonaxisymmetric fossil magnetic field (Mordvinov and Kitchatinov 2004; Kitchatinov *et al.* 2001). Therefore, we also calculated the longitudinal variability V separately for the Northern and Southern Hemispheres of the Sun as well as for even and odd activity cycles.

Of course, in this case, the number of event being analyzed decreases, and, hence, the statistical significance criteria become more stringent. Nevertheless, the variability for the events of the Northern Hemisphere shown in Fig. 3 exceeds the 95% confidence level for the interval of periods near 28 days.

Figure 4 shows the longitudinal variability as a function of the rotation period for 11-year cycles with even and odd numbers. The adopted level of statistical significance in the interval of rotation periods slightly longer than 28 d is exceeded significantly only for odd cycles. Figure 5 shows the results for the Northern Hemisphere and odd cycles. Here, the number of events is even smaller, but there is still an interval of rotation periods in which the variability exceeds the adopted level of statistical significance.

The results for the Northern and Southern Hemispheres in even cycles and for the Southern Hemisphere in odd cycles (not shown in the figures) exhibit no statistical significance.

We see from Figs. 3–5 that the rotation period of the statistically most significant active longitudes slightly exceeds 28 days. Figure 6 shows the histograms of distributions (1) for odd cycles and for a rotation period of 28.15 days near which the longitudinal variability reaches its maximum. We see that there is one interval of active longitudes both for the complete set of events without their separation into the hemispheres and separately for the Northern and Southern Hemispheres.

This value is close to, but slightly less than the rotation period of the radiative zone determined from helioseismological data on the rotation of the solar interior regions (Schou *et al.* 1998). Such assertions about the association of local magnetic fields with deeper layers are known to have been made repeatedly (Obridko and Shel'ting 1988). The active longitudes may be actually associated with the nonaxisymmetric fossil field of the Sun. Such a field could be preserved in the almost uniformly rotating radiative zone since the early evolution of the Sun. However, the fossil field can penetrate into the convection zone. Here, it is added to the dynamo field that varies with an 11-year period. The result of this superposition depends on the sign of the field generated by the hydromagnetic dynamo, which may enhance the sunspot activity at the active longitudes in odd cycles and weaken it in even cycles.

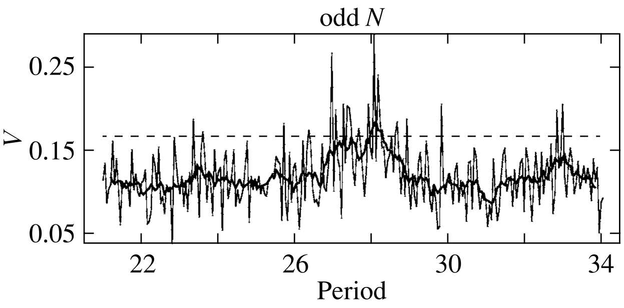

Fig. 5. Variability (3) of the longitudinal distribution of sunspot groups for odd cycles.

However, we failed to choose a suitable spherical harmonic for the hypothetical fossil field with a definite type of symmetry relative to the equator and the rotation axis that would allow us to interpret the above results. Nevertheless, we can note that a dipole-like field whose symmetry axis is parallel to the rotation axes, but is displaced from it toward the active longitudes could yield these results.

APPENDIX

RANDOM EVENTS WITH A UNIFORM LONGITUDINAL DISTRIBUTION

In this Appendix, we estimate the longitudinal nonuniformity in the distribution of a finite number of random events localized in space each of which falls with equal probability within any of the longitude intervals.

Let us divide the full longitude range into K equal $360°/K$ intervals. Let the total number of independent events be N and the individual events fall with equal probability and independently from each other within any of the K longitude intervals. Let us calculate the probability $P_N(n_1, \ldots, n_K)$ that n_1 events fall within the first interval, n_2 events fall within the second interval, etc. Of course, $\sum_{i=1}^{K} n_i = N$. The sought probability is equal to the ratio of the number of ways in which the distribution $(n_1, \ldots, n_K)$ can be obtained to the total number of all possible distributions of events in K intervals. The latter is K^N. The number of ways, $C_N(n_1, \ldots, n_K)$, in which the given distribution of events can be obtained is slightly more difficult to estimate. The result is as follows:

$$C_N(n_1, \ldots, n_K) \tag{5}$$
$$= \frac{N!}{n_1!(N-n_1)!}\,\frac{(N-n_1)!}{n_2!(N-n_1-n_2)!} \cdots \frac{(N-n_1-n_2\ldots-n_{K-2})!}{n_{K-2}!(N-n_1-n_2\ldots-n_{K-1})!}.$$

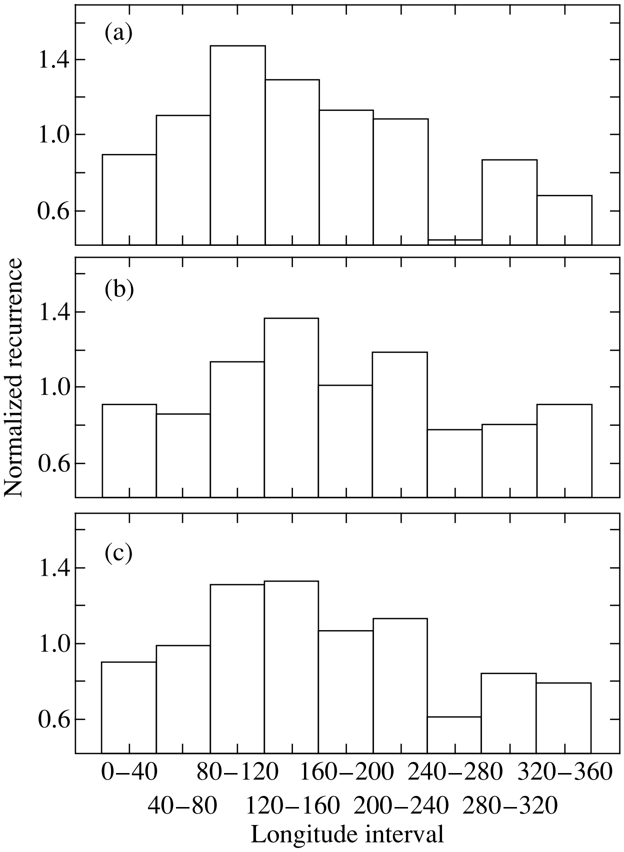

Fig. 6. Normalized longitudinal distributions (1) of sunspot groups for odd cycles (the adopted rotation period is $P = 28.15$ day): (a) for the Northern Hemisphere, (b) for the Southern Hemisphere, and (c) for all sunspots without their separation into the hemispheres.

On the right-hand side of this formula, the first factor is the number of ways of filling the first longitude interval with n_1 events from their total number N. The second factor is the number of ways of filling the second longitude interval with n_2 events from the remaining number $N - n_1$, etc. After obvious simplifications, formula (5) takes the form

$$C_N(n_1, \ldots, n_K) = \frac{N!}{n_1!\, n_2! \ldots n_K!}. \tag{6}$$

Hence, we obtain the final formula for the probabilities

$$P_N(n_1, \ldots, n_K) = \frac{N!}{n_1!\, n_2! \ldots n_K!\, K^N}. \tag{7}$$

Of greatest interest for the purposes of this paper is the probability $p_N(V)$ that the variability defined by formulas (1) and (2) does not exceed V. For the statistics of random events under consideration, $p_N(V)$ is given by the sum of probabilities (7) for the

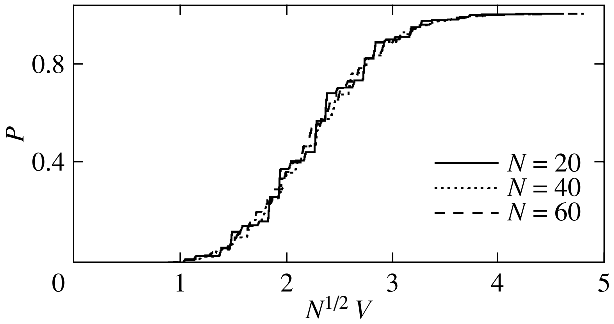

Fig. 7. Probability $p_N(V)$ as a function of $N^{1/2}V$ for $N = 20$, 40, 60 and $K = 9$ intervals. The calculations were performed using formula (8). As N increases, the probability distribution approaches the asymptotic dependence shown in Fig. 1.

distributions whose variability is less than V:

$$p_N(V) = \sum_{n_1,\ldots,n_K} \frac{N!}{n_1!\,n_2!\,\ldots n_K!\,K^N} \times \Delta\left(V - \left|\frac{K_{n_1}}{N} - 1\right| - \left|\frac{K_{n_2}}{N} - 1\right| \ldots - \left|\frac{K_{n_k}}{N} - 1\right|\right), \tag{8}$$

where summation is over all possible distributions $(n_1, \ldots, n_K)$, and Δ is a step function:

$$\Delta(x) = \begin{cases} 0, & x < 0 \\ 1, & x \geq 0. \end{cases} \tag{9}$$

Calculations using formula (8) are difficult to perform, but an appropriate numerical program can be written (the difficulties associated with the large numbers that arise in calculating the factorials can be easily circumvented). However, the computational time increases rapidly with N, and calculations for $N \geq 100$ can no longer be performed in a reasonable time. The typical values of N for the sunspot statistics used in this paper are several thousands. The situation is saved by the similarity rule: at large N, the probability $p_N(V)$ is a function of one argument, $N^{1/2}V$, rather than two independent variables, N and V. Figure 1 shows precisely this function. As we see from Fig. 7, this similarity rule holds even at moderate N accessible for direct numerical calculations. Thus, we can find an approximation for the asymptotic dependence of $p_N(V)$ on $N^{1/2}V$ through calculations for moderate N and then use the result for arbitrary N.

Of course, numerical calculations cannot be a rigorous proof of mathematical rules, particularly the similarity rule under discussion. However, the results of Fig. 7 leave virtually no doubt that it is valid.

ACKNOWLEDGMENTS

This work was supported by the Russian Foundation for Basic Research (project nos. 02-02-16044 and 02-02-39027) and the INTAS (grant no. 2001-0550).

REFERENCES

1. E. E. Benevolenskaya, J. T. Hoeksema, A. G. Kosovichev, and P. H. Scherer, Astrophys. J. **517**, L163 (1999).
2. S. V. Berdyugina and I. Tuominen, Astron. Astrophys. **336**, 25 (1998).
3. S. V. Berdyugina and I. Usoskin, Astron. Astrophys. **405**, 1121 (2003).
4. V. Bumba, Bull. Astron. Inst. Czech. **42**, 381 (1991).
5. V. Bumba, Publ. Astron. Inst. Czech. **88**, 1 (1998).
6. L. Jetsu, S. Pohjolainen, J. Pelt, and I. Tuominen, Astron. Astrophys. **318**, 293 (1997).
7. L. L. Kitchatinov, Astron. Zh. **78**, 934 (2001) [Astron. Rep. **45**, 816 (2001)].
8. L. L. Kitchatinov, M. Jardine, and A. Collier Cameron, Astron. Astrophys. **374**, 250 (2001).
9. H. Korhonen, S. V. Berdyugina, T. Hackman, *et al.*, Astron. Astrophys. **346**, 101 (1999).
10. A. V. Mordvinov and L. L. Kitchatinov, Astron. Zh. **81**, 281 (2004) [Astron. Rep. **48**, 254 (2004)].
11. V. N. Obridko and B. D. Shel'ting, Issled. Geomagn. Aeron. Fiz. Solntsa **83**, 3 (1988).
12. J. Schou, H. M. Antia, S. Basu, *et al.*, Astrophys. J. **505**, 390 (1998).
13. Yu. I. Vitinskij, Izv. G. Astron. Obs., No. 163, 96 (1960).
14. Yu. I. Vitinskij, Solar Phys. **7**, 210 (1969).
15. Yu. I. Vitinskij, M. Kopetskiĭ, and G. V. Kuklin, *Statistics of Solar Sunspot Activity* (Nauka, Moscow, 1986) [in Russian].

Translated by G. Rudnitskiĭ

Astronomy Letters, Vol. 31, No. 4, 2005, pp. 285–290. Translated from Pis'ma v Astronomicheskiĭ Zhurnal, Vol. 31, No. 4, 2005, pp. 315–320.
Original Russian Text Copyright © 2005 by Zaitsev, Zlotnik, Aurass.

The Efficiency of Electron Acceleration in Solar Type-IV Radio Pulsations with a Zebra Pattern

V. V. Zaitsev[1]*, E. Ya. Zlotnik[1], and H. Aurass[2]

[1]*Institute of Applied Physics, Russian Academy of Sciences, ul. Ul'yanova 46, Nizhni Novgorod, 603950 Russia*
[2]*Astrophysikalisches Institut, An der Sternwarte 16, D-14482 Potsdam, Germany*

Received September 22, 2004

Abstract—Based on a comprehensive analysis of the October 25, 1994 event, we consider the balance of energetic particles in a type-IV solar radio emission source with a zebra-type fine structure (in a coronal magnetic loop). The zebra pattern is formed through the injection of fast electrons into a trap and the formation of a ring-type nonequilibrium electron distribution function. We estimated the characteristic zebra-pattern lifetime, which is determined by the escape of fast particles from the trap into the loss cone. In addition, we determined the number of fast particles that must be injected into the trap to provide the observed radio brightness temperature in zebra-pattern stripes by analyzing the plasma emission mechanism responsible for the zebra-pattern generation. As a result, we estimated the efficiency of the electron acceleration mechanism in coronal magnetic loops at the post-flare evolutionary phase of an active region. © *2005 Pleiades Publishing, Inc.*

Key words: *solar corona, radio emission mechanisms, electron acceleration.*

INTRODUCTION

Many varieties of electromagnetic radiation that arise in the solar and stellar coronas are associated with suprathermal particles, which, in turn, are produced by various acceleration mechanisms. In general, the latter remain unknown, or there are many uncertainties in identifying the acceleration mechanisms in each specific type of events. Therefore, an important problem of solar and stellar physics is to estimate the efficiency of the acceleration processes in various events. For example, an average solar flare with electron energy release $E_e(\epsilon > 20\ \mathrm{keV}) \simeq 10^{29}$ erg during 100 s must provide a fast electron efficiency $\sim 3 \times (10^{35}{-}10^{36})\ \mathrm{s}^{-1}$, as follows from observations of the hard X-ray emission that accompanies a flare (Miller *et al.* 1997). Large flares can provide an electron acceleration rate that is three orders of magnitude higher.

Filling low coronal magnetic loops, fast electrons generate gyrosynchrotron radiation that manifests itself as microwave emission observed from solar flares in the centimeter wavelength range (Zheleznyakov 1964). Type-IV radio bursts, broad-band continuum emission in the meter wavelength range with a high brightness temperature, constitute another variety of sporadic radio emission that arises several minutes after a solar flare. Occasionally, type-IV bursts appear in the form of broad-band pulsations with periods of 1–3 s, which are probably suggestive of a pulsating particle acceleration mechanism in type-IV sources. The efficiency of this mechanism has not yet been studied adequately, although type-IV pulsations are a fairly common phenomenon. Recently, Aurass *et al.* (2003) and Zlotnik *et al.* (2003) summarized the results of a comprehensive study of type-IV pulsations accompanied by the so-called zebra pattern, another variety of the fine structure of type-IV bursts in the form of parallel-drifting quasi-harmonic stripes in the dynamic spectrum. These studies included an analysis of data from the Tremsdorf dynamic radio spectrograph and the Nançay Radio Heliograph, YOHKOH soft X-ray data, and Hα observations of an active region (AR 7792 on October 25, 1994). As a result, it was possible to restore the shape of the coronal magnetic loop in which the pulsations and the zebra pattern were generated and to determine the relative positions of their sources and other important parameters.

Based on these data, we analyze the efficiency of the acceleration mechanism required to account for the observed radio brightness temperature and interpret the temporal dynamics of the event as a whole by discussing the parameters of the acceleration mechanism that can take place in a coronal magnetic loop.

---

*E-mail: `za130@appl.sci-nnov.ru`

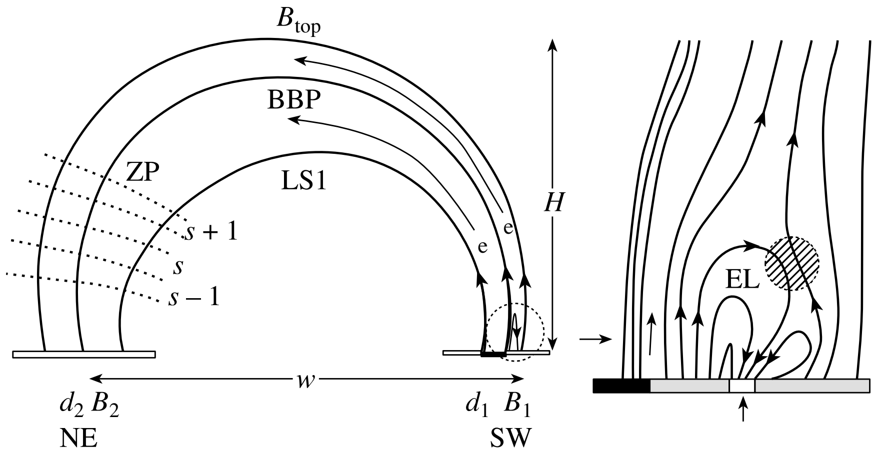

The source model constructed from optical, X-ray, and radio observations (Zlotnik *et al.* 2003). The coronal loop LS1 is the main source of the broad-band pulsations (BBP) and the zebra pattern (ZP): the BBP-exciting beams of fast electrons are injected at the southwestern (SW) footpoint of the loop. The zebra pattern arises at the levels of the double plasma resonance $f_p = sf_B$ (indicated by dotted lines) in the northeastern (NE) part of LS1. A magnified image of the region highlighted by the dotted circumference at the SW footpoint of the loop is shown on the right: electrons are accelerated at the footpoints of the emerging loop EL; accelerated electrons penetrate into LS1, the source of the pulsations and the zebra pattern, through the reconnection region (the hatched circle).

PARAMETERS OF THE CORONAL MAGNETIC LOOP AND THE ORIGIN OF THE SPECTRAL FINE STRUCTURE

Let us briefly summarize the basic data on the parameters of the coronal magnetic loop in which the broad-band quasi-periodic pulsations and the zebra pattern were generated in the October 25, 1994 event (Aurass *et al.* 2003; Zlotnik *et al.* 2003) and on their generation mechanisms.

A schematic view of the source is shown in the figure. The magnetic field strengths at the right and left footpoints of the loop were $B_1 = 200$–300 G and $B_2 = 20$–30 G, respectively; the strength at the top of the loop was $B_{top} \simeq 2$ G. The loop footpoint areas were $S_1 = 1.7 \times 10^{18}$ cm^2 and $S_2 = 2.5 \times 10^{19}$ cm^2 for the right and left footpoints, respectively; the height of the loop was $H = 7.5 \times 10^9$ cm, and the separation between the footpoints was $w = 1.3 \times 10^{10}$ cm.

An analysis of the possible generation mechanisms for the broad-band quasi-periodic pulsations led us to conclude (Zlotnik *et al.* 2003) that the MHD oscillations of the coronal magnetic loop cannot be the pulsation source in the event under consideration: the Alfvén velocity inside the magnetic flux tube, which determines the period of its free oscillations, changes significantly when going from the top of the loop to its footpoints, ruling out the possibility of synchronous pulsations over a wide frequency range. According to Zlotnik *et al.* (2003), the periodic injection of electrons into a magnetic trap and the excitation of plasma waves through beam instability as the electron beam propagates along the loop (similar to type-III bursts) are most likely responsible for the broad-band pulsations. This hypothesis is supported, first, by the observed negative frequency drift of individual pulses and, second, by the motion of the source of an individual pulse along the loop axis from the right footpoint to the top recorded with the Nançay Radio Heliograph.

As regards the electron injection periodicity, the two most plausible mechanisms capable of producing this effect are as follows: the current-sheet oscillations (periodic reconnection) analyzed by Tajima *et al.* (1987) and the RLC oscillations of the emerging magnetic loop EL (Zaitsev *et al.* 1998). However, the former cannot provide a high Q factor of the oscillations (more than a hundred pulsations were observed in the October 25, 1994 event). Therefore, the RLC oscillations of the loop, which provide the observed periods and Q factor of the radio pulsations, are most likely responsible for the periodic injection of electrons. The electron acceleration periodicity mechanism at the footpoint of the current-carrying loop EL is as follows (Zlotnik *et al.* 2003): the charge separation produced by convective flows gives rise to a longitudinal (along the magnetic field) component of the electric field $E_\parallel$ and the associated radial component of the magnetic field B_r; the latter is modulated by the oscillations of the current in the magnetic flux tube (determined by the equivalent RLC circuit), causing the accelerating field $E_{\|}$ to vary periodically.

According to the observations by Aurass *et al.* (2003), fast electrons were injected during the generation of quasi-periodic pulsations from the right footpoint of the loop with a stronger magnetic field. The velocity of the injected electrons was $v = 1.1 \times 10^{10}$ cm s^{-1}. The pulsations were observed by the Radio Heliograph in the right half of the magnetic loop, and their total duration was $\tau_{\mathrm{p}} \approx 3.5$ min. Electrons were probably accelerated in the small emerging loop EL, which was rooted at the right footpoint of the main loop and had a reconnection region (indicated in the figure by the circle on the right) with it. Accelerated electrons could penetrate into the main loop through this region and through the left footpoint of the emerging loop.

The source of the zebra pattern (denoted by ZP in the figure) was observed in the left part of the coronal loop with a weaker magnetic field in the frequency range 130–220 MHz. Our previous analysis (Zlotnik *et al.* 2003) showed that, in this case, the zebra pattern originated from the excitation of plasma waves when the following double plasma resonance condition was satisfied: the upper hybrid resonance frequency $\omega_{\mathrm{uh}} = \sqrt{\omega_{\mathrm{p}}^2 + \omega_B^2}$ coincides with one of the electron gyrofrequency harmonics ω_B, i.e., $\omega_{\mathrm{uh}} = s\omega_B$ (here, ω_{p} is the Langmuir frequency, and s is the harmonic number). More than ten harmonics with numbers from $s = 10$ to 30 ($s = 13$–27 for the fixed time chosen by Zlotnik *et al.* (2003) for a quantitative analysis) were simultaneously excited in the event under consideration. A necessary condition for the emergence of resolved zebra-pattern stripes is a ring-type electron distribution in transverse (relative to the magnetic field) velocities (with a zero mean velocity along the magnetic field). The periodic injection of electrons from the footpoints of the magnetic loop is the source of the energetic particles responsible for the zebra pattern, and the distribution function of the required shape is formed in the trap through the escape of electrons into the loss cone. The time delay between the onset of pulsations and the emergence of the zebra pattern is attributable to the higher threshold of instability at the double plasma resonance than that of beam instability. Therefore, the multiple injection of beams, which manifested itself in the form of radio pulsations, initially pumped a large number of fast electrons into the trap, following which instability at the double plasma resonance grew. After the injection ceased, the zebra pattern in the event under consideration decayed with a characteristic time of $\tau_{\mathrm{z}} \simeq (40$–$50)$ s.

THE EFFICIENCY OF THE ACCELERATION MECHANISM

Let us consider the balance of energetic particles in the coronal magnetic loop depicted in the figure under the following assumptions. We assume that the fast electrons with the number density $n_{\mathrm{h}}(t)$ averaged over the radio pulsation period are uniformly distributed over the trap (the coronal magnetic loop) and are accumulated in it through the action of the source I (s^{-1}) associated with the acceleration mechanism. At a certain stage, when $n_{\mathrm{h}}(t)$ exceeds the instability threshold at the double plasma resonance, a zebra pattern is generated. At the same time, the losses of energetic particles from the trap arise from their precipitation into the loss cone due to the quasi-linear diffusion of the energetic particle distribution function through the interaction with plasma waves. A comparison of the dynamic spectrum for the zebra pattern with the magnetic field of the loop restored from optical data shows that the instability at the double plasma resonance arises not in the entire trap, but only in its northeastern (NE) part and in a limited range of heights, from approximately 70 000 km (the top of the trap) to 40 000 km above the photosphere. Let us denote the magnetic field at a height of 40 000 km, i.e., at the lower instability boundary, by B_*. We assume that quasi-linear effects near the instability boundaries give rise to a quasi-isotropic distribution function of fast particles. This situation is typical of moderate and strong pitch—angle diffusion (Bespalov *et al.* 1991), and we will show that these regimes are realized in our case. An isotropic distribution function allows (using the results by Bespalov *et al.* 1991) the formula for the precipitation rate of the energetic particles from the trap to be written as

$$\dot{N}_{\mathrm{loss}} \approx -\frac{n_{\mathrm{h}} v}{2} \left[S_* \left(1 - \sqrt{1 - \sigma_*^{-1}}\right) + S_{\mathrm{top}} \left(1 - \sqrt{1 - \sigma_1^{-1}}\right) \right], \qquad (1)$$

where $\sigma_* = B_2/B_*, \sigma_1 = B_1/B_{\mathrm{top}}$, S_* and S_{top} are the cross-sectional areas of the coronal magnetic loop at the high-frequency and low-frequency (at the top of the loop) instability boundaries, respectively. Since the mirror ratios σ_* and σ_1 satisfy the conditions

$$\sigma_* \gg 1, \quad \sigma_1 \gg 1, \qquad (2)$$

and since the magnetic flux through the cross section of the tube is conserved, i.e., $S_* = \sigma_* S_2$ and $S_{\mathrm{top}} = \sigma_1 S_1$, we derive a simple expression for the precipitation rate from (1):

$$\dot{N}_{\rm loss} \approx -\frac{1}{4} n_{\rm h} v (S_1 + S_2)\ {\rm s}^{-1}. \tag{3}$$

The volume of the trap can be estimated by approximating it by a straight trap of length L with cross sections S_1 and S_2 at its ends and with a parabolic coordinate dependence of the cross section. As a result, we obtain the number of fast particles in the trap:

$$N_{\rm h} \approx n_{\rm h} \int\limits_0^L S(l)dl \approx \frac{2}{3} n_{\rm h} S_1 \sigma_1 L. \tag{4}$$

Using (3) and (4), we can easily derive the following equation for the balance of fast particles in the coronal magnetic trap:

$$\frac{dn_{\rm h}}{dt} = -\frac{n_{\rm h}}{\tau} + \frac{3I}{2S_1\sigma_1 L}, \tag{5}$$

where

$$\tau = \frac{8}{3}\frac{\sigma_1 L}{v}\frac{S_1}{S_1 + S_2} \tag{6}$$

is the characteristic precipitation time of the energetic particles from the trap, and I is the number of hot electrons supplied into the trap per unit time. Assuming the trap length to be $L \simeq \pi H \approx 2.35 \times 10^{10}$ cm and substituting the parameters from the previous section into (6), we obtain an estimate of the precipitation time, $\tau \approx 40$–50 s, which is close to the characteristic decay time of the zebra pattern. Equation (5) allows an increase in the number density of energetic electrons in the trap with time for the acting source I:

$$n_{\rm h}(t) = \frac{4I}{v(S_1 + S_2)}\left(1 - e^{-t/\tau}\right). \tag{7}$$

Since the total duration of the pulsations (the acceleration phase) $\tau_{\rm p}$ is several times longer than τ, the number density reaches its steady-state value

$$\bar{n_{\rm h}} \approx \frac{4I}{v(S_1 + S_2)}. \tag{8}$$

After the acceleration mechanism is turned off, the number density of fast particles in the trap decreases exponentially:

$$n_{\rm h}(t) = \frac{4I}{v(S_1 + S_2)} e^{-t/\tau}. \tag{9}$$

Thus, the time τ determines the duration of the zebra pattern after the source is turned off.

The intensity of the acceleration source I can be estimated from the radio brightness temperature of the zebra pattern, since the brightness temperature depends on the plasma wave energy density in the source, and the wave energy density, in turn, is determined by the intensity of the acceleration source. The brightness temperature $T_{\rm b}$ of the radio emission that emerges during the induced scattering of plasma waves with a quasi-isotropic spectrum by thermal coronal plasma ions is defined by (Zaitsev and Stepanov 1983)

$$k_{\rm B} T_{\rm b} \approx \frac{\pi}{36}\frac{\omega_{\rm p}}{\nu_{\rm ei}} m_{\rm e} v^2 \frac{W_{\rm L}}{n k_{\rm B} T}, \tag{10}$$

where $\nu_{\rm ei}$ is the effective electron–ion collision frequency, $m_{\rm e}$ is the electron mass, n and T are the density and temperature of the main plasma, $k_{\rm B}$ is the Boltzmann constant, and $W_{\rm L}$ is the plasma wave energy density. The plasma wave energy density in the steady-state regime of loss-cone instability, when the losses of particles through their diffusion into the loss cone are compensated for by the source, was calculated by Shaposhnikov (1988):

$$W_{\rm L} = \frac{j m_{\rm e} v^2}{4\nu_{\rm ei}} \ln \bar{\sigma}, \tag{11}$$

where j is the source function of the fast particles, i.e., the number of particles supplied by the source per unit trap volume per unit time. In our case,

$$j = \frac{3I}{2S_1\sigma_1 L}\ {\rm cm}^{-3}\ {\rm s}^{-1}. \tag{12}$$

Substituting (11) and (12) into (10) yields the intensity of the source expressed in terms of the observed brightness temperature of the zebra pattern, the velocity of the fast electrons, the geometric parameters of the trap, and the parameters of the coronal plasma:

$$I \approx 30 S_1 \sigma_1 L \frac{k_{\rm B} T_{\rm b}}{m_{\rm e} v^2}\frac{v_{T{\rm e}}^2}{v^2}\frac{\nu_{\rm ei}}{\omega_{\rm p}}\frac{n\nu_{\rm ei}}{\ln\bar{\sigma}}\ {\rm s}^{-1}, \tag{13}$$

where $v_{T_{\rm e}}$ is the thermal electron velocity.

The observed brightness temperature of the zebra-pattern stripes in the October 25, 1994 event was $T_{\rm b} \approx 1.4 \times 10^{10}$ K. Assuming that the coronal plasma temperature is $T = 2 \times 10^6$ K, the number density is $n = 6.8 \times 10^8$ cm^{-3} (which corresponds to the maximum frequency of the observed zebra pattern $\omega_{\rm p} = 2\pi \times 234$ MHz), and $\ln\bar{\sigma} \approx 3$ (the lower instability boundary where the degree of transverse anisotropy in the fast-particle distribution function is at a maximum), we obtain an estimate of the intensity of the acceleration source in the October 25, 1994 event from Eq. (13), $I \approx 2.6 \times 10^{32}$ s^{-1}. Thus, the derived acceleration efficiency is three or four orders of magnitude lower than the electron acceleration efficiency during solar flares. The estimated I may be assumed to be typical of intense type-IV radio bursts with a zebra pattern. The estimated I may also be assumed to characterize the efficiency of the residual post-flare electron acceleration in the active region.

Let us compare the number density of fast electrons in the trap with the threshold value required for the growth of instability at the double plasma resonance. Equation (8) yields $n_\mathrm{h} \approx 4 \times 10^3$ cm^{-3} or $n_\mathrm{h}/n \simeq 6 \times 10^{-6}$. On the other hand, the threshold for the growth of instability at the double plasma resonance is determined by the condition (Zlotnik *et al.* 2003)

$$n_\mathrm{h}^\mathrm{min}/n = s\nu_\mathrm{ei}/\omega_\mathrm{p}, \tag{14}$$

which yields $n_\mathrm{h}^\mathrm{min}/n \approx 1.4 \times 10^{-7}$ for $s = 13$; i.e., the number density of fast particles in the source is approximately a factor of 40 higher than the threshold value required for the growth of instability.

DISCUSSION

In this paper, we used the results of a comprehensive analysis of the October 25, 1994 event that included the fine structure of type-IV bursts in the form of broad-band quasi-periodic pulsations and the succeeding zebra pattern. Invoking spectral and heliographic data as well as soft X-ray and optical observations allowed us to ascertain the magnetic structure of the sources, their sizes and relative positions, to determine the velocity of the electrons injected into the magnetic trap, and to localize the site of initial acceleration. Restoring the magnetic field from photospheric optical data made it possible to determine the sizes of the trap, the degree of its asymmetry, and the mirror ratios of both footpoints.

The periodic injection of fast electrons into the trap leads to the accumulation of particles and to the growth of loss-cone instability near the upper hybrid frequency. If the double plasma resonance condition is satisfied, this instability shows up in the dynamic spectrum as a zebra pattern. Since the observed radio brightness temperature in the event under consideration is high ($T_\mathrm{b} \simeq 1.4 \times 10^{10}$ K), we assumed that the level of plasma waves provided moderate or strong pitch–angle diffusion of fast electrons; as a result, the fast particle velocity distribution function is nearly isotropic. This assumption allowed us to determine the characteristic lifetime of the zebra pattern, which depends on the geometry of the trap, the mirror ratio, and the particle velocity. All of these parameters known from experiments yielded an estimate of the characteristic trap depletion time after the completion of the acceleration phase that closely agrees with observations. Knowing the radio brightness temperature of the zebra pattern, we were able to estimate the energy density of the plasma waves excited at the double plasma resonance and the intensity of the acceleration source. The acceleration mechanism in the event under consideration yielded an acceleration rate of $I \simeq 2.6 \times 10^{32}$ s^{-1}, which is approximately three orders of magnitude lower than the electron acceleration rate during a moderately intense solar flare. In this case, the mean number density of fast electrons in the trap at the end of the acceleration process is approximately a factor of 40 higher than the threshold value for the growth of instability at the double plasma resonance.

Let us estimate the extent to which our assumption about the realization of strong pitch–angle diffusion is valid. According to the results by Bespalov and Trakhtenhertz (1986) and Bespalov *et al.* (1991), strong pitch–angle diffusion is realized if the particle flux at the ends of the trap exceeds a critical value,

$$J_* \simeq \frac{cB\sigma}{4\pi eL}. \tag{15}$$

Assuming that $B \simeq 2 \times 10^2$ G, $\sigma \simeq 10^2$, and $L \simeq 2 \times 10^{10}$ cm, we obtain $J_* \simeq 5 \times 10^{12}$ cm^{-2} s^{-1}. In our case, the flux $J_e = \bar{n}_\mathrm{h}v/4 \simeq 10^{13}$ cm^{-2} s^{-1} exceeds J_*; i.e., the initial assumption is justified.

In our view, the results obtained are of considerable interest for a detailed analysis of the particle acceleration mechanisms responsible for the type-IV continuum emission with a fine structure, allowing us to choose those that better meet the inferred requirements for the efficiency of the acceleration mechanism. In addition, our intensity estimates for the source of fast electrons that lead to type-IV radio pulsations may be considered as characteristics of the acceleration mechanism in an active region at the post-flare phase of its evolution.

ACKNOWLEDGMENTS

This work was supported by the Russian Foundation for Basic Research (project nos. 05-02-16252a and 04-02-16148a), the Program for Support of Leading Scientific Schools of Russia, the Comprehensive Nonstationary Processes in Astronomy program of the Presidium of the Russian Academy of Sciences, and the Solar Wind: Generation and Interaction with the Earth and other Planets program of the Department of Physical Sciences of the Russian Academy of Sciences.

REFERENCES

1. H. Aurass, K.-L. Klein, E. Ya. Zlotnik, and V. V. Zaĭtsev, Astron. Astrophys. **410**, 1001 (2003).
2. P. A. Bespalov and V. Yu. Trakhtenhertz, Rev. Plasma Phys. **10**, 155 (1986).

3. P. A. Bespalov, V. V. Zaitsev, and A. V. Stepanov, Astrophys. J. **374**, 369 (1991).
4. J. A. Miller, J. P. Cargill, A. G. Emslie, *et al.*, J. Geophys. Res. **102**, 14 631 (1997).
5. V. E. Shaposhnikov, Pis'ma Astron. Zh. **14**, 644 (1988) [Sov. Astron. Lett. **14**, 275 (1988)].
6. T. Tajima, J. Sakai, H. Nakajima, *et al.*, Astrophys. J. **321**, 1031 (1987).
7. V. V. Zaitsev and A. V. Stepanov, Solar Phys. **88**, 297 (1983).
8. V. V. Zaitsev, A. V. Stepanov, S. Urpo, and S. Pohjolainen, Astron. Astrophys. **337**, 887 (1998).
9. V. V. Zheleznyakov, *Radio Emission from the Sun and Planets* (Nauka, Moscow, 1964).
10. E. Ya. Zlotnik, V. V. Zaitsev, H. Aurass, *et al.*, Astron. Astrophys. **410**, 1011 (2003).

Translated by V. Astakhov